PHASES AND CRITICAL PHENOMENA IN 3D TOPOLOGICAL SUPERCONDUCTORS AND SEMIMETALS

A Dissertation Presented to

the Faculty of the Department of Physics

University of Houston

In Partial Fulfillment

of the Requirements for the Degree

Doctor of Philosophy

By

Sayed Ali Akbar Ghorashi

May 2018

PHASES AND CRITICAL PHENOMENA IN 3D TOPOLOGICAL SUPERCONDUCTORS AND SEMIMETALS

Sayed Ali Akbar Ghorashi

APPROVED:

Professor Chin-Sen Ting, Chairman
TcSUH and Department of Physics, University of Houston

Assistant Professor Matthew S. Foster
Department of Physics and Astronomy, Rice University

Assistant Professor Pavan Hosur
TcSUH and Department of Physics, University of Houston

Professor Gemunu Gunaratne
Department of Physics, University of Houston

Professor Wei-Kan Chu
TcSUH and Department of Physics, University of Houston

Dean, College of Natural Sciences and Mathematics

Acknowledgement

This work would not have been possible without the support of several people. I would like to first thank my adviser Dr. Chin-Sen Ting for letting me work in his group while giving me freedom, support and opportunity to pursue my topics of interests. I am greatly indebted to Dr. Matthew Foster at Rice university who accepted me as part of his group as well as his supervision for most of the research done in this thesis. When I started to work with Matthew about three years ago, I knew a small fraction of what I know now, and it required great patience, kindness and wisdom on his behalf to get me here.

I am also thankful to the other members of my PhD committee, Dr. Pavan Hosur, Dr. Gemunu Gunaratne and Dr. Wei-Kan Chu. In particular, Pavan, who started to collaborate with me as soon as he joined the University of Houston on a project that constitutes the last chapter of this dissertation. I also would like to thank my other bright collaborators, Seth Davis, Bitan Roy and Yunxiang Liao. Moreover, I would like to thank all the members of groups of Dr. Ting at UH and Dr. Foster at Rice with whom I had a chance to have illuminating discussions.

Last but not least, I would like to express my deep gratitude for my parents and family. All that I have achieved I owe to the upbringing, love and support provided by my parents.

PHASES AND CRITICAL PHENOMENA IN 3D TOPOLOGICAL SUPERCONDUCTORS AND SEMIMETALS

An Abstract of a Dissertation

Presented to

the Faculty of the Department of Physics

University of Houston

In Partial Fulfillment

of the Requirements for the Degree

Doctor of Philosophy

By

Sayed Ali Akbar Ghorashi

May 2018

Abstract

In this dissertation, we have studied the effect of disorder and interaction on some classes of topological superconductors and semimetals. In the superconducting phase, we studied various phases and critical phenomena that arise by the effect of disorder on the surface states of topological superconductors with different and higher winding numbers. In particular, we investigated topological protection of topological superconductors with effective spin-3/2 systems. Moreover, we have shown that the almost all the finite-energy states at the surface of topological superconductors in the presence of disorder are also protected (delocalized) and sit at the spin quantum plateau transition point without fine tuning. Finally, through the Floquet formalism we showed that the irradiated Luttinger semimetal is a suitable platform for engineering various Weyl semimetals, from Type-I to type-II as well as single and double Weyl semimetals.

Contents

List of Figures

List of Tables

Chapter 1

Introduction

The introduction of the concept of topology in band theory is the one of the most important advances of condensed matter physics, which dominated much of the research areas over past decade. The "topological states of the matter", are states of matter in which their electronic structures are topologically nontrivial. A hallmark signature of a topologically non-trivial system is the existence of robust gapless states at an interface with the trivial vacuum, exposing the information about the bulk topological invariant to the external world. This classification includes both gapped and gapless systems. The most famous example of nontrivial topology in solid state physics is the integer quantum Hall effect (IQHE), in which protected chiral edge states give rise to a quantized transverse Hall conductivity.

In this dissertation, I focused on topological superconductors and semimetals in three dimensions. In particular, I study the phases and critical phenomena that result from the interplay of topology with disorder and interactions. The rest of the dissertation

is organized as follows: An overview of topological phases with emphasis on some prominent examples of topological superconductors and semimetals is discussed in chapter 2. In chapter 3, we discuss the effect of disorder and interaction on the surface states of doped three-dimensional Luttinger semimetal, describing a quadratic band touching bands of effective spin-3/2 carriers. In chapter 4, I study the disordered surface state of topological superconductors in class CI and report on the novel discovery of spin quantum plateau transition in the finite-energy states of these surfaces. In chapter 5, I discuss the interaction of light with a three-dimensional Luttinger semimetal using Floquet theory. We summarize this dissertation in chapter 6.

Works discussed in this thesis have been published in,

1. **Ghorashi**, Davis, Foster, PRB, **95**, 144503 (2017). (Chapter 3)

2. Roy, **Ghorashi**, Foster, Nevidomskyy, arXiv:1708.07825. (Chapter 3)

3. **Ghorashi**, Liao, Foster, arXiv:1711.03972. (Chapter 4)

4. **Ghorashi**, Hosur, Ting, arXiv:1801.04287. (Chapter 5)

Chapter 2

Topological phases

In this chapter we present a review of some important concepts that would be useful for the rest of this thesis.

2.1 Topological Superconductors in 2D

The chiral superconductor in 2D, $p_x + ip_y$, is the simplest topological system which can manifest the main properties of a topological system. Its Hamiltonian can be written as [5, 6],

$$H = \sum_k \Psi^\dagger h_k \Psi_k; \quad h_k = \frac{1}{2} \sum_k \begin{pmatrix} \epsilon(\mathbf{k}) & 2i\Delta(\sin(k_x) + i\sin(k_y)) \\ -2i\Delta^*(\sin(k_x) - i\sin(k_y)) & -\epsilon(\mathbf{k}) \end{pmatrix} \tag{2.1}$$

where $\Psi_k = (C_k, C^\dagger_{-k})^T$ and $\epsilon(\mathbf{k}) = -2t(\cos(k_x)+\cos(k_y))-(\mu-4t)$. In the continuum limit we can write the above equation in the following form,

$$h_k = \frac{1}{2}\sum_k \begin{pmatrix} \frac{\mathbf{k}^2}{2m} - \mu & 2i\Delta(k_x + ik_y) \\ -2i\Delta^*(k_x - ik_y) & -\frac{\mathbf{k}^2}{2m} + \mu \end{pmatrix} \tag{2.2}$$

with $\mathbf{k}^2 = k_x^2 + k_y^2$. The spectrum of continuum model is given as $\mathcal{E}(\mathbf{k}) = \pm\sqrt{(\frac{\mathbf{k}^2}{2m} - \mu)^2 + 4|\Delta|^2\mathbf{k}^2}$ and is gapped as long as $\mu \neq 0$. In fact, at $\mu = 0$ the 2.2 undergoes a phase transition between topologically trivial ($\mu < 0$) and nontrivial ($\mu > 0$) cases. Therefore, we can study a domain wall geometry between these two phases by taking $\mu = \mu(x)$, such that $\mu = -\mu_0$ for $x < 0$ and $\mu = \mu_0$ for $x > 0$ for a positive constant μ_0. By keeping the translational invariance in y direction, k_y is still can be considered as good quantum number. Therefore, solving for the quasi-1D Hamiltonian (up to first order of $\mathbf{k}$) with,

$$h_k = \begin{pmatrix} -\mu(x) & 2i|\Delta|(-i\partial_x + ik_y) \\ -2i|\Delta|(-i\partial_x - ik_y) & \mu(x) \end{pmatrix}, \tag{2.3}$$

one can find a bound states at the interface of two topologically distinct phases with $\mu(x) < 0$ and $\mu(x) > 0$, respectively. It can be obtained as,

$$\psi_{k_y}(x, y) = e^{ik_y y}\left(-\frac{1}{2|\Delta|}\int_0^x \mu(x')dx'\right)|\phi_0\rangle \tag{2.4}$$

where $|\phi_0\rangle$ is a constant normalized spinor. This set of bound states parameterized by k_y as $E(k_y) = -2|\Delta|k_y$ is gapless and the group velocity of the quasiparticle dispersion is always negative and never changes sign (chiral). Next, we compute the

bulk topological winding number (Chern number). To do so, we rewrite 2.2 as,

$$h_k = \sum_a d_a(\mathbf{k}).\hat{\tau}^a;$$
$$d_a(\mathbf{k}) = \left(-2|\Delta|k_y, -2|\Delta|k_x, \frac{\mathbf{k}^2}{2m} - \mu\right) \tag{2.5}$$

where $\hat{\tau}^a$ are Pauli matrices. Now by using unit vector $\hat{d}_a = d_a/|\mathbf{d}|$ and employing following formula,

$$\hat{N}_w = \frac{1}{8\pi}\int d^2\mathbf{p}\epsilon^{ij}\hat{d}.\left(\partial_{k_i}\hat{d} \times \partial_{k_j}\hat{d}\right) \tag{2.6}$$

one can by computing above integral numerically easily find $\hat{N}_w = 0$ and $\hat{N}_w = 1$ for $\mu < 0$ and $\mu > 0$ respectively.

2.2 Topological superconductivity in 3D: The case of ^{3}He-B

Now lets turn to an example of topological superconductivity (superfluidity) in three dimensions. The prototypical example of such a system that is confirmed to be topological is phase B of ^{3}He, which possess an isotropic p-wave fully gapped pairing [6, 7]. Moreover, reviewing of the later, it is particularly of interest of this dissertation because we will going to study the spin-3/2 generalization of ^{3}He-B. The topological superfluidity of ^{3}He-B is protected by the time-reversal symmetry as well as the particle-hole symmetry. It can be described by the following Hamiltonian,

$$h_k = \begin{pmatrix} \frac{\mathbf{k}^2}{2m} - \mu & \Delta(\mathbf{k}) \\ \Delta^\dagger(\mathbf{k}) & -\frac{\mathbf{k}^2}{2m} + \mu \end{pmatrix}, \tag{2.7}$$

where $\Delta(k) = \Delta_p i\sigma^2 \boldsymbol{\sigma}.\mathbf{k}$ and satisfied particle-hole $\tau^1 h_k(-\mathbf{k})^T \tau^1 = -h_k(\mathbf{k})$ and time-reversal symmetry of $\sigma^2 h_k^*(\mathbf{k})\sigma^2 = h_k(\mathbf{k})$ so it belongs to class DIII ($(\tau^1)^2 = 1$ and $(\sigma^2)^2 = -1$)[9]. τ and σ denotes Nambu and spin spaces, respectively.

Topological invariant for three-dimensional superconductors with chiral symmetry [9] can be obtained by following steps:

- Diagonalize the Hamiltonian to get U_h eigenvector matrices.
- Build a flat Hamiltonian of $Q = U_h^{-1} \Lambda U_h$ where Λ is the flattened matrix of eigenvalues.
- Off-diagonalize Q to get,

$$\begin{pmatrix} 0 & q(\mathbf{k}) \\ q^\dagger(\mathbf{k}) & 0 \end{pmatrix}; \quad q^\dagger(\mathbf{k}) q(\mathbf{k}) = 1 \tag{2.8}$$

- Use following equation to calculate the winding number,

$$W = \frac{1}{24\pi^2} \int d^3\mathbf{k} \epsilon^{ijk} \operatorname{Tr}\left[(q^{-1}\partial_i q)(q^{-1}\partial_j q)(q^{-1}\partial_k q)\right]; \quad \partial_i \equiv \partial_{k_i}. \tag{2.9}$$

It can be applied to (2.7) and one can see that for $\mu < 0$ and $\mu > 0$ give $W = 0$ and $W = 1$, respectively.

The 2D surface states of (2.7) possess the neutral helical Majorana quasiparticles with the effective Hamiltonian,

$$\hat{h}_{\mathrm{s}} = \sum_k \xi^\dagger (k_x \sigma^1 + k_y \sigma^2) \xi, \tag{2.10}$$

where $\xi = (\gamma_{k,\uparrow}, \gamma_{k,\downarrow})^T$ and $\gamma_{k\sigma}$ satisfies $\gamma_{k\sigma}^\dagger = \gamma_{-k\sigma}$. The surface states are thus propagating (nonchiral) Majorana fermions. The surface Hamiltonian must possess

the same symmetries of the bulk, i.e., particle-hole and time-reversal symmetries (and their combination: chiral symmetry) so belong to the same symmetry class of DIII.

2.3 Effect of disorder

In this section we review some of the essential concepts and methods that are used in the rest of this thesis for treating the effect of disorder on the surface states of topological superconductors. Anderson theory of localization has been the corner stone of the disordered physics since 1958 [28].

In three dimensions, it is shown [28] that in the presence of random disorder wavefunctions show two different behaviors, extended and localized, unlike the one and two dimensional cases where eigenstates are always localized. However, at the transition point, wavefunctions are critically delocalized. The probability distribution in this phase shows "multifractal" statistics, i.e it contains random peaks while most of places is zero. However, the hallmark of theses states is the universal properties in their wavefunction statistical properties. Fig. 2.1, shows an example of a multifractal state.

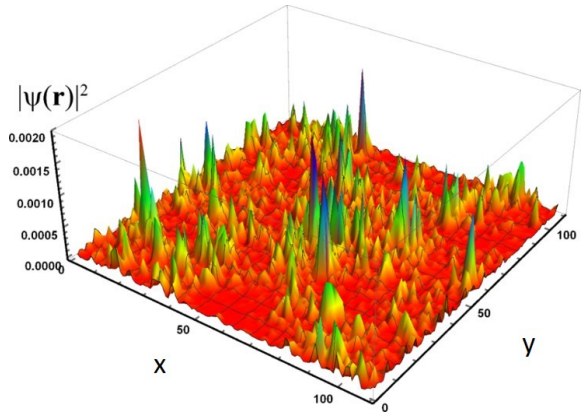

Figure 2.1: Shows probability distribution (no unit) for a sample multifractal wavefunction.

For most of this dissertation we use multifractality as measure of criticality on the surface state of different topological superconductors. The multifractal spectrum measures the statistics of the local DoS, which can be measured experimentally by scanning tunneling microscopy [1].

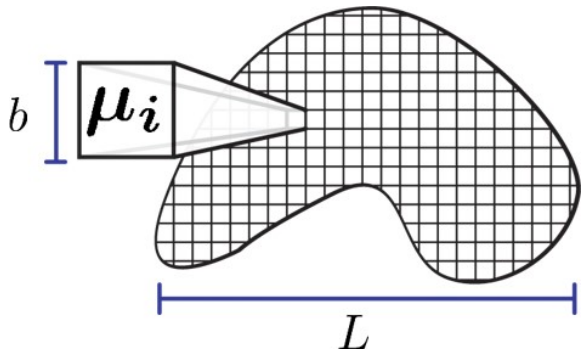

Figure 2.2: Schematic picture of discretizing space to box sizes of b and system size of L.

Here we mention main steps to compute multifractal spectrum numerically. First, we discretize the space to small boxes of size $b << L$ where L (Fig. 2.2) is the system size and get box probability as,

$$\mu_i = \int_{box\ i} d^2\mathbf{r}|\psi(\mathbf{r})|^2. \tag{2.11}$$

Then, one can get the Inverse participation ration (IPR),

$$P_q = \sum_i \mu_i^q \sim \left(\frac{b}{L}\right)^{\tau(q)}. \tag{2.12}$$

$\tau(q)$ is the multifractal exponent associated with the qth IPR. We get $\tau(q)$ by computing the logarithm of the ratio of two P_q with different box sizes of b. $\tau(q)$ is a self-averaging quantity [2] that satisfies the conditions $\tau(1) = 0$ due to the normalization and $\tau(0) = -d$, where d is system dimension. For simple plane wave $\tau(q) = d(q-1)$ because the probability of finding a particle is uniform. For the critical states it is shown to be [10, 11],

$$\tau(q) = (q-1)(2-\theta q), \ \ |q| \leq q_c = \sqrt{2/\theta}, \tag{2.13}$$

where θ can be viewed as the degree of multifractality.

q_c denotes the termination threshold which after that $\tau(q)$ shows a linear behavior with respect to q.

2.4 Gapless topological phases: The case of topological semimetals

In this section, we review some of the most important properties of gapless topological phases. In particular, we focus on Weyl semimetals. Weyl semimetals can be seen as three-dimensional analogs of graphene. The low-energy theory around a Weyl point can be described by 2×2 Hamiltonian of $\mathcal{H}_w = \sigma.\mathbf{k} = \sigma^1 k_x + \sigma^2 k_y + \sigma^3 k_z$. In the presence of time-reversal and inversion symmetries Weyl points are doubly degenerate, as guaranteed by Kramers theorem. Therefore, to make Weyl semimetal we need to break either of time reversal or inversion symmetries.

Without loss of generality we can start from two-band lattice model with breaking time-reversal symmetry [3],

$$\mathcal{H}(k) = [2t(\cos(k_z) - \cos(k_0)) + m(2 - \cos(k_y) - \cos(k_x)]\,\sigma^3 + 2t\sin(k_y)\sigma^2 + 2t\sin(k_x)\sigma^1, \tag{2.14}$$

where by setting $t = 1$ and $m = -2$, it has two nodes at $(0, 0, \pm k_0)$. Each node has *chirality* denoted by $\pm$ in the later. A Weyl point can thus be destroyed only by annihilating it with another Weyl point of opposite chirality. To characterize the topological nature of these points we use the Chern number associated to each node. To get the Chern number (monopole charge) we write the effective low-energy Hamiltonian as $\mathcal{H} \propto \mathbf{n}(k).\boldsymbol{\sigma}$ and use,

$$W_n = \frac{1}{8\pi}\int_s d^2\mathbf{k}\epsilon^{ijk}\mathbf{n}.(\partial_j\mathbf{n} \times \partial_k\mathbf{n}), \tag{2.15}$$

where integration is performed over surface S surrounding the node and $\mathbf{n}$ is a unit

vector. W_n is an integer value which can be positive or negative depending on the chirality of the specific node. So, it is clear that the total Chern number over whole Brillouin zone is zero. As result of nontrivial topology, the projection of two nodes with different chirality on the surface, leads to the zero-energy fermi arcs which are the hallmark of Weyl semimetals. The properties of these fermi arcs are extensively studied over past couple of years [3].

Chapter 3

Topological superconductivity in Spin-3/2 systems

In this Chapter, the topological superconductivity in Luttinger semimetals with effective spin-3/2 is investigated. To proceed we divided this topic to two parts. First, we have considered the case were both bands bending in same direction that is relevant to hole-doped semiconductors. Then, as the second part, the case where bands bending oppositely is studied.

This chapter is mainly adapted from the following published papers: S.A.A. Ghorashi, S. Davis, M.S. Foster, Phys.Rev. B, 95, 144503 (2017) and B. Roy, S.A.A. Ghorashi, M.S. Foster, A.H. Nevidomskeyy, arXiv:1708.07825.

3.1 Introduction

In the past decade there has been an explosion of interest in new forms of topological matter, driven by the discoveries of topological insulators and gapless topological phases [4, 5, 6, 7]. Despite this progress, a three-dimensional analog of the IQHE that ties a robust surface transport signature directly to a bulk winding number remains lacking. One potentially promising route is to look for a generalization of Helium 3B (^{3}He-B), the only known bulk topological superfluid predicted to host a gapless surface fluid of unpaired Majorana fermions [8, 9].

Previous theoretical work [9, 10, 11, 12, 13] has shown that the Majorana surface fluid of a model spin-1/2 bulk topological superconductor (TSC) can be robust to both disorder and interaction effects, and should exhibit a universal surface thermal conductivity proportional to the bulk winding number [13]. In all of these works, the form of the 2D surface theory was always assumed to be relativistic, with $|\nu|$ "colors" of linearly-dispersing Majorana fermions coupled via interactions and/or quenched disorder; ν denotes the winding number. A key unanswered question is whether the physics (e.g., universal thermal conductivity) is tied to this simplifying assumption, or instead represents a robust aspect of generic bulk TSCs.

Recent theoretical work has turned to higher-spin TSCs, with potential applications to alkaline and alkaline-earth ultracold atoms [14] or doped semimetals with spin-orbit coupling [15, 16, 17]. In the first part of this chapter, we consider the surface states of a spin-3/2 generalization of ^{3}He-B with isotropic p-wave pairing [14]. A novel feature is that the surface Majorana fluid exhibits coexisting linear and cubic

bands. Cubic surface bands were also predicted in a closely related model [15] that may be relevant for superconducting half-Heusler alloys, discussed in the second half of this chapter. Due to the van Hove singularity, one might expect that any residual interactions between surface Majorana particles would produce a strong instability. Surprisingly, we show that interactions are only *marginally relevant*: only attractive interactions induce spontaneous time-reversal symmetry breaking and lead to a surface thermal quantum Hall effect (TQHE) [9, 10]. This weak instability is tied to the strong constraints imparted by Pauli exclusion to a Majorana gas, despite the density of states divergence. Repulsive interactions are marginally irrelevant; their main effect would be to generate a finite longitudinal surface thermal conductivity κ_{xx} at temperature $T > 0$ due to inelastic scattering. In the absence of impurity scattering the ratio κ_{xx}/T would diverge as $T \to 0$.

By contrast, nonmagnetic quenched disorder proves to be a strong perturbation. Using exact diagonalization to study the noninteracting dirty surface, we show that disorder induces scaling consistent with a critical, exactly solvable conformal field theory (CFT) $\mathrm{SO}(n)_4$ [11]. (Here $n \to 0$ denotes the number of replicas.) The CFT governs the divergence of the global density of states and the statistics of the single-particle wave functions. The level of the current algebra (=4) is also the modulus of the bulk winding number $|\nu|$ for our p-wave model. This is the same result that obtains for spin-1/2 models of TSC surface states studied previously [11, 13]. In the spin-1/2 case with winding number ν, the clean surface fluid is a free fermion (level one) CFT due to the relativistic dispersion. The emergence of another CFT with level $|\nu|$ in the presence of disorder follows from certain rules in these theories

(conformal embeddings [11, 13]).

Here the situation is very different. The clean Majorana fluid of the spin-3/2 model is not a CFT, as evidenced by the cubic dispersion. Moreover, a standard derivation of the effective surface theory with disorder would incorrectly predict a thermal metal with weak antilocalization [24, 11]. Properties of this metal would depend on the bare disorder strength and would vary slowly with system size. Our numerics instead show universal scaling that is independent of the disorder strength. In conjunction with the conformal embedding argument for the spin-1/2 case, the results obtained here empirically suggest a deep relation between the topology of the bulk and the CFT describing the *disordered surface* of a TSC, despite the fact that the clean surface theories can fundamentally differ. Technically, it means that the topology precisely tunes the surface field theory to the conformal fixed point made possible by a Wess-Zumino-Novikov-Witten term [11]. Without this fine-tuning, this fixed point is *unstable* to the thermal metal phase (despite the WZNW term) [13].

The $\mathrm{SO}(n)_4$ CFT that describes the disordered Majorana surface fluid is known to be protected against weak interaction effects [11]. We conclude that disorder *stabilizes* the surface Majorana fluid for this spin-3/2 model, and this implies that higher-spin TSCs could be robustly protected. The thermal Hall conductivity κ_{xy} divided by temperature T of the surface TQHE is quantized and universal [18, 19, 20, 21, 22, 23]: $\kappa_{xy} = W\,\kappa_\circ$, where $W \in \mathbb{Z}$ is the *surface winding number* and,

$$\kappa_\circ/T = \pi^2 k_B^2/6h. \tag{3.1}$$

What is more important here is that [9, 13]

$$\lim_{T\to 0} \frac{\kappa_{xx}}{T} = \frac{|\nu|}{\pi} \frac{\kappa_\circ}{T}, \quad \kappa_{xy} = 0, \tag{3.2}$$

for the disorder-induced surface CFT (which preserves time-reversal symmetry). Here the winding number $\nu = 4$. Eq. (3.2) implies that the low-temperature thermal conductivity is quantized by the bulk winding number, independent of both disorder and interactions. Since disorder stabilizes the surface and induces a quantized thermal conductivity, bulk TSCs appear to be closely analogous to the integer quantum Hall effect in two dimensions. Our results are summarized by the phase diagram in Fig. 3.1.

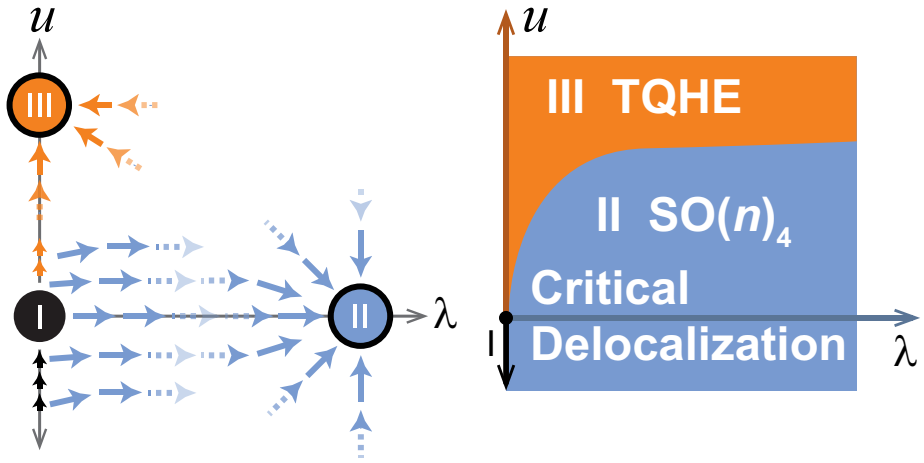

Figure 3.1: Schematic renormalization group (RG, left) and parameter (right) phase diagram: 2D Majorana fermion surface fluid of a bulk spin-3/2 topological superconductor with p-wave pairing and winding number $\nu = 4$. The axes denote surface perturbations: the interaction strength u and quenched disorder strength λ. In the absence of disorder ($\lambda = 0$), the clean surface ("I") is marginally unstable to spontaneous time-reversal symmetry breaking [thermal quantum Hall effect (TQHE) order, ("III")] for $u > 0$. Disorder $\lambda > 0$ is a strong perturbation that drives the surface into a critically delocalized, time-reversal symmetric state [SO$(n)_4$ CFT, "II"]. The latter is stable against weak interaction effects [11]. Disorder is formally irrelevant to III because it can be viewed as a gapped, paired Majorana BCS condensate. RG results near I and II are obtained by analytical and numerical calculations, while III is confirmed by mean-field theory. The boundary between II and III on the right likely indicates a first order transition, but neither its nature nor its precise shape in the λ-u plane is determined here. The surface thermal conductivity is precisely quantized in *both* phases II and III: $\{\kappa_{xx}, \kappa_{xy}\} = \{4/\pi, 0\}\,\kappa_\circ$ in II [9, 13] and $\{\kappa_{xx}, \kappa_{xy}\} = \{0, \pm 2\}\,\kappa_\circ$ in III [18, 19, 20, 21, 22, 23]. Here $\kappa_\circ \equiv \pi^2 k_B^2 T/6h$.

This chapter is organized as follows. In Sec. 3.2, we define the bulk model and describe the form of the surface states. We then summarize our results regarding the marginal instability of the clean surface, and the universal quantum criticality of the disordered one. The rest of the paper explains key technical details. Sec. 3.3 shows the derivation of the surface state Hamiltonian and the calculation of the surface winding number in the presence of explicit time-reversal symmetry breaking. The effects of interactions on the clean surface are treated using one-loop renormalization and mean field theory. Sec. 3.4 describes the incorporation of disorder, and provides details of the numerical diagonalization scheme. In Sec. 3.5, a similar analysis is made for surface states of the doped Luttinger semimetal, where bands bend oppositely. This model may be relevant to superconductivity in half-Heusler alloys.

3.2 Model and results

3.2.1 Bulk and surface models

We consider a system of spin-3/2 fermions. In the absence of pairing, we assume a bulk Hamiltonian of the form

$$H_0 = \int \frac{d^3\mathbf{k}}{(2\pi)^3}\, c^\dagger(\mathbf{k})\, \left[k^2 - \gamma\, (\mathbf{S}\cdot\mathbf{k})^2\right]\, c(\mathbf{k}), \tag{3.3}$$

where $\mathbf{k} = \{k_{x,y,z}\}$. The 4-component fermion field $c(\mathbf{k}) \to c_{m_s}(\mathbf{k})$ has $\hat{S}^z$-label $m_s \in \{\frac{3}{2}, \frac{1}{2}, -\frac{1}{2}, -\frac{3}{2}\}$; $\mathbf{S} = \{\hat{S}^{x,y,z}\}$ are spin-3/2 operators. Eq. (3.3) is an isotropic version of the Luttinger Hamiltonian [25] used to model heavy and light hole bands in zinc-blende semiconductors; the parameter γ measures the strength of effective

spin-orbit coupling (SOC) amongst the states of the 3/2 multiplet. Here we have set $2m = 1$ in the first term (m is the band mass in the absence of SOC). We assume that $\gamma < 4/9$, so that both bands "bend up." The situation where bands bend oppositely is relevant for half-Heusler alloys; in that case similar Majorana surface states can arise with bulk p-wave pairing [15], but the winding numbers differ [26] (see Sec. 3.5).

We assume isotropic p-wave pairing of spin-3/2 fermions [14]:

$$H = \frac{1}{2} \int \frac{d^3\mathbf{k}}{(2\pi)^3} \, \chi^\dagger(\mathbf{k}) \, \hat{h}(\mathbf{k}) \, \chi(\mathbf{k}), \tag{3.4}$$

where the 8×8 Bogoliubov-de Gennes Hamiltonian is

$$\hat{h}(\mathbf{k}) = \left[k^2 - \mu - \gamma \, (\mathbf{S} \cdot \mathbf{k})^2 \right] \hat{\sigma}^3 + \Delta_p \, (\mathbf{S} \cdot \mathbf{k}) \, \hat{\sigma}^2. \tag{3.5}$$

Here μ is the chemical potential and Δ_p the BCS gap parameter. The 8-component field in Eq. (3.4) has the particle-hole space decomposition

$$\chi(\mathbf{k}) \equiv \begin{bmatrix} c(\mathbf{k}) \\ (-i\hat{R}) \, \left[c^\dagger(-\mathbf{k}) \right]^{\mathsf{T}} \end{bmatrix}, \tag{3.6}$$

where T denotes the transpose in spin-3/2 space. The Pauli matrices $\hat{\sigma}^{1,2,3}$ in Eq. (3.5) act on particle-hole space. In Eq. (3.6), $\hat{R}$ is an antisymmetric 4×4 matrix satisfying

$$\hat{R} \, (\mathbf{S})^{\mathsf{T}} \, \hat{R}^{-1} = -\mathbf{S}, \quad \hat{R}^2 = -\hat{1}. \tag{3.7}$$

The field χ satisfies the "Majorana" condition $\chi^\dagger(\mathbf{k}) = i \, \chi^{\mathsf{T}}(-\mathbf{k}) \, \hat{M}_{\mathsf{P}}$, where $\hat{M}_{\mathsf{P}} = -i\hat{\sigma}^2 \, \hat{R} = \hat{M}_{\mathsf{P}}^{\mathsf{T}}$. This implies the *automatic* particle-hole symmetry $-\hat{M}_{\mathsf{P}}^{-1} \, \hat{h}^{\mathsf{T}}(-\mathbf{k}) \, \hat{M}_{\mathsf{P}} = \hat{h}(\mathbf{k})$. Time-reversal invariance is encoded as $\hat{M}_{\mathsf{T}}^{-1} \, \hat{h}^{\mathsf{T}}(-\mathbf{k}) \, \hat{M}_{\mathsf{T}} = \hat{h}(\mathbf{k})$, where $\hat{M}_{\mathsf{T}} =$

$-\hat{M}_{\mathsf{T}}^{\mathsf{T}} = \hat{\sigma}^3 \hat{R}$. Combining particle-hole and time-reversal [14, 9] gives the effective chiral condition $-\hat{\sigma}^1 \hat{h}(\mathbf{k}) \hat{\sigma}^1 = \hat{h}(\mathbf{k})$. With all of these symmetries the model belongs to class DIII [9]. The bulk winding number is $\nu = 4$ [14] so long as $\mu > 0$ and $\gamma < 4/9$.

The effective surface Hamiltonian obtains by terminating the system in the z-direction and diagonalizing $\hat{h}(k_x, k_y, -i\partial_z)$. The momentum $\mathbf{k} = \{k_{x,y}\}$ labels propagation parallel to the surface. For $\mathbf{k} = 0$ and hard wall boundary conditions, there are four zero energy bound states $\{|\psi_{0,m_s}\rangle\}$. The most important feature is that the particle-hole "spin" locks to the physical spin at the surface:

$$|\psi_{0,m_s}\rangle = |\sigma^1 = \mathrm{sgn}(m_s)\rangle \otimes |m_s\rangle \otimes |f_{m_s}\rangle. \tag{3.8}$$

The particle-hole spin points along the $+\sigma^1$ ($-\sigma^1$) direction for positive (negative) m_s. In Eq. (3.63), $\langle z|f_{m_s}\rangle = f_{m_s}(z)$ denotes the bound state envelope function.

Since time-reversal gives the effective chiral condition $-\hat{\sigma}^1 \hat{h}(\mathbf{k}) \hat{\sigma}^1 = \hat{h}(\mathbf{k})$ in the bulk, the locking condition implies that the effective surface Hamiltonian $\hat{h}_{\mathsf{s}}$ satisfies

$$-\hat{\tau}^3 \hat{h}_{\mathsf{s}}(\mathbf{k}) \hat{\tau}^3 = \hat{h}_{\mathsf{s}}(\mathbf{k}), \tag{3.9}$$

where $\hat{\tau}^3 = +1$ (-1) for $m_s > 0$ ($m_s < 0$). We introduce two mutually commuting species of Pauli matrices: $\{\hat{\tau}^{1,2}\}$ anticommute with $\hat{\tau}^3$ and act on the $\mathrm{sgn}(m_s)$ space, while $\{\hat{\kappa}^{1,2,3}\}$ mix the 3/2 and 1/2 states with the same sign. E.g., $\hat{\tau}^3 = \mathrm{diag}(1, 1, -1, -1)$, $\hat{\kappa}^3 = \mathrm{diag}(1, -1, 1, -1)$. The matrix $\hat{R} = i\hat{\tau}^1\hat{\kappa}^2$. Then the locking condition implies the *automatic* surface particle-hole symmetry

$$-\hat{M}_{\mathsf{P}}^{(\mathsf{S})} \hat{h}_{\mathsf{s}}^{\mathsf{T}}(-\mathbf{k}) \hat{M}_{\mathsf{P}}^{(\mathsf{S})} = \hat{h}_{\mathsf{s}}(\mathbf{k}), \quad \hat{M}_{\mathsf{P}}^{(\mathsf{S})} = \hat{\tau}^2\hat{\kappa}^2. \tag{3.10}$$

The form of $\hat{h}_{\mathsf{s}}(\mathbf{k})$ is constrained by Eqs. (3.9) and (3.10), as well as rotational invariance in the plane. An explicit k·p calculation gives the low-energy form [14]

$$\begin{aligned}\hat{h}_{\mathsf{s}}(\mathbf{k}) = &\quad \tfrac{i}{4}\left(\hat{\tau}^{+}\hat{\kappa}^{-}\,\mathsf{k} - \hat{\tau}^{-}\hat{\kappa}^{+}\,\bar{\mathsf{k}}\right) + \tfrac{c}{2}\left(\hat{\tau}^{+}\,\mathsf{k}^2 + \hat{\tau}^{-}\bar{\mathsf{k}}^2\right) \\ = &\quad \begin{bmatrix} 0 & 0 & c\,\mathsf{k}^2 & 0 \\ 0 & 0 & i\,\mathsf{k} & c\,\mathsf{k}^2 \\ c\,\bar{\mathsf{k}}^2 & -i\,\bar{\mathsf{k}} & 0 & 0 \\ 0 & c\,\bar{\mathsf{k}}^2 & 0 & 0 \end{bmatrix}. \end{aligned} \tag{3.11}$$

Here, $\{\mathsf{k}, \bar{\mathsf{k}}\} = k_x \mp i k_y$, $\hat{\tau}^{\pm} = \hat{\tau}^1 \pm i\hat{\tau}^2$, $\hat{\kappa}^{\pm} = \hat{\kappa}^1 \pm i\hat{\kappa}^2$, the coefficient for the linear dispersion is normalized to one, and c is a real constant with units of length. For weak SOC ($0 < \gamma \ll 1$), it is easy to see that $c \propto \gamma/\Delta_p$. Without SOC, second-order k·p theory gives $c = 0$ so that the $m_s = \pm 3/2$ bands remain flat. Nonzero c is symmetry-allowed and thus expected in the generic situation; an alternative route incorporates additional small s-wave pairing. In Eq. (3.11), we neglect terms cubic in $k_{x,y}$ because these do not modify the low-energy dispersion relations.

In the limit $k \to 0$, Eq. (3.11) exhibits linear and cubic bands [14]:

$$\begin{aligned}\varepsilon_1(k) &= \frac{k}{2}\left(\sqrt{1+4c^2k^2}+1\right) \simeq k + \boldsymbol{O}\left(k\right)^3, \\ \varepsilon_3(k) &= \frac{k}{2}\left(\sqrt{1+4c^2k^2}-1\right) \simeq c^2k^3 + \boldsymbol{O}\left(k\right)^5. \end{aligned} \tag{3.12}$$

Both bands become quadratic at large k. Due to the cubic band, the system has a van Hove singularity in the density of states $\nu(\varepsilon \to 0) \sim \varepsilon^{-1/3}$.

3.2.2 Surface perturbations

The Hamiltonian for the surface fermion fluid is given by

$$H_0^{(\mathsf{S})} = \frac{1}{2}\int d^2\mathbf{r}\,\eta^{\mathsf{T}}\,\hat{M}_{\mathsf{P}}^{(\mathsf{S})}\,\hat{h}_{\mathsf{s}}\,\eta, \tag{3.13}$$

where $\eta \to \eta_{m_s}$ is a four-component Majorana spinor and $\mathbf{r}$ is the position vector. Local bilinear ("potential") perturbations must obey surface particle-hole symmetry. There are 6 Hermitian terms without derivatives of the form $\frac{1}{2}\int d^2\mathbf{r}\,\eta^{\mathsf{T}}\,\hat{M}_{\mathsf{P}}^{(\mathsf{S})}\,\hat{\Lambda}\,\eta$, where $\Lambda \in \{\hat{\tau}^{1,2,3}\}$ or $\{\hat{\kappa}^{1,2,3}\}$ satisfies Eq. (3.10). These are classified by symmetry.

Under planar rotations, $\hat{\tau}^3$ and $\hat{\kappa}^3$ are scalars, $\hat{\kappa}^{1,2}$ transform like a vector, and $\hat{\tau}^{1,2}$ transform like second-rank tensor components. Only $\hat{\tau}^{1,2}$ are time-reversal even [Eq. (3.10)]; the rest are odd.

A generic combination $\hat{\Lambda} = m_1\,\hat{\tau}^3 + m_2\,\hat{\kappa}^3$ breaks time-reversal and induces a gapped surface thermal quantum Hall (TQH) state [19, 6]. We compute the *surface winding number* W using the Green's function [8]; the result is shown in Fig. 3.2. The lines $m_1 = \pm m_2$ are gapless surface plateau transitions. The maximum winding number and surface gap for fixed $\sqrt{m_1^2 + m_2^2}$ is achieved for $|m_1| > |m_2|$, i.e. $\hat{\tau}^3$ order. Finally, we note that the spin operator $\hat{S}^z$ corresponds to $m_1 = 2m_2$, so that an external Zeeman field would induce the $W = \pm 2$ plateaux.

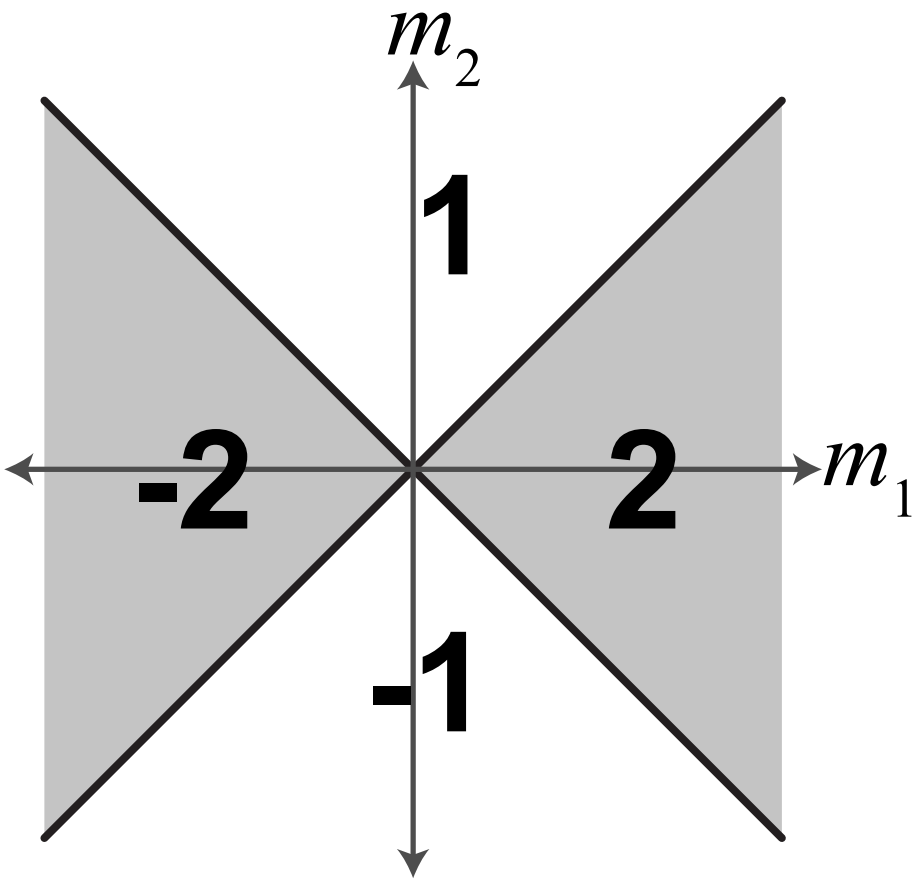

Figure 3.2: Phase diagram of the clean spin-3/2 Majorana surface fluid in the presence of time-reversal symmetry-breaking mass terms m_1 and m_2. All states are TQHE plateaux with winding number as indicated, computed via the surface Green's function [8]. The combination $m_2 = m_1/2$ corresponds to the spin-3/2 operator $\hat{S}^z$, as could be introduced via Zeeman coupling to an external magnetic field. The conditions $m_1 = \pm m_2$ are gapless plateau transitions.

3.2.3 Marginal instability of the clean surface

Although we treat the gapped bulk as an effectively non-interacting mean field Hamiltonian, we must consider the effects of residual interactions on the surface Majorana fluid carefully. This is because the latter is gapless and exhibits a diverging density of states. In a superconductor, interactions at the surface are expected to be short-ranged due to screening by the bulk. These residual interactions can be mediated by virtual fluctuations of the "massive" electromagnetic field. Here we posit the form of the interactions based on symmetry and Pauli exclusion.

Because η is a four-component Majorana field, there is only a single interaction term without derivatives that we can write; others with derivatives are less relevant. Labeling the components as $\eta \to \eta_{1,2,3,4}$,

$$\begin{aligned} H_I^{(\mathsf{S})} \equiv & \quad u \int d^2\mathbf{r}\, \eta_1\eta_2\eta_3\eta_4 \\ = & \quad \mp\tfrac{u}{8} \int d^2\mathbf{r}\, (\eta^{\mathsf{T}}\, \hat{M}_{\mathsf{P}}^{(\mathsf{S})}\, \hat{\Lambda}\, \eta)^2, \end{aligned} \tag{3.14}$$

where the minus (plus) sign corresponds to $\hat{\Lambda} = \hat{\tau}^3$ ($\hat{\kappa}^3$). Thus $u > 0$ is an attractive (repulsive) interaction in the $\hat{\tau}^3$ ($\hat{\kappa}^3$) channel. The coupling u has units of length. The sign of u could be determined by integrating out the bulk superfluid and the electromagnetic field, but we will not do so here.

Given that the noninteracting surface fluid has coexisting linear and cubic bands, it is not a priori obvious how to assess the relevance of u from a renormalization group (RG) perspective. Moreover, the van Hove singularity suggests that nonzero u will induce bad infrared behavior. In fact one-loop perturbation theory gives the

simple vertex correction,

$$\Gamma^{(4)} = -\left[u + \left(u^2/4\pi c\right)\ln(4c\Lambda)\right], \tag{3.15}$$

where Λ is the ultraviolet momentum cutoff. The correction is only logarithmic, and is cut in the infrared by the length scale c. This immediately implies the beta function,

$$\frac{d\tilde{u}}{dl} = \frac{\tilde{u}^2}{4\pi} + \boldsymbol{O}\left(\tilde{u}^3\right), \tag{3.16}$$

where $\tilde{u} = u/c$ is the dimensionless coupling.

The absence of bad infrared behavior in Eq. (3.15) and the weakness of the ultraviolet singularity is due to Pauli exclusion, i.e. the fact that both linear and cubic components of the Majorana Green's function must appear simultaneously in the loop. Eq. (3.16) implies that $u > 0$ is a marginally relevant perturbation. Eq. (3.14) suggests a natural interpretation in terms of TQH order with surface winding number $W = \pm 2$.

We can confirm this picture with a mean-field calculation. We decouple the interaction in Eq. (3.14) with the order parameter $\mathcal{M} \equiv (u/2)\left\langle \eta^{\mathsf{T}}\, \hat{M}_{\mathsf{P}}^{(\mathsf{S})}\, \hat{\tau}^3\, \eta \right\rangle$. Zero-temperature mean-field theory gives

$$\mathcal{M} \simeq \frac{1}{c}\left(\frac{4.4}{2\pi}\right)^3 \frac{1}{\left[(2\pi/\tilde{u}) - \ln(c\Lambda)\right]^3}, \quad \tilde{u} \ll 1. \tag{3.17}$$

Physically we can associate nonzero $\mathcal{M}$ with *surface* "i s" (imaginary s-wave) pairing of the Majorana particles [10, 11, 27]. This can be understood via the following argument. In the bulk, one can write a local spin singlet, time-reversal odd

pairing operator

$$[-ic^\dagger \hat{R} \left(c^\dagger\right)^{\mathsf{T}} + \text{H.c.}] = \chi^\dagger \hat{\sigma}^1 \chi. \tag{3.18}$$

Eq. (3.8) implies that this bilinear projects to $\eta^{\mathsf{T}} \hat{M}_{\mathsf{P}}^{(\mathsf{S})} \hat{\tau}^3 \eta \propto \mathcal{M}$ at the surface. On the other hand, Eq. (3.14) can also be written as proportional to $-u \int d^2\mathbf{r} \, (\hat{S}^z)^2$, implying surface magnetic order for $u > 0$. Indeed, these disparate orders are unified in the surface fluid, due to the strong spin-orbit coupling in the bulk and the locking condition [Eq. (3.8)]. We might anticipate a generic order parameter of the form $\hat{\Lambda} = m_1 \, \hat{\tau}^3 + m_2 \, \hat{\kappa}^3$ [c.f. Fig. 3.2] with $|m_1| > |m_2|$. Although we are confident that the surface resides in the $W = +2$ or -2 plateau for $u > 0$, there are hints that mean-field theory fails to correctly predict the admixture of m_1 and m_2. For details, see Sec. 3.3.4, below.

3.2.4 Quenched disorder and universal surface quantum criticality

In a solid state realization, quenched disorder due to impurities and other defects is inevitable at the sample surface. Now we consider the effects of disorder on the non-interacting surface states.

We add real disorder potentials that couple to the time-reversal symmetric bilinear perturbations $\hat{\tau}^{1,2}$ to Eq. (3.11):

$$\hat{h}_{\mathsf{s}} \to \hat{h}_{\mathsf{s}} + P_1(\mathbf{r}) \, \hat{\tau}^1 + P_2(\mathbf{r}) \, \hat{\tau}^2 =$$

$$\begin{bmatrix} 0 & 0 & c(-i\partial)^2 + \mathsf{P}(\mathbf{r}) & 0 \\ 0 & 0 & \partial & c(-i\partial)^2 + \mathsf{P}(\mathbf{r}) \\ c(-i\bar{\partial})^2 + \bar{\mathsf{P}}(\mathbf{r}) & -\bar{\partial} & 0 & 0 \\ 0 & c(-i\bar{\partial})^2 + \bar{\mathsf{P}}(\mathbf{r}) & 0 & 0 \end{bmatrix}, \quad (3.19)$$

where $\{\partial, \bar{\partial}\} = \partial_x \mp i\partial_y$ and $\{\mathsf{P}, \bar{\mathsf{P}}\} = P_1 \mp iP_2$. We consider only time-reversal invariant disorder; equivalently, we require that there are no magnetic fields or magnetic impurities at the surface. We assume Gaussian white noise disorder potentials $P_{1,2}(\mathbf{r})$ with common variance given by a dimensionless parameter λ. Due to the cubic dispersion, even weak disorder is expected to produce a strong effect. Indeed, perturbative renormalization of λ produces a quadratic infrared divergence, and implies that λ/c^2 is the effective disorder strength. This has dimension 2 and thus corresponds to a strongly relevant perturbation of the clean surface band structure. To treat the disorder nonperturbatively, we diagonalize Eq. (3.19) numerically. The calculation is performed in momentum space to avoid fermion doubling issues [12]. Details are described in Sec. 3.4.2, below.

In spin-1/2 bulk TSCs with relativistic surface fluids, conformal embedding rules establish certain 2+0-D conformal field theories (CFTs) as governing the properties of disordered, noninteracting surface states [11]. For a class DIII bulk with winding number 4, that theory would predict the surface CFT $\mathrm{SO}(n)_4$, where $n \to 0$ counts replicas. We will demonstrate that this theory also governs the dirty surface states of the spin-3/2 TSC.

The $\mathrm{SO}(n)_4$ theory predicts [11] a diverging low-energy global density of states (DoS) $\nu(\varepsilon) \sim \varepsilon^{-1/5}$. Note that this is a weaker power law than the 1/3 van Hove

singularity in the clean system. In Fig. 3.3, we compare numerical results for different disorder strengths to the CFT prediction for the integrated DoS $N(\varepsilon) \equiv \int_0^\varepsilon d\varepsilon'\, \nu(\varepsilon')$. We find good agreement irrespective of the disorder strength.

The disorder-induced spatial fluctuations of the critical surface wave functions are encoded in the multifractal spectrum $\tau(q)$. (For a recent review on multifractality at Anderson metal-insulator transitions, see, e.g., Ref. [28].) The $\mathrm{SO}(n)_4$ theory predicts an exactly quadratic spectrum [11] for the low-energy wavefunctions,

$$\tau(q) = (q-1)\,(2 - q/2)\,, \qquad |q| \leq 2. \tag{3.20}$$

Fig. 3.4 compares Eq. (3.20) to the numerical results.

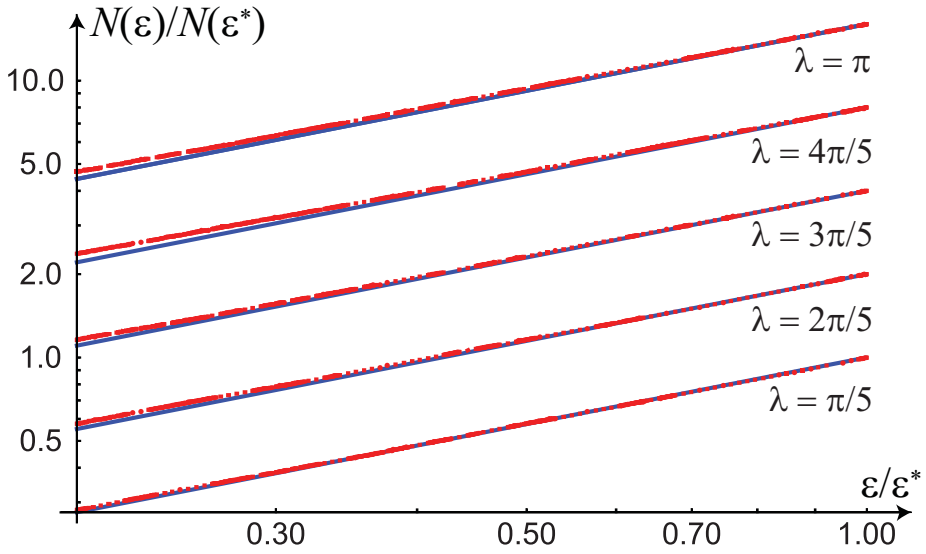

Figure 3.3: Numerical evidence for critical surface delocalization in the presence of quenched disorder I: Integrated local density of states (IDoS) $N(\varepsilon)$. The exact prediction of the SO$(n)_4$ theory gives $N(\varepsilon) \sim \varepsilon^{4/5}$ (blue solid lines). The clean theory has $N(\varepsilon) \sim \varepsilon^{2/3}$ due to the van Hove singularity. Data (red dotted lines) is obtained from momentum-space exact diagonalization of the dirty surface Hamiltonian, without interactions. Results are presented for typical realizations of the disorder (i.e., there is no disorder-averaging). Curves with different disorder strengths λ are labeled and shifted vertically for clarity. The system size consists of an 81×81 grid of momenta. Irrespective of the nonzero disorder strength, the same critical scaling exponent is observed and is consistent with the SO$(n)_4$ theory.

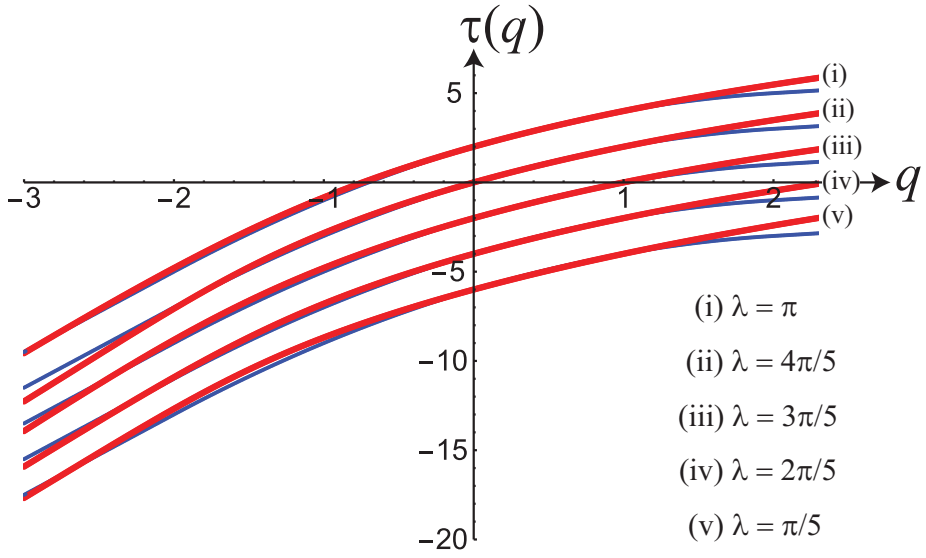

Figure 3.4: Numerical evidence for critical surface delocalization in the presence of quenched disorder II: Multifractal spectrum (No unit, no unit is reported for the multifractal spectrum throughout this dissertation). The exact prediction of the $SO(n)_4$ theory gives Eq. (3.20) (blue). The clean theory would have $\tau(q) = 2(q-1)$. Data [red, labeled (i)–(v)] is obtained as in Fig. 3.3. The disorder strengths λ are indicated for the numerical curves. Curves with different disorder strengths are shifted vertically for clarity. The largest deviation occurs for $|q| > q_c$, where $q_c = 2$ is the multifractal termination threshold [29, 28, 30]. This is a finite resolution effect, since the slopes beyond q_c are governed by the peaks and valleys of the wave function.

Figs. 3.3 and 3.4 provide strong evidence that the disordered, noninteracting spin-3/2 Majorana fluid is governed by the $SO(n)_4$ theory. This is surprising because a standard derivation [24] of the disorder-induced effective field theory would predict a thermal metal phase exhibiting weak antilocalization. Although the theory in

[24] should be augmented by a Wess-Zumino-Novikov-Witten term (see Sec. 3.4.1 for details), this term does not alter the tendency towards antilocalization in the metallic phase [11]. Because the clean density of states diverges for the surface Majorana fluid studied here, a diffusive metallic state would be generically expected. Yet this is inconsistent with our numerical results [which instead match the $\mathrm{SO}(n)_4$ CFT]. An important technical point is that the CFT is *unstable* to the thermal metal phase [see Eq. (3.43)]. It means that the CFT can only be realized if the system is tuned to the $\mathrm{SO}(n)_4$ fixed point. Our numerical results imply that this is exactly what happens.

The same "fine-tuning" is required for the spin-1/2 TSCs. In that case, however, there is a nonperturbative argument for it using conformal embedding theory [11]. Additional evidence in the spin-1/2 case obtains by comparing interaction (Altshuler-Aronov) corrections to transport via two methodologies: (1) order-by-order in the interaction strength, in a *fixed realization* of disorder, and (2) within a disorder-averaged large winding number expansion. These give the same result only if the disorder-averaged system is tuned to the CFT (in which case Altshuler-Aronov corrections vanish) [13]. We do not have the conformal embedding dictionary [11] utilized for spin-1/2 TSCs, but our numerical results empirically suggest that there is an equivalence between the bulk topology and the CFT describing the *disordered surface* of a TSC [11, 12, 13], despite the fact that the clean surface theories can fundamentally differ.

3.2.5 Stability, phase diagram, and quantized thermal conductivity

We have seen that the clean surface is marginally unstable to TQH order. We have also shown that quenched disorder is a strong perturbation that drives the non-interacting surface to a phase described by the $\mathrm{SO}(n)_4$ CFT. It is known [11] that interactions are strongly irrelevant to this CFT,

$$\frac{d\tilde{u}}{dl} = -\frac{\tilde{u}}{2} + \boldsymbol{O}\left(\tilde{u}^2\right), \tag{3.21}$$

where $\tilde{u}$ is the dimensionless coupling strength. Although multifractality can sometimes enhance interactions [31, 32, 10], that does not occur here. The reason is again Pauli exclusion: the interaction and second multifractal moment operators are distinct due to the complete antisymmetrization of the former [11]. We therefore conclude that disorder stabilizes the surface Majorana fluid of this spin-3/2 TSC. This is our most important result. We note that Eq. (3.21) technically obtains from the *dynamical version* of the $\mathrm{SO}(n)_4$ theory. This is a 2+1-D theory of Majorana fermions propagating in space and time, whose disorder-averaged spatial correlations and dynamical scaling exponent are governed by the 2+0-D replicated CFT, see [11] for details. Thus in Fig. 3.1, "$\mathrm{SO}(n)_4$" really refers to this dynamical hybrid theory, which can also be expressed as a Wess-Zumino-Novikov-Witten Finkel'stein nonlinear sigma model (WZNW-FNLsM) [11, 13].

The thermal conductivity of the WZNW-FNLsM receives no quantum interference corrections due to disorder [9, 13] at the conformal fixed point. Interaction-mediated Altshuler-Aronov corrections also vanish to at least order $1/|\nu|$, where ν

is the bulk winding number. The absence of Friedel oscillations in any Majorana surface "density" implies that these should be absent to all orders [13]. Since the spin-3/2 Majorana surface fluid studied here realizes the $\mathrm{SO}(n)_4$ theory in the presence of disorder, we conclude that the ratio of the longitudinal thermal conductivity and temperature is precisely quantized as $T \to 0$ [Eq. (3.83)].

3.3 Ideal (clean) surface states and interactions

3.3.1 Derivation of the surface Hamiltonian Eq. (4.1)

3.3.1.1 Luttinger Hamiltonian bulk

To obtain the surface Hamiltonian, we consider a bulk superconductor in the half space $z \geq 0$ with hard wall boundary conditions. We divide Eq. (3.3) into two parts:

$$\hat{h} = \hat{h}_0(-i\partial_z) + \hat{h}_1(\mathbf{k}, -i\partial_z),$$

$$\hat{h}_0 = \hat{\sigma}^3\left(-\partial_z^2 - \mu\right) + \hat{\sigma}^2\left[\Delta_p \hat{S}^z\left(-i\partial_z\right) + \Delta_s\right], \tag{3.22a}$$

$$\hat{h}_1 = \hat{\sigma}^3\left\{k^2 - \gamma\left[\tfrac{1}{2}\left(\hat{S}^+\mathsf{k} + \hat{S}^-\bar{\mathsf{k}}\right) + \hat{S}^z(-i\partial_z)\right]^2\right\} + \hat{\sigma}^2\tfrac{\Delta_p}{2}\left(\hat{S}^+\mathsf{k} + \hat{S}^-\bar{\mathsf{k}}\right), \tag{3.22b}$$

where $\mathbf{k} = \{k_{x,y}\}$ is the momentum parallel to the surface, $\{\mathsf{k}, \bar{\mathsf{k}}\} = k_x \mp i k_y$, and $\hat{S}^\pm = \hat{S}^x \pm i\hat{S}^y$ are spin-3/2 raising and lowering operators. In Eq. (3.22a), we have added a time-reversal symmetric s-wave pairing term proportional to Δ_s. We will utilize this below in the case of vanishing bulk spin-orbit coupling (SOC). Energies like Δ_s and μ have units of $1/(\text{length})^2$, while Δ_p has units of $1/\text{length}$.

In this subsection we will ignore s-wave pairing ($\Delta_s = 0$) and we will treat the

SOC term proportional to γ as a small perturbation (although this is not necessary). The surface eigenstates of $\hat{h}_0$ with zero transverse momentum satisfy $\hat{h}_0|\psi_{0,m_s}\rangle = 0$ and take the form shown in Eq. (3.8),

$$\psi_{0,m_s}(z) = f_{m_s}(z) \begin{bmatrix} 1 \\ \mathrm{sgn}(m_s) \end{bmatrix} |m_s\rangle,\ f_{m_s}(z) = \frac{1}{\sqrt{\mathcal{N}_{m_s}}} \exp\left(-\frac{\Delta_p |m_s| z}{2}\right) \times \sin\left[z\sqrt{\mu - \frac{\Delta_p^2 m_s^2}{4}}\right]. \quad (3.23)$$

Here the explicit 2-component spinor resides in particle-hole (σ) space; the four zero energy states are distinguished by their $\hat{S}^z$ eigenvalues $m_s \in \{\pm\frac{3}{2}, \pm\frac{1}{2}\}$. The particle-hole spinor is "locked" to the physical spin, as it points along the $+\sigma^1$ ($-\sigma^1$) direction for positive (negative) m_s. The form of the envelope function $f_{m_s}(z)$ is appropriate for the weak pairing limit, $(3\Delta_p/4)^2 < \mu$.

To obtain the effective surface Hamiltonian for nonzero transverse momentum, we diagonalize $\hat{h}_1$ in the basis of zero modes given by Eq. (3.23). The only non-vanishing elements obtain from

$$\hat{h}_1 \to \hat{\sigma}^2 \frac{\Delta_p}{2} \left(\hat{S}^+ \mathsf{k} + \hat{S}^- \bar{\mathsf{k}}\right) - \hat{\sigma}^3 \frac{\gamma}{4} \left[(\hat{S}^+)^2 \mathsf{k}^2 + (\hat{S}^-)^2 \bar{\mathsf{k}}^2\right]. \quad (3.24)$$

The first term connects the $\pm 1/2$ states, giving the $\{\mathsf{k}, \bar{\mathsf{k}}\}$-linear terms in Eq. (3.11). The second term mixes the $\{3/2, -1/2\}$ and $\{1/2, -3/2\}$ states, giving the $\{\mathsf{k}^2, \bar{\mathsf{k}}^2\}$ terms in Eq. (3.11). The parameter $c \propto -\gamma/\Delta_p$.

3.3.1.2 Vanishing SOC in the bulk

If the SOC parameter $\gamma = 0$, then the $\pm 3/2$ surface bands remain flat in degenerate perturbation theory. Another way to get nonzero c in Eq. (3.11) is by incorporating

an additional weak s-wave pairing amplitude Δ_s, as in Eq. (3.22a). Then the zero energy surface eigenstates with vanishing transverse momentum again take the form shown in Eq. (3.23), but with the modified envelope function

$$f_{m_s}(z) = \frac{1}{\sqrt{\mathcal{N}_{m_s}}} \exp\left(-\tfrac{\Delta_p |m_s| z}{2}\right) \sinh\left[z\sqrt{\tfrac{\Delta_p^2 m_s^2}{4} - \mu - i\Delta_s \operatorname{sgn}(m_s)}\right]. \quad (3.25)$$

Here we assume that $0 < \Delta_s \ll \Delta_p^2$ (so as to remain in the bulk topological phase with winding number $\nu = 4$ [14]). For convenience, we also assume intermediate strength pairing such that $0 < \mu < (\Delta_p/4)^2$; in this case there is only one branch of bulk scattering states.

To obtain the effective surface Hamiltonian for nonzero transverse momentum, we use k·p theory. The matrix elements of $\hat{h}_1$ [Eq. (3.22b) with $\gamma = 0$] give the $\{\mathsf{k}, \bar{\mathsf{k}}\}$-linear terms in Eq. (3.11), which connect the $m_s = \pm 1/2$ states. To connect the $\pm 3/2$ states to the former, one has to go to second order. This yields the matrix elements [34]

$$-\langle \psi_{0,m_s} | \hat{h}_1(\mathbf{k})\, \hat{P}\, \hat{h}_0^{-1}\, \hat{P}\, \hat{h}_1(\mathbf{k}) | \psi_{0,m_s'} \rangle, \quad (3.26)$$

where $\hat{P}$ projects out of the degenerate zero mode space. Eq. (3.26) can be expressed using the basis of bulk scattering states with zero transverse momentum:

$$\begin{aligned} \langle \psi_{0,m_s} | \hat{h}_1(\mathbf{k})\, \hat{P}\, \hat{h}_0^{-1}\, \hat{P}\, \hat{h}_1(\mathbf{k}) | \psi_{0,m_s'} \rangle \quad &= \textstyle\sum_{m_s''} \int_0^\infty \frac{dq}{\varepsilon_{m_s''}(q)} \langle \psi_{0,m_s} | \hat{h}_1(\mathbf{k}) | \psi_{q,m_s''} \rangle \times \\ &\langle \psi_{q,m_s''} | \hat{h}_1(\mathbf{k}) | \psi_{0,m_s'} \rangle + \langle \psi_{0,m_s} | \hat{h}_1(\mathbf{k})\, \hat{\sigma}^2 \hat{R} | \psi^*_{q,m_s''} \rangle \times \\ &\langle \psi^*_{q,m_s''} | \hat{\sigma}^2 \hat{R}\, \hat{h}_1(\mathbf{k}) | \psi_{0,m_s'} \rangle \end{aligned} \quad (3.27)$$

where $|\psi_{q,m_s''}\rangle$ denotes a scattering state with standing wave momentum q (oscillation in the z-direction), $\hat{S}^z$-eigenvalue m_s'', and gapped positive energy eigenvalue $\varepsilon_{m_s''}(q)$,

while $\hat{\sigma}^2\hat{R}|\psi^*_{q,m''_s}\rangle$ is the (negative energy) particle-hole conjugate of $|\psi_{q,m''_s}\rangle$. The matrix $\hat{R}$ was introduced in Eq. (3.7).

The scattering states take the form

$$\psi_{q,m_s}(z) = \frac{1}{\sqrt{\mathcal{N}_{q,m_s}}}\left\{\hat{\alpha}_{q,m_s}\left[\cos(qz) - e^{-\lambda_{q,m_s}z}\right] + \hat{\beta}_{q,m_s}\,\sin(qz)\right\}|m_s\rangle, \qquad (3.28)$$

where $\hat{\alpha}_{q,m_s}$ and $\hat{\beta}_{q,m_s}$ are 2-component spinors in particle-hole space. The expressions for these and λ_{q,m_s} are unwieldy so we omit them here.

Finally, one computes Eq. (3.27) using Eqs. (3.8), (3.25), and (3.28). This second-order result *vanishes* for $\Delta_s = 0$. Nonzero c in Eq. (3.11) is symmetry allowed, and thus expected in the generic situation. The simplest way to get it is by retaining nonzero Δ_s in the bound states $\{|\psi_{0,m_s}\rangle\}$, but neglecting it in the scattering states $\{|\psi_{q,m_s}\rangle\}$ (which become very complicated for $\Delta_s \neq 0$). This gives nonzero terms mixing the $\{3/2, -1/2\}$ and $\{1/2, -3/2\}$ states proportional to k^2 and $\bar{\mathsf{k}}^2$ in $\hat{h}_{\mathsf{s}}$ (above and below the diagonal, respectively, consistent with planar rotational invariance). Without loss of generality, we can take the coefficients to be real and positive since the phases can be removed with a unitary transformation.

3.3.2 Calculation of the surface winding number in Fig. 3.2

We compute the surface winding number W for the clean, noninteracting Majorana surface fluid perturbed by time-reversal breaking "mass" terms. The Hamiltonian is

$$\hat{h}_{m_1,m_2}(\mathbf{k}) \equiv \hat{h}_{\mathsf{s}}(\mathbf{k}) + m_1\,\hat{\tau}^3 + m_2\,\hat{\kappa}^3, \qquad (3.29)$$

where $\hat{h}_{\mathsf{s}}$ was defined by Eq. (3.11). The energy bands of $\hat{h}_{m_1,m_2}(\mathbf{k})$ are gapped for non-zero values of $m_{1,2}$ unless $m_1 = \pm m_2$, in which case a gapless linear Dirac point appears at $\mathbf{k} = 0$.

Because the mass terms break surface time-reversal symmetry [Eq. (3.9)], the surface theory resides in class D [9]. In 2D, this class can exhibit a thermal quantum Hall effect [18, 19, 20], where edge states carry a quantized energy current. The thermal Hall conductivity κ_{xy} can be expressed in terms of a winding number W via [21, 6]

$$\kappa_{xy} = W\,\kappa_{\circ}, \tag{3.30}$$

where $\kappa_{\circ}$ was defined by Eq. (3.81). In terms of the surface Green's function

$$\hat{G}(\omega, \mathbf{k}, m_1, m_2) \equiv \left[-i\,\omega\,\hat{1} + \hat{h}_{m_1,m_2}(\mathbf{k})\right]^{-1}, \tag{3.31}$$

the winding number is given by [8]

$$W(m_1, m_2) \equiv \frac{\epsilon_{\alpha\beta\gamma}}{3!(2\pi)^2} \int_{-\infty}^{\infty} d\omega \int_{\mathbb{R}^2} d^2\mathbf{k}\ \mathrm{Tr}\left[\left(\hat{G}^{-1}\partial_\alpha \hat{G}\right)\left(\hat{G}^{-1}\partial_\beta \hat{G}\right)\left(\hat{G}^{-1}\partial_\gamma \hat{G}\right)\right], \tag{3.32}$$

where Tr denotes the trace over spin-3/2 components and $\alpha, \beta, \gamma \in \{\omega, k_x, k_y\}$. Numerical evaluation of Eq. (3.32) using Eqs. (3.29) and (3.31) leads to the winding number results shown in Fig. 3.2.

3.3.3 Perturbative vertex renormalization

The imaginary time action for the clean, time-reversal invariant, interacting Majorana surface theory implied by Eqs. (3.11) and (3.14) is given by

$$S = \frac{1}{2}\int \frac{d\omega\, d^2\mathbf{k}}{(2\pi)^3} \eta^{\mathsf{T}}(-\omega, -\mathbf{k})\, \hat{M}_{\mathsf{P}}^{(\mathsf{S})} \left[-i\omega + \hat{h}_{\mathsf{s}}(\mathbf{k})\right] \eta(\omega, \mathbf{k}) + \frac{u}{4!}\int d\tau\, d^2\mathbf{r}\, \epsilon_{i_1 i_2 i_3 i_4}\, \eta_{i_1}\, \eta_{i_2}\, \eta_{i_3}\, \eta_{i_4},$$

(3.33)

where we have antisymmetrized the four-fermion interaction using the fourth-rank Levi-Civita tensor. Repeated indices are summed.

To one loop, the bare vertex function evaluates to

$$\begin{aligned}(\Gamma^{(4)})_{i_1 i_2 i_3 i_4} = -u\,\epsilon_{i_1 i_2 i_3 i_4} + \frac{u^2}{2} \quad & [\epsilon_{i_1 i_2 j_1 j_2}\epsilon_{j_3 j_4 i_3 i_4} + \epsilon_{i_1 i_3 j_1 j_2}\epsilon_{j_3 j_4 i_4 i_2} + \epsilon_{i_1 i_4 j_1 j_2}\epsilon_{j_3 j_4 i_2 i_3}] \\ & \times \int \tfrac{d\omega\, d^2\mathbf{k}}{(2\pi)^3} \left[\hat{G}\hat{M}_{\mathsf{P}}^{(\mathsf{S})}\right]_{j_1 j_3}(\omega, \mathbf{k}) \left[\hat{G}\hat{M}_{\mathsf{P}}^{(\mathsf{S})}\right]_{j_4 j_2}(\omega, \mathbf{k}),\end{aligned} \tag{3.34}$$

valid in the limit of vanishing external frequencies and momenta. The three double Levi-Civita terms in the square brackets correspond to the three loop corrections shown in Fig. 3.5. We emphasize that the sign of each diagram has to be carefully determined using Wick's theorem for the Majorana fermion field. The Green's function $\hat{G}(\omega, \mathbf{k})$ is given by Eq. (3.31) with $m_1 = m_2 = 0$, while $\hat{M}_{\mathsf{P}}^{(\mathsf{S})}$ was defined by Eq. (3.10).

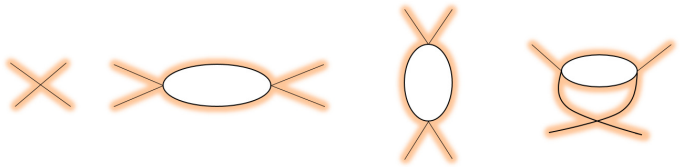

Figure 3.5: Feynman diagrams for the one-loop vertex corrections.

We define

$$D(\omega, k) \equiv c^4 k^8 + 2c^2 k^4 \omega^2 + k^2 \omega^2 + \omega^4$$

and

$$\mathcal{N}_{i_1 i_2 i_3 i_4}(\omega,k) \equiv \int_0^{2\pi} d\phi_k \, D^2(\omega,k) \, \left[\hat{G}\hat{M}_{\mathsf{P}}^{(\mathsf{S})}\right]_{i_1 i_2}(\omega,k,\phi_k) \, \left[\hat{G}\hat{M}_{\mathsf{P}}^{(\mathsf{S})}\right]_{i_3 i_4}(\omega,k,\phi_k), \quad (3.35)$$

where we have switched to polar momentum coordinates $\mathbf{k} \to (k,\phi_k)$. Next we compute

$$\frac{1}{2}\left[\epsilon_{i_1 i_2 j_1 j_2}\epsilon_{j_3 j_4 i_3 i_4} + \epsilon_{i_1 i_3 j_1 j_2}\epsilon_{j_3 j_4 i_4 i_2} + \epsilon_{i_1 i_4 j_1 j_2}\epsilon_{j_3 j_4 i_2 i_3}\right]\mathcal{N}_{j_1 j_3 j_4 j_2}(\omega \equiv ck^2 x, k)$$
$$= -4c^4 k^{10}\pi\left[x^2 + c^2 k^2 (1+x^2)^2\right]\epsilon_{i_1 i_2 i_3 i_4}. \quad (3.36)$$

Thus Eq. (3.34) reduces to

$$\begin{aligned}(\Gamma^{(4)})_{i_1 i_2 i_3 i_4} &= -\epsilon_{i_1 i_2 i_3 i_4}\left\{u + u^2 \int_{-\infty}^{\infty} dx \int_0^{\Lambda} dk \, \tfrac{(ck^3)4c^4k^{10}\pi}{2^3\pi^3} \, \tfrac{\left[x^2+c^2k^2(1+x^2)^2\right]}{D^2(ck^2x,k)}\right\} \\ &= -\epsilon_{i_1 i_2 i_3 i_4}\left\{u + \tfrac{u^2}{4\pi c}\ln\left[\sqrt{(2c\Lambda)^2+1} + 2c\Lambda\right]\right\}, \end{aligned} \quad (3.37)$$

where Λ denotes the ultraviolet momentum cutoff. Taking the limit $c\Lambda \gg 1$ gives Eq. (3.15).

3.3.4 Mean-field theory: surface thermal quantum Hall plateaux

The interaction strength u is enhanced (suppressed) by quantum fluctuations for $u > 0$ ($u < 0$) [Eq. (3.16)]. In Eq. (3.14) and the text following, it is noted that $u > 0$ is an attractive (repulsive) interaction in the "$\hat{\tau}^3$" ("$\hat{\kappa}^3$") channel, where these matrices specify mass terms used to construct the thermal quantum Hall phase diagram shown in Fig. 3.2. We therefore expect that spontaneous symmetry breaking

due to quantum fluctuations for positive u can be characterized by an order parameter

$$\mathcal{M} \equiv \frac{u}{2(1-2\alpha)} \left\langle \eta^{\mathsf{T}} \hat{M}_{\mathsf{P}}^{(\mathsf{S})} \hat{\Lambda}_\alpha \eta \right\rangle, \tag{3.38}$$

where

$$\hat{\Lambda}_\alpha \equiv (1-\alpha)\hat{\tau}^3 + \alpha\hat{\kappa}^3 \tag{3.39}$$

and α is a real variational parameter. In terms of Majorana (spin-3/2) components,

$$\frac{1}{2}\eta^{\mathsf{T}} \hat{M}_{\mathsf{P}}^{(\mathsf{S})} \hat{\Lambda}_\alpha \eta = \eta_1\eta_4 + (1-2\alpha)\,\eta_3\eta_2. \tag{3.40}$$

The interaction in Eq. (3.14) can be written as

$$H_I^{(\mathsf{S})} = -\frac{(1-2\alpha)}{2u} \int d^2\mathbf{r} \left\{ \mathcal{M} + \left[\frac{u}{2(1-2\alpha)} \eta^{\mathsf{T}} \hat{M}_{\mathsf{P}}^{(\mathsf{S})} \hat{\Lambda}_\alpha \eta - \mathcal{M} \right] \right\}^2. \tag{3.41}$$

The interaction is attractive for $u > 0$ so long as $0 \leq \alpha < 1/2$. Precisely for $\alpha = 1/2$, Eq. (3.40) implies that $\left(\frac{1}{2}\eta^{\mathsf{T}} \hat{M}_{\mathsf{P}}^{(\mathsf{S})} \hat{\Lambda}_\alpha \eta\right)^2 = 0$ due to Pauli exclusion (neglecting nontrivial anticommutators). In this case the interaction cannot be written as the square of the bilinear.

The zero temperature mean-field condensation energy density is given by

$$\Delta\mathcal{E}(\mathcal{M}) = \quad (1-2\alpha)\tfrac{\mathcal{M}^2}{u} - \tfrac{1}{2\pi}\textstyle\int_0^\Lambda k dk \left\{ [\varepsilon_1(k,\mathcal{M}) - \varepsilon_1(k,0)] + [\varepsilon_3(k,\mathcal{M}) - \varepsilon_3(k,0)] \right\}, \tag{3.42}$$

where $\varepsilon_1(k,\mathcal{M})$ and $\varepsilon_3(k,\mathcal{M})$ denote the linear and cubic surface band energies modified by the addition of the term $\mathcal{M}\,\hat{\Lambda}_\alpha$ to $\hat{h}_{\mathsf{s}}$ in Eq. (3.11); $\varepsilon_1(k,0)$ and $\varepsilon_3(k,0)$ are the unperturbed, gapless linear and cubic dispersion relations [Eq. (3.12)].

Setting $\alpha = 0$ (such that $\hat{\Lambda}_\alpha = \hat{\tau}^3$) and extremizing $\Delta\mathcal{E}(\mathcal{M})$ with respect to $\mathcal{M}$ leads to the mean-field result in Eq. (3.17), valid in the weak coupling limit $u \ll c$. Since quantum fluctuations enhance positive u and the interaction is attractive in the $\hat{\Lambda}_\alpha$ channel only for $0 \leq \alpha < 1/2$, we expect that the order is weighted towards $\hat{\tau}^3$ instead of $\hat{\kappa}^3$; the surface winding number $W = +2$ throughout this range (Fig. 3.2).

A curious aspect of Eq. (3.42) is the following. By choosing α arbitrarily close to $1/2$, we can suppress the contribution of the first term on the right-hand side of Eq. (3.42). This allows us to take larger and larger values for $\mathcal{M}$ so as to enhance the negativity of the second term. Yet it cannot be that the system wants to condense with the bilinear with $\hat{\Lambda}_\alpha = (\hat{\tau}^3 + \hat{\kappa}^3)/2$, because the interaction cannot even be written in terms of its square (as discussed above). This suggests that the true admixture of $\hat{\tau}^3$ and $\hat{\kappa}^3$ order [i.e., the value of α in the expectation value of $\mathcal{M}$ defined by Eq. (3.38)] cannot be determined by mean-field theory. This warrants further investigation, but we will not pursue it here.

3.4 Quenched disorder

3.4.1 The "standard" theory for a disordered class DIII system: thermal metal

Next we comment on the physics of the noninteracting, disordered Majorana surface fluid. Since the spin-3/2 model with surface Hamiltonian given by Eq. (3.11) has a cubic van Hove singularity, one would naively expect the "standard program" [35]

for deriving the effective low-energy field theory in the presence of disorder would apply. The steps in this program are

1. Write a (replicated) Grassmann path integral in order to compute disorder-averaged products of retarded and advanced Green's functions.

2. Average over the disorder potentials $P_{1,2}(\mathbf{r})$ in Eq. (3.19) with variance λ.

3. Decouple the four-field term using an unconstrained matrix field $\hat{Q}$.

4. Integrate out the Grassmann field.

5. Compute the saddle-point configuration of $\hat{Q}$, the strength of which is the self-consistent Born approximation for the elastic scattering rate. This should smear out the van Hove singularity in the clean density of states.

6. Perform a gradient expansion and integrate out massive modes to get the non-linear sigma model for the constrained matrix field $\hat{Q}$ in the appropriate symmetry class. Fluctuations due to quantum interference are controlled by the (inverse of the) coupling constant G, which is the dimensionless charge, spin, or thermal longitudinal dc conductance (depending upon the class and context).

For a gapless, 2D class DIII Majorana system as described here, this program was carried out in a nontopological context in [24]. The resulting theory has the thermal conductance determined by the bare strength of the disorder $G \propto 1/\lambda$, and G grows with increasing system size due to weak antilocalization. Although the global density of states (DoS) diverges and wave functions are weakly multifractal, neither are universal.

Our numerical results in Figs. 3.3 and 3.4 instead imply universal behavior in the disorder-averaged DoS and multifractal spectrum for the spin-3/2 surface Majorana fluid, consistent with the $\mathrm{SO}(n)_4$ conformal field theory. Interestingly, the latter has a sigma model description (non-abelian bosonization) that is almost identical to the one obtained by the "standard program," but augmented with a Wess-Zumino-Novikov-Witten term [11]. Yet the key point is that the coupling strength is pinned to a special value equal to the winding number 4, times a universal constant. Since the winding number is not large, the field theory is strongly coupled. This is in part why the standard program fails in this case. For the spin-1/2 TSC models studied previously [10, 11, 13], a nonperturbative derivation was possible using conformal embedding theory. This is not possible in the present case, since the clean surface with Hamiltonian given by Eq. (4.1) is not a conformal field theory (as evidenced by the fact that c has units of length).

Finally, we stress an important technical point. The CFT is an *unstable* fixed point of the sigma model. In the absence of interactions, the sigma model is characterized by a single coupling strength λ, which can be understood as the dimensionless thermal resistance of the system. In the large winding number limit $|\nu| \gg 1$, it is possible to compute the beta function for λ, incorporating the WZNW term. The result is [13]

$$\frac{d\lambda}{dl} = -2\lambda^2 \left[1 - (|\nu|\lambda)^2\right], \tag{3.43}$$

valid for $\lambda \leq |\nu|$. The CFT has $\lambda = 1/|\nu|$, and this remains a fixed point to all orders in λ. However, any $\lambda < 1/|\nu|$ flows to ever smaller λ; this is the signal for weak antilocalization in the thermal metallic phase [24]. The fact that our numerical results

for the spin-3/2 Majorana surface fluid studied in this work coincide with the $\mathrm{SO}(n)_4$ fixed point implies that the topology "fine tunes" λ to its fixed point value. Since λ is an inverse conductance, it implies the quantization of the thermal conductivity [Eq. (3.2)], which remains true even when interaction (Altshuler-Aronov) corrections are taken into account [13].

3.4.2 Momentum space exact diagonalization

We consider the effective surface Hamiltonian in the presence of the most general form of time-reversal invariant disorder, as given in Eq. (3.19). For a system of finite size L, the Hamiltonian can be expressed as a sum over discrete points in momentum space:

$$H = \frac{1}{2}\int d^2\mathbf{r}\,\eta^{\mathsf{T}}(\mathbf{r})\,\hat{M}_{\mathsf{P}}^{(\mathsf{S})}\left[\hat{h}_{\mathsf{s}} + \hat{\boldsymbol{\tau}}\cdot\mathbf{P}(\mathbf{r})\right]\eta(\mathbf{r}) = \frac{1}{2}\sum_{\mathbf{n},\mathbf{m}}\eta_{-\mathbf{m}}^{T}\,\hat{M}_{\mathsf{P}}^{(\mathsf{S})}\,[\hat{h}_{\mathsf{s}}^{(P)}]_{\mathbf{m},\mathbf{n}}\,\eta_{\mathbf{n}},$$

$$[\hat{h}_{\mathsf{s}}^{(P)}]_{\mathbf{m},\mathbf{n}} \equiv \delta_{\mathbf{m},\mathbf{n}}\,\hat{h}_{\mathsf{s}}\big(\mathbf{k} = \tfrac{2\pi}{L}\mathbf{n}\big) + \hat{\boldsymbol{\tau}}\cdot\mathbf{P}_{(\mathbf{m}-\mathbf{n})}, \tag{3.44}$$

with the Fourier conventions

$$\eta_{\mathbf{n}} = \frac{1}{L}\int d^2\mathbf{r}\;e^{-i\frac{2\pi}{L}\mathbf{n}\cdot\mathbf{r}}\;\eta(\mathbf{r}),\quad \eta(\mathbf{r}) = \frac{1}{L}\sum_{\mathbf{n}}\;e^{i\frac{2\pi}{L}\mathbf{n}\cdot\mathbf{r}}\;\eta_{\mathbf{n}},$$

$$P_{\mu,\mathbf{n}} = \frac{1}{L^2}\int d^2\mathbf{r}\;e^{-i\frac{2\pi}{L}\mathbf{n}\cdot\mathbf{r}}\;P_{\mu}(\mathbf{r}),\quad P_{\mu}(\mathbf{r}) = \sum_{\mathbf{n}}\;e^{i\frac{2\pi}{L}\mathbf{n}\cdot\mathbf{r}}\;P_{\mu,\mathbf{n}}.$$

In these equations $\mathbf{n}\in\{\mathbb{Z},\mathbb{Z}\}$ and the components of P_μ are $\mu\in\{1,2\}$.

For exact diagonalization, we choose a momentum cutoff N_k and keep only those points $\mathbf{n}$ in momentum space with $-N_k \le n_i \le N_k$, for $i = 1, 2$. This choice corresponds to an energy cutoff of $\Lambda = 2\pi N_k/L$. We also approximate the Gaussian white

noise disorder potentials $P_{\mu,\mathbf{n}}$ with random-phase Gaussian amplitude distributions via

$$P_{\mu,\mathbf{n}} \Rightarrow \frac{\sqrt{\lambda}}{L} \exp\left(-\frac{\pi^2}{L^2}\xi^2\mathbf{n}^2 + i\,\theta_{\mu,\mathbf{n}}\right), \tag{3.45}$$

where λ is the dimensionless variance of the disorder, ξ is a short-distance correlation length of the order L/N_k, and $\theta_{\mu,\mathbf{n}} \in [0, 2\pi)$ is a uniformly distributed random phase angle. Because $P_\mu(\mathbf{r})$ is a real-valued disorder potential, the phases are taken to satisfy $\theta_{\mu,\mathbf{n}} = -\theta_{\mu,-\mathbf{n}}$. The random-phase approach is equivalent to the disorder-average up to finite-size corrections [12]. The resulting approximate Hamiltonian $[\hat{h}_{\mathrm{s}}^{(P)}]_{\mathbf{m},\mathbf{n}}$ is a dense numerical matrix acting on a $4(2N_k+1)^2$-dimensional Hilbert space that we diagonalize to obtain the energy values and eigenstate wave functions.

In the plots shown in Figs. 3.3 and 3.4, we set $\xi = 0.25\,(L/N_k)$ and $c = 0.078\,(L/N_k)$ (such that $2\pi N_k c/L = 0.49$ for $N_k = 40$). Our results are robust with respect to variation of the system size N_k, the correlation length ξ, and c. In our calculations, we have retained $P_{\mu,0}$ given by Eq. (3.45) with $\theta_{\mu,0} = 0$. This represents a nonzero average disorder strength proportional to $\sqrt{\lambda}$. The associated matrix bilinears $\hat{\tau}^{1,2}$ break rotational invariance. Thus, our numerical results show good agreement with the CFT even when we incorporate nonzero (but weak) average anisotropy. We have also performed calculations with $P_{\mu,0} = 0$. The results are indistinguishable.

3.5 Odd-parity pairing in the Luttinger semimetal

In this section and hereafter, we present the case of odd-parity topological superconductivity in the Luttinger semimetal where bands bending oppositely [26]. To motivate and clarify more on the Luttinger model itself, we reintroduce the model in more detail here again.

Quadratic touching of Kramers degenerate valence and conduction bands at an isolated point [taken to be the $\Gamma = (0,0,0)$ point] in the Brillouin zone in three spatial dimensions can be captured by the $k \cdot p$ Hamiltonian

$$H_L = \int \frac{d^3\mathbf{k}}{(2\pi)^3}\, \Psi_{\mathbf{k}}^{\dagger}\, \hat{h}_L(\mathbf{k})\, \Psi_{\mathbf{k}}, \tag{3.46}$$

where the four-component spinor $\Psi_{\mathbf{k}}$ is defined as

$$\Psi_{\mathbf{k}}^{\top} = \left(c_{\mathbf{k},+\frac{3}{2}}, c_{\mathbf{k},+\frac{1}{2}}, c_{\mathbf{k},-\frac{1}{2}}, c_{\mathbf{k},-\frac{3}{2}} \right). \tag{3.47}$$

Here $c_{\mathbf{k},m_s}$ is the band electron annihilation operator with spin projection $m_s \in \{3/2, 1/2, -1/2, -3/2\}$. Such quadratic touching is protected by the cubic symmetry, which restricts the form of the Luttinger Hamiltonian [36, 37] operator to

$$\begin{aligned} \hat{h}_L(\mathbf{k}) &= \left(\frac{\mathbf{k}^2}{2m_0} - \mu \right) \Gamma_0 - \frac{1}{2m_1} \sum_{a=1}^{3} d_a(\mathbf{k}) \Gamma_a \\ &- \frac{1}{2m_2} \sum_{a=4}^{5} d_a(\mathbf{k}) \Gamma_a, \end{aligned} \tag{3.48}$$

where μ is the chemical potential measured from the band touching point. The $\mathbf{d}$-vector appearing in the Luttinger Hamiltonian is given by $\mathbf{d}(\mathbf{k}) = k^2\, \hat{\mathbf{d}}(\hat{\mathbf{k}})$, where

$\hat{\mathbf{d}}(\hat{\mathbf{k}})$ is a five-dimensional unit vector that transforms in the $l = 2$ ("d-wave") representation under orbital SO(3) rotations. Its components can be constructed from the spherical harmonics $Y^m_{l=2}(\theta, \phi)$. While Γ_0 is a four-dimensional unit matrix, the five mutually anti-commuting matrices appearing in the Luttinger Hamiltonian are given by

$$\begin{gathered} \Gamma_1 = \kappa_3\sigma_2, \quad \Gamma_2 = \kappa_3\sigma_1, \quad \Gamma_3 = \kappa_2, \\ \Gamma_4 = \kappa_1, \quad \Gamma_5 = \kappa_3\sigma_3. \end{gathered} \tag{3.49}$$

Two sets of Pauli matrices $\{\kappa_\alpha\}$ and $\{\sigma_\alpha\}$, with $\alpha = 0, 1, 2, 3$ operate respectively on the sign [$\mathrm{sgn}(m_s)$] and the magnitude [$|m_s| \in \{1/2, 3/2\}$] of the spin projection m_s. The Γ matrices provide a basis for a symmetric traceless tensor operator formed from bilinear products of $j = 3/2$ matrices, and transform in the $j = 2$ representation of the spin SU(2). Consequently, the Hamiltonian in Eq. (3.48), is an A_{1g} quantity in a cubic environment. For $m_1 = m_2$, $\hat{h}_L(\mathbf{k})$ exhibits continuous SO(3) rotational invariance.

Besides five mutually anticommuting Γ matrices and the identity matrix (Γ_0), we can define ten commutators as $\Gamma_{ab} = [\Gamma_a, \Gamma_b]/(2i) \equiv -i\Gamma_a\Gamma_b$ for $a, b = 1, \cdots, 5$ with $a \neq b$ that together close the basis for all four dimensional matrices. The ten commutators are the generators of a (fictitious) SO(5) symmetry. Since $\mathbf{d}(\mathbf{k}) = 0$ at the Γ point of the Brillouin zone $\mathbf{k} = 0$, the four degenerate bands possess an emergent SU(4) symmetry at this point. However, at finite momentum such symmetry gets reduced to SU(2) $\times$ SU(2), stemming from the Kramers degeneracies of the valence and conduction bands. In addition, the Luttinger Hamiltonian is invariant under the time reversal transformation: $\mathbf{k} \to -\mathbf{k}$ and $\Psi_{\mathbf{k}} \to \Gamma_{13}\Psi_{-\mathbf{k}}$. The

anti-unitary time-reversal symmetry operator is given by $\mathcal{T} = \Gamma_1\Gamma_3 K$, where K is the complex conjugation and $\mathcal{T}^2 = -1$. The Kramers degeneracy is protected by inversion symmetry $\mathcal{P} : \mathbf{k} \to -\mathbf{k}$.

Without any loss of generality, but for the sake of technical simplicity, we work with the isotropic Luttinger model for which $m_1 = m_2 \equiv m$. The Luttinger Hamiltonian then has the alternative representation,

$$\hat{h}_L(\mathbf{k}) = \left[\left(\lambda_1 + \frac{5}{2}\lambda_2\right)k^2 - \mu\right]\Gamma_0 - 2\lambda_2\left(\mathbf{J}\cdot\mathbf{k}\right)^2, \tag{3.50}$$

with $\mathbf{J} = (J^x, J^y, J^z)$ and $\mathbf{k} = (k_x, k_y, k_z)$. Here $J^{x,y,z}$ are SU(2) generators in the 3/2 representation. The correspondence between Eqs. (3.48) and (3.50) is $\lambda_1 = (2m_0)^{-1}$, $\lambda_2 = (4m)^{-1}$. The Luttinger Hamiltonian can be diagonalized as $\mathcal{D}^\dagger\hat{H}_L(\mathbf{k})\mathcal{D}$, with the energy spectra

$$\varepsilon_{\pm,\sigma}(\mathbf{k}) = \left(\frac{\mathbf{k}^2}{2m_0} - \mu\right) \pm \frac{\mathbf{k}^2}{2m}. \tag{3.51}$$

Here $+$ $(-)$ corresponds to the $|m_s| = 1/2$ conduction ($|m_s| = 3/2$ valence) band. We have assumed that $m_0 > m_1$, so that these two bands bend oppositely. The "band pseudospin" index $\sigma \in \pm 1$, and independence of $\varepsilon_{\pm,\sigma}(\mathbf{k})$ on σ specifies the Kramers degenerate states in each band. For a given $\mathbf{k}$, one possible choice is $\sigma = \mathrm{sgn}(\mathbf{J}\cdot\mathbf{k})$ (i.e. pseudospin-momentum locking), but we will not need to fix this basis. The diagonalizing matrix $\mathcal{D}$ is given by [37]

$$\mathcal{D} = \frac{1}{\left[2\left(1+\hat{d}_5\right)\right]^{1/2}}\left[\left(1+\hat{d}_5\right)\Gamma_0 + i\sum_{a=1}^{4}\Gamma_{a5}\right]. \tag{3.52}$$

The pseudospin locking in the valence and conduction bands becomes transparent

with a specific choice of the momentum $\mathbf{k} = (0, 0, k_z)$ for which the Luttinger Hamiltonian from Eq. (3.48) readily assumes a diagonal form

$$\hat{h}_L(k_z) = \text{Diag.}\left[-\frac{k_z^2}{2m_*^-}, \frac{k_z^2}{2m_*^+}, \frac{k_z^2}{2m_*^+}, -\frac{k_z^2}{2m_*^-}\right] - \mu, \tag{3.53}$$

in the spinor basis defined in Eq. (3.47), where $m_*^{\pm} = m_0 m/|m_0 \pm m|$. Therefore, for $m_0 > m$ the first and fourth (second and third) entries yield Kramers degenerate spectra for the valence (conduction) band. Hence, the pseudospin projection on the valence (conduction) band is $|m_s| = 3/2$ $(1/2)$.

In the previous sections, also look at [38], we investigated exactly these questions in the Luttinger Hamiltonian [Eqs. (3.46) and (3.50)] with isotropic p-wave pairing, but with one crucial difference. In Ref. [38], we assumed that $m > m_0$, i.e., that both bands in Eq. (3.51) "bend together", as in the light and heavy hole bands of GaAs [37]. Assuming that both bands participate in superconductivity, the bulk winding number $\nu = 4$ in that case, and the surface Majorana fluid exhibits coexisting linear and cubic dispersing branches [14]. We showed that interactions can destabilize the clean fluid [38], inducing spontaneous time-reversal symmetry breaking and surface thermal quantum Hall order[1] [19, 9, 22, 23].

By contrast, we demonstrated that quenched surface disorder is a strong perturbation that induces critical Anderson delocalization, with multifractal surface wave functions and a power-law divergence of the disorder-averaged density of states. These results were obtained numerically via exact diagonalization, and were found to agree very well with the predictions of a certain 2D conformal field theory (CFT). The CFT is the current algebra $\text{SO}(n)_\nu$ (with $\nu = 4$), where $n \to 0$ is a replica index

[1] We note that such surface order can also arise in the presence of $p + is$ pairing in the bulk [39].

[11]. We concluded that the surface states are governed by this CFT in the presence of arbitrarily weak disorder. Moreover, in a separate work we established that the class DIII $\mathrm{SO}(n)_\nu$ theory is stable against the effects of residual quasiparticle-quasiparticle interactions [11]. The main takeaway of Ref. [38] was that disorder can *enhance* topological protection at the surface of a higher-spin TSC.

The $\mathrm{SO}(n)_\nu$ CFT can be "derived" via certain conformal embedding rules for surface states of model spin-1/2 TSCs [11]. In the case of the Luttinger semimetal (LSM) with p-wave pairing studied here and for the closely related model in [38], these rules do not obviously apply. In particular, the conformal embedding argument assumes that the clean limit is also a CFT, i.e., free relativistic fermions (in $2+0$ dimensions; in the absence of interactions, we can study the problem at a fixed single particle energy [11]). By contrast, the clean surface states of higher-spin TSCs typically have higher (e.g., cubic) dispersion [15, 14], and are not conformally invariant.

Here we consider the problem in the LSM, where electron and hole bands bend oppositely. This gives rise to a different winding number ($\nu = 3$) and different surface states, depending on the doping. In fact, we invent here a *generalized surface model* (see Sec. 3.5.3) that allows us to efficiently simulate noninteracting surface states corresponding to a bulk TSC in class DIII with arbitrary integer winding number ν. The model has ν-fold dispersion, such that the large-ν limit corresponds to a highly flattened surface band with a strongly diverging clean DoS.

On physical grounds, the most general expectation for class DIII in this case would be that disorder induces a surface thermal metal [28].

In two spatial dimensions, the thermal metal phase in class DIII is stable due to weak antilocalization. Moreover, the $\mathrm{SO}(n)_\nu$ CFT fixed point, while stable against interactions, is technically *unstable* towards flowing into the thermal metal [38]; see Fig. 3.6.

Despite this, in Ref. [38] for winding number $\nu = 4$ and here for *generic* $\nu \geq 3$, we provide strong numerical evidence that any disorder induces the quantum critical scaling associated to $\mathrm{SO}(n)_\nu$, with universal predictions for experiment that depend only on ν. These include power-law scaling for the tunneling density of states, a quantized thermal conductivity divided by temperature [13, 38], and a universal multifractal spectrum of local DoS fluctuations. These states are also robust against interactions for any ν [11].

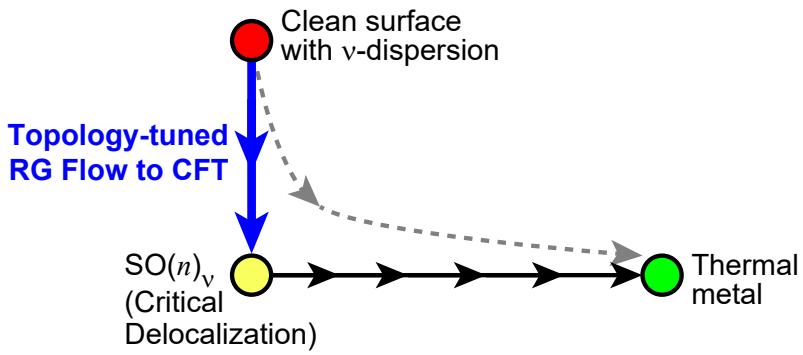

Figure 3.6: Schematic phase diagram for the noninteracting 2D surface states of a class DIII bulk topological superconductor. The fixed point representing the clean surface band structure (red dot) is unstable in the presence of time-reversal preserving quenched disorder for any $\nu \geq 3$, where ν is the integer bulk winding number. The precise form of the clean limit depends on details. For a spin-1/2 bulk, one can have ν species of massless relativistic Majorana fermions, with disorder that enters as a nonabelian gauge potential scattering between these [11]. For isotropic p-wave pairing in the LSM studied here with winding number $\nu = 3$, the surface states in the hole-doped case consist of a single two-component surface fermion with cubic dispersion, see Fig. 3.7 (a) and Eq. (3.64) [15], c.f. Refs. [14, 38]. Our generalized surface theory in Eq. (3.76) has ν-fold dispersion for the corresponding winding number. The disordered system should be described by a class DIII non-linear sigma model with a Wess-Zumino-Novikov-Witten (WZNW) term. The WZNW term prevents Anderson localization [28, 11]. This theory has a stable thermal metal phase (green dot) and an unstable, critically delocalized fixed point. The latter (yellow dot) is governed by the SO$(n)_\nu$ CFT [11, 13]. Our numerical results are generally consistent with the SO$(n)_\nu$ theory, see Figs. 3.8–3.10, implying that the renormalization group trajectory away from the clean limit is *fine-tuned by the topology* to flow into the CFT (solid vertical flow), instead of flowing into the thermal metal (dashed flow). The same conclusion was reached for a model with $\nu = 4$ in Ref. [38].

Our results suggest a deep connection between the bulk topology of three-dimensional TSC and the universal physics of the *quench-disordered* two-dimensional Majorana surface fluid, despite the fact that key attributes of the clean surface depend on details of the bulk. In particular, it suggests a *topological generalization* of the conformal embedding rule $[\mathrm{SO}(n\nu)_1 \supset \mathrm{SO}(n)_\nu \oplus \mathrm{SO}(\nu)_n]$ used to link ν clean relativistic Majorana fermions to the $\mathrm{SO}(n)_\nu$ CFT in the presence of disorder [11]. This topological generalization should apply in the replica limit $n \to 0$ to any surface band structure for any strong class DIII TSC with winding number $\nu \geq 3$, subject to time-reversal invariant quenched disorder.

Beyond fundamental interest, the Eliashberg calculations in Ref. [40] suggest that isotropic p-wave pairing gives the dominant non-s-wave channel in a hole-doped LSM due to optical-phonon–mediated pairing. For this reason we focus mainly on the hole-doped model in the following, which has $\nu = 3$ (see below).

3.5.1 Bulk and surface theory

We write the Luttinger Hamiltonian in terms of the Nambu spinor defined as,

$$H = \frac{1}{2} \int \frac{d^3\mathbf{k}}{(2\pi)^3} \, \Psi_N^\dagger(\mathbf{k}) \, \hat{h}(\mathbf{k}) \, \Psi_N(\mathbf{k}), \tag{3.54}$$

where the 8×8 Bogoliubov-de Gennes (BdG) Hamiltonian is

$$\hat{h}(\mathbf{k}) = \hat{h}_L(\mathbf{k}) \, \tau_3 + \Delta_p \, (\mathbf{J} \cdot \mathbf{k}) \, \tau_1. \tag{3.55}$$

Here $\hat{h}_L$ is the Luttinger operator from Eq. (3.50) and $\mathbf{J}$ denotes the vector of spin-3/2 generators. The Pauli matrices $\{\tau_\mu\}$ act on the particle-hole (Nambu) space.

The parameter Δ_p is the real p-wave pairing amplitude; with this choice, Eq. (3.55) is time-reversal invariant [see Eq. (3.57)]. It also satisfies the particle-hole condition in Eq. (3.56).

$$-\hat{M}_{\mathsf{P}}\,\hat{h}^{\mathsf{T}}(-\mathbf{k})\,\hat{M}_{\mathsf{P}} = \hat{h}(\mathbf{k}), \quad \hat{M}_{\mathsf{P}} = \tau_2\,\Gamma_{13}, \tag{3.56}$$

$$-\hat{M}_{\mathsf{S}}\,\hat{h}(\mathbf{k})\,\hat{M}_{\mathsf{S}} = \hat{h}(\mathbf{k}), \quad \hat{M}_{\mathsf{S}} = \tau_2. \tag{3.57}$$

We assume weak BCS pairing so that $\mu > 0$ ($\mu < 0$) describes superconductivity in the $|m_s| = 1/2$ conduction ($|m_s| = 3/2$ valence) band of the Luttinger Hamiltonian. The physical bulk quasiparticle energy spectrum of Eq. (3.55) is fully gapped,

$$E_{\pm}(\mathbf{k}) = \sqrt{\left(|\lambda_1 \pm 2\lambda_2|k^2 - |\mu|\right)^2 + \left[\left(\tfrac{2\mp 1}{2}\right)\Delta_p k\right]^2}, \tag{3.58}$$

where $2\lambda_2 > \lambda_1$ is required so that conduction and valence bands bend oppositely [or $m_0 > m$ in Eq. (3.51)], and E_+ (E_-) corresponds to superconductivity in the conduction (valence) band. The assumption of weak BCS pairing around a finite Fermi surface means that we can project the BdG Hamiltonian into the $|m_s| = 1/2$ conduction or $|m_s| = 3/2$ valence band. The results are

$$\begin{aligned}
\hat{h}_{1/2}(\mathbf{k}) &= \left[(\lambda_1 + 2\lambda_2)k^2 - \mu\right]\tau_3 + \frac{\Delta_p}{2}\begin{bmatrix} -k_z & -\frac{\bar{\mathsf{k}}^2}{\mathsf{k}} \\ -\frac{\mathsf{k}^2}{\mathsf{k}} & k_z \end{bmatrix}\tau_1, \\
\hat{h}_{3/2}(\mathbf{k}) &= \left[(\lambda_1 - 2\lambda_2)k^2 - \mu\right]\tau_3 \\
&\quad + \frac{\Delta_p}{\alpha(\mathbf{k})}\begin{bmatrix} -k_z\,\beta(\mathbf{k}) & \bar{\mathsf{k}}^3 \\ \mathsf{k}^3 & k_z\,\beta(\mathbf{k}) \end{bmatrix}\tau_1,
\end{aligned} \tag{3.59}$$

where $\mathsf{k} \equiv k_x - ik_y$, $\bar{\mathsf{k}} = \mathsf{k}^*$, and

$$\alpha(\mathbf{k}) = \frac{2}{3}\left(4k_z^2 + |\mathsf{k}|^2\right), \quad \beta(\mathbf{k}) = \left(4k_z^2 + 3|\mathsf{k}|^2\right). \tag{3.60}$$

Here we have diagonalized $(\mathbf{J}\cdot\mathbf{k})^2$ but not $(\mathbf{J}\cdot\mathbf{k})$, so that the matrix elements are rational functions of the momentum components. This is essential for obtaining a local surface theory, derived below.

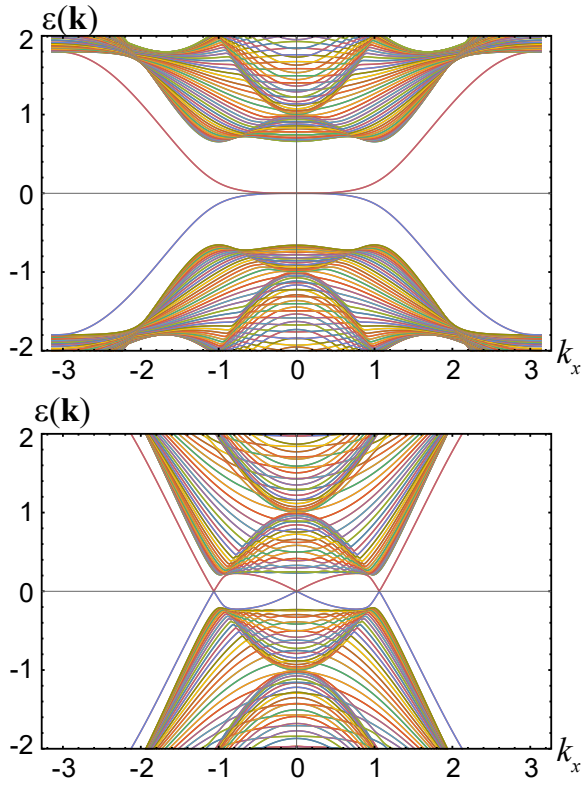

Figure 3.7: Surface Majorana fluid band structure (no unit) for the Luttinger Hamiltonian with isotropic p-wave pairing. This is a class DIII, strong topological superconductor with winding number $|\nu| = 3$ for pairing arising from either the conduction or valence bands. Results shown here are obtained from a lattice regularization and termination of Eq. (3.55). The top panel (a) shows the cubic-dispersing two-dimensional surface states obtained for hole-doping, see Eq. (3.64). The BdG parameters are $\Delta_p = 1$, $\lambda_1 = 0.1$, $\lambda_2 = 0.5$ and $\mu = -1$. The bottom panel (b) shows a relativistic cone centered at $\mathbf{k} = 0$ and a gapless ring in the electron-doped case. The parameters are the same as for (a), except that $\mu = +1$.

We employ the winding number defined by Schnyder *et al.* [9] to characterize the

topology of the bulk. After rotating $\tau_3 \to \tau_2$, one introduces the matrix 4×4 matrix $Q(\mathbf{k}) = U^{-1}(\mathbf{k})\,\Lambda\,U(\mathbf{k})$, where $U(\mathbf{k})$ diagonalizes $\hat{h}_{|m_s|}(\mathbf{k})$, and $\Lambda = \mathrm{diag}(1, 1, -1, -1)$ is the flattened matrix of energy eigenvalues. Then Q is off-diagonal,

$$Q = \begin{bmatrix} 0 & q \\ q^{-1} & 0 \end{bmatrix}, \tag{3.61}$$

and the winding number is given by

$$\nu = \int \frac{d^3k}{24\pi^2}\,\epsilon^{ijk}\,\mathrm{Tr}\left[(q^{-1}\partial_i q)(q^{-1}\partial_j q)(q^{-1}\partial_k q)\right], \tag{3.62}$$

with repeated indices summed. We find that $|\nu| = 3$ for the valence and conduction bands. From here on we ignore $\mathrm{sgn}(\nu)$, which can only be important at an interface (e.g., a physical surface) where this sign flips. Our winding number is in agreement with Ref. [15] for the $|m_s| = 3/2$ band, but differs from that obtained for the $|m_s| = 1/2$ band, in which $\nu = 1$ was claimed. We show below that surface state calculations support our results. We believe that the discrepancy comes from the fact the authors of Ref. [15] used a Fermi surface winding number method [41], which gives the correct winding number only if the system is non-degenerate.

To obtain the effective surface Hamiltonian we follow the conventional approach of terminating in the z-direction and diagonalizing $\hat{h}_{|m_s|}(\mathbf{k}, k_z \to -i\partial_z)$ where $\mathbf{k} = k_x, k_y$ denotes momentum parallel to the surface. For the $|m_s| = 3/2$ valence band, applying hard-wall boundary conditions we obtain zero energy surface states at $\mathbf{k} = 0$ of the form

$$|\psi_{0,m_s}\rangle = |\tau_2 = \mathrm{sgn}(m_s)\rangle \otimes |m_s\rangle \otimes |f_{m_s}\rangle. \tag{3.63}$$

The particle-hole spin locks along the $+\tau_2$ ($-\tau_2$) direction for positive (negative) m_s [14, 38]. In Eq. (3.63), $\langle z|f_{m_s}\rangle = f_{m_s}(z)$ denotes the bound state envelope function.

Using first-order $k \cdot p$ perturbation theory we obtain the surface effective Hamiltonian,

$$\hat{h}^{(\mathsf{S})}_{3/2}(\mathbf{k}) \propto \frac{\Delta_p}{k_F^2} \begin{bmatrix} 0 & i\bar{\mathsf{k}}^3 \\ -i\mathsf{k}^3 & 0 \end{bmatrix}. \tag{3.64}$$

Eq.(3.64) satisfies the projected version of the particle-hole symmetry in Eq. (3.56),

$$-\hat{M}^{(\mathsf{S})}_{\mathsf{P}} \left[\hat{h}^{(\mathsf{S})}_{3/2}\right]^{\mathsf{T}} (-\mathbf{k})\, \hat{M}^{(\mathsf{S})}_{\mathsf{P}} = \hat{h}^{(\mathsf{S})}_{3/2}(\mathbf{k}), \quad \hat{M}^{(\mathsf{S})}_{\mathsf{P}} = \sigma_1, \tag{3.65}$$

and the projected time-reversal symmetry [Eq. (3.57)]

$$-\hat{M}^{(\mathsf{S})}_{\mathsf{S}}\, \hat{h}^{(\mathsf{S})}_{3/2}(\mathbf{k})\, \hat{M}^{(\mathsf{S})}_{\mathsf{S}} = \hat{h}^{(\mathsf{S})}_{3/2}(\mathbf{k}), \quad \hat{M}^{(\mathsf{S})}_{\mathsf{S}} = \sigma_3. \tag{3.66}$$

Here the matrices $\{\sigma_\mu\}$ act on the components $m_s = \pm 3/2$.

Fig. 3.7 shows the clean Majorana surface bands obtained numerically from a lattice regularization of Eq. (3.55) for (a) $|m_s| = 3/2$ valence-band–hole and (b) $|m_s| = 1/2$ conduction-band–electron superconductivity. Below we focus on the hole-doped case in which the surface fluid has cubic dispersion [Eq. (3.64)]. The surface fluid in the electron-doped case is depicted in Fig. 3.7 (b), and exhibits a linear Majorana cone around $\mathbf{k} = 0$ and a zero-mode ring at finite surface momentum; the latter structure is inconsistent with $\nu = 1$ [15, 14].

3.5.2 Quenched surface disorder, class DIII SO$(n)_\nu$ conformal field theory, and numerical results

We now turn to perturbations of the surface theory, focusing on the cubic-dispersing Majorana fluid that arises from hole-doped superconductivity. We can write the surface Hamiltonian as

$$H_0^{(\mathsf{S})} = \frac{1}{2}\int d^2\mathbf{r}\, \eta^{\mathsf{T}}\, \hat{M}_{\mathsf{P}}^{(\mathsf{S})}\, \left(\sigma_-\, \partial^3 - \sigma_+\, \bar{\partial}^3\right) \eta, \tag{3.67}$$

where $\eta \to \eta_{m_s}$ is a two-component Majorana spinor and $\mathbf{r}$ is the position vector. The chiral derivative operators are $\{\partial, \bar{\partial}\} \equiv (1/2)(\partial_x \mp i\partial_y)$, while $\sigma_\pm \equiv \sigma_1 \pm i\sigma_2$. Here we have set the prefactor of Eq. (3.64) equal to one.

The simplest class of surface perturbations are constant bilinears. Such an operator can be written as $\eta^{\mathsf{T}} \hat{M}_{\mathsf{P}}^{(\mathsf{S})} \Lambda \eta$, with Λ a 2×2 Hermitian matrix. The only bilinear that satisfies particle-hole in Eq. (3.65) (i.e., which does not vanish under Pauli exclusion) is the mass term $\Lambda = \sigma_3 \simeq J^z$. This is the projection of the spin operator perpendicular to the surface. The nonzero expectation value of this term (due e.g. to a coupling with an external Zeeman field) would open a surface energy gap and signal time-reversal symmetry breaking. The time-reversal broken state would reside in a plateau of a surface thermal quantum Hall effect [19, 9, 22, 23].

These considerations are almost identical to ^{3}He-B [8, 9], which has spin-1/2 and $\nu = 1$. The only difference is that the derivatives in Eq. (3.67) appear to the first power for $\nu = 1$, whereas here we get the $\nu = 3$ power for the spin-3/2 bulk.

Residual quasiparticle-quasiparticle interactions should be short-ranged (due to

screening by the bulk superfluid). Since η is a two-component Majorana field, the most relevant interaction that we can write down is

$$H_I^{(\mathsf{S})} = u \int d^2\mathbf{r}\ \eta_1 \boldsymbol{\nabla}\eta_1 \cdot \eta_2 \boldsymbol{\nabla}\eta_2. \tag{3.68}$$

The coupling strength u has dimensions of length for cubic dispersion and is therefore irrelevant in the sense of the renormalization group (RG) [15].

Finally we turn to quenched disorder, which is always present at the surface of a real sample. We assume the disorder is non-magnetic, but may arise due to neutral adatoms, charged impurities, grain boundaries, etc. In other words, any time-reversal invariant surface potential perturbation is allowed. Since the only bilinear without derivatives is the massive, time-reversal odd J^z operator discussed above, we must broaden the search to include bilinears with derivatives. The most relevant possible potential can be encoded in the Hamiltonian

$$H_D^{(\mathsf{S})} = -\frac{i}{2} \int d^2\mathbf{r} \left[\eta^{\mathsf{T}}(\mathbf{r})\, \hat{M}_{\mathsf{P}}^{(\mathsf{S})}\, \sigma_\alpha\ \frac{\overleftrightarrow{\partial}}{\partial x^\beta}\ \eta(\mathbf{r}) \right] P_{\alpha\beta}(\mathbf{r}). \tag{3.69}$$

In this equation repeated indices are summed, $\alpha, \beta \in \{x, y\}$. We assume that $P_{\alpha\beta}(\mathbf{r})$ is a white-noise-correlated random potential with variance λ. Then λ has dimensions of $1/(\text{length})^2$ and is a relevant perturbation to the clean cubic band structure.

Similar to the previous sections, The effects of disorder cannot be treated perturbatively. The standard procedure would produce a disorder-averaged nonlinear sigma model in class DIII, which possesses a stable thermal metal phase [24, 28]. Although the thermal metal is perturbatively accessible in the sigma model with the WZNW term, the critical $\mathrm{SO}(n)_\nu$ CFT fixed point is not, except for the limit of large

ν. Therefore we resort to numerics in the remainder of this section. The question we want to answer is whether disorder flows into the $\mathrm{SO}(n)_\nu$ CFT or the thermal metal, see Fig. 3.6.

The noninteracting BdG Hamiltonian implied by Eqs. (3.67) and (3.69) has momentum space matrix elements

$$\left[\hat{h}_{\mathsf{S}}\right]_{\mathbf{k},\mathbf{k}'} = \begin{bmatrix} 0 & i\bar{\mathsf{k}}^3 \\ -i\mathsf{k}^3 & 0 \end{bmatrix} \delta_{\mathbf{k},\mathbf{k}'} + (k_x + k'_x) \begin{bmatrix} 0 & 1 \\ 1 & 0 \end{bmatrix} P_x(\mathbf{k} - \mathbf{k}') + (k_y + k'_y) \begin{bmatrix} 0 & -i \\ i & 0 \end{bmatrix} P_y(\mathbf{k} - \mathbf{k}'), \tag{3.70}$$

where we have taken $P_{\alpha\beta}(\mathbf{r})$ to be diagonal in its lower indices. Gaussian white noise disorder can be efficiently simulated in momentum space using a random phase method [12],

$$P_\alpha(\mathbf{k}) = \frac{\sqrt{\lambda}}{L} e^{i\theta_\alpha(\mathbf{k})} \exp\left(-\frac{k^2\xi^2}{4}\right), \tag{3.71}$$

where $\theta_\alpha(-\mathbf{k}) = -\theta_\alpha(\mathbf{k})$, but these are otherwise independent, uniformly distributed random phases. The parameters L, ξ and λ denote the system size, correlation length, and disorder strength respectively. For exact diagonalization, we choose periodic boundary conditions so that $\mathbf{k} = (2\pi/L)\mathbf{n}$, and the components of $\mathbf{n} \in \{\mathbb{Z}, \mathbb{Z}\}$ run over a square with $-N_k \leq n_i \leq N_k$, for $i = 1, 2$. Here N_k determines the size of the vector space in which we diagonalize, which is $2(2N_k + 1)^2$. Although the choice of L is arbitrary, we use it to fix the ultraviolet momentum cutoff $\Lambda = 2\pi N_k/L$. The correlation length ξ and the dimensionful disorder strength λ are then measured in terms of powers of Λ. The random-phase approach is equivalent to the disorder-average up to finite-size corrections [12]. We perform the calculations in momentum

space in order to avoid fermion doubling.

Similar to the case of $\nu = 4$ of previous sections and [38], to characterize the disordered surface theory, we study the scaling of the disorder-averaged DoS $\varrho_{\mathsf{S}}(\varepsilon)$ and wave function multifractality, measures that are expected to show universal behavior at the $\mathrm{SO}(n)_3$ fixed point. The clean surface has $\varrho_{\mathsf{S}}(\varepsilon) \propto |\varepsilon|^{-1/3}$ due to the cubic dispersion. For winding number ν, in the presence of time-reversal preserving disorder the $\mathrm{SO}(n)_\nu$ theory predicts the scaling behavior of the disorder-averaged DoS [42, 11] to be $\varrho_{\mathsf{S}}(\varepsilon) \propto |\varepsilon|^{-1/(2\nu-3)}$. In the case of the hole-doped LSM with $\nu = 3$, the clean and dirty CFT predictions coincide. For the generalized surface theory introduced below [defined via Eq. (3.76)] or the $\nu = 4$ model studied in Ref. [38], the clean and dirty predictions differ, so that the DoS provides a useful diagnostic. We will plot the integrated density of states (IDoS) $N(\varepsilon)$. For the $\mathrm{SO}(n)_\nu$ theory

$$N(\varepsilon) \equiv \int_0^\varepsilon d\varepsilon' \, \varrho_{\mathsf{S}}(\varepsilon') \sim |\varepsilon|^{(2\nu-4)/(2\nu-3)}. \tag{3.72}$$

For TSC surface states, the multifractal spectrum $\tau(q)$ is expected to have the form [29, 11, 12]

$$\tau(q) = \begin{cases} (q-1)(2-\theta_\nu\, q), & q < |q_c|, \\ (\sqrt{2}-\sqrt{\theta_\nu})^2 q, & q > q_c, \\ (\sqrt{2}+\sqrt{\theta_\nu})^2 q, & q < -q_c, \end{cases} \tag{3.73}$$

where

$$q_c \equiv \sqrt{2/\theta_\nu}. \tag{3.74}$$

The spectrum is quadratic below the *termination threshold* $q = \pm q_c$, beyond which it is linear [29, 28, 30].

For disordered class DIII surface states and winding number ν, the $\mathrm{SO}(n)_\nu$ theory predicts [11]

$$\theta_\nu = \frac{1}{\nu - 2}, \quad \nu \geq 3. \tag{3.75}$$

Eqs. (3.72) and (3.75) are exact results that obtain from the primary field spectrum of $\mathrm{SO}(n)_\nu$ in the replica $n \to 0$ limit. Isotropic p-wave pairing in the Luttinger semimetal gives $\nu = 3$, so that $\theta_\nu = 1$ and $q_c = \sqrt{2} \simeq 1.4$. This corresponds to quite strong multifractality, which presents some difficulties as we will see. By contrast, large ν gives $\theta_\nu \ll 1$ and $q_c \gg 1$, corresponding to weakly multifractal (nearly plane-wave) states.

Fig. 3.8 depicts our numerical results for the $\tau(q)$ spectrum for two different disorder strengths, and the IDoS $N(\varepsilon)$ for one disorder strength. As mentioned above, the IDoS is not particularly useful for $\nu = 3$ because the clean and dirty CFT predictions coincide. Moreover, the strong divergence in the corresponding DoS $\varrho(\varepsilon)$ makes it difficult to get sufficient resolution in the peak itself.

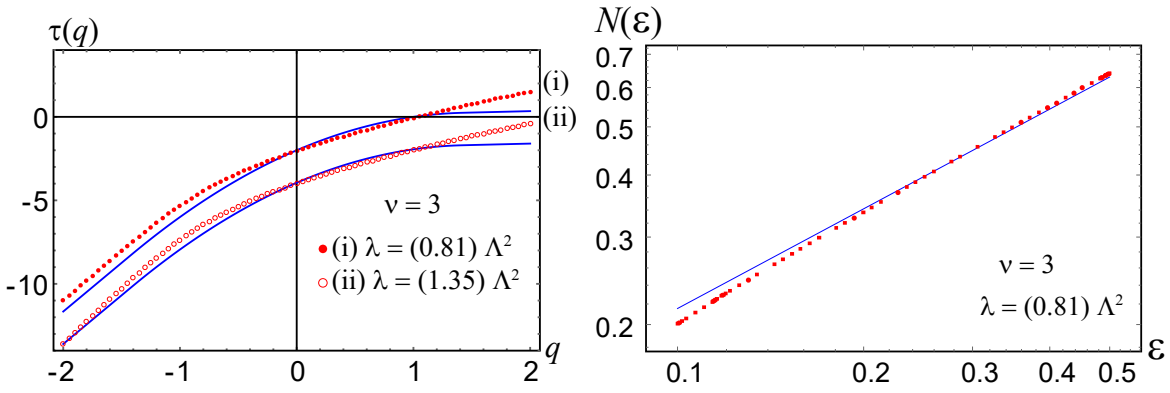

Figure 3.8: Numerical results for the surface states of the hole-doped Luttinger semimetal with isotropic p-wave pairing in the bulk and time-reversal symmetry preserving disorder on the surface. The winding number of the bulk is $\nu = 3$. The left plot shows the multifractal spectrum [Eqs. (3.73)] for two typical lowest energy surface wave functions in fixed disorder realizations. The dotted red curves are the numerical results, while the solid blue curve is the analytical prediction from the SO(n)$_3$ CFT [Eqs. (4.3)–(3.75)]. The curves marked (i) and (ii) correspond to two different disorder strengths λ; the second one is shifted vertically for clarity. Because λ has dimensions of $1/(\text{length})^2$, it is measured in units of the squared momentum cutoff Λ^2 (see text). The system size is a 109×109 grid of momenta. Box sizes b=1 and b=5 are used to extract $\tau(q)$ [see Eqs. (2.11) and (2.12)]. The right plot shows the integrated density of states $N(\varepsilon)$ (No unit). In this case, both the clean limit and the SO(n)$_3$ theory predict $N(\varepsilon) \sim \varepsilon^{2/3}$ [Eq. (3.72)]. For $\nu = 3$ the effects of disorder are strong, as indicated by the analytical result for the universal multifractal spectrum (blue curves, left panel). It is almost "frozen" [a frozen state has $\tau(q) = 0$ for $q > q_c$ [29, 43, 44, 45, 12]]. This means that the typical wave function consists of a few rare peaks with arbitrarily large separation, see Fig. 1(b) in Ref. [12] for an example. We expect that finite size effects are quite severe in this case, responsible for the deviation between the analytical prediction and numerics. See Figs. 3.9 and 3.10 for higher ν, which give much better agreement.

We find that the multifractal spectrum becomes disorder-independent for sufficiently large disorder strengths. This is important, because the thermal metal phase should exhibit weak multifractality and a weak DoS divergence, but both features would be disorder- and scale-dependent due to weak antilocalization [24]. We observe rough agreement between the analytical $\mathrm{SO}(n)_3$ CFT prediction [Eqs. (3.73)–(3.75)] and the numerics. This should be compared to the $\nu = 4$ model studied in Ref. [38], wherein quite good agreement was obtained. Even better results are found for the higher-ν model explicated in the next section, see Figs. 3.9 and 3.10.

We attribute the relatively poor fit for $\tau(q)$ in Fig. 3.8 to the *strong multifractality* predicted by $\mathrm{SO}(n)_3$. This is indicated by the solid blue curve in the top panel of Fig. 3.8. The analytical $\tau(q)$ is almost "frozen." A frozen state has $\tau(q) = 0$ for $q > q_c \geq 1$ [29]. A critically delocalized, but frozen state consists of a *few* rare probability peaks, with arbitrarily large separation between these [29, 43, 44, 45, 12]. The peaks are sufficiently rare that their heights do not scale with a power of the system size L, similar to an Anderson localized state. (The term "frozen" originates via a mapping to the classical glass transition in the random energy model [29, 44, 45].) Frozen states also resemble the "random singlet" wave functions of the Jordan-Wignerized random bond XY model in 1D, which have the quality of random telegraph signals [46]. In a previous study [12], we found that the momentum space method does not scale well for frozen states, and we believe this is the source of the relatively poor fit in Fig. 3.8.

3.5.3 Generalized surface: Higher winding numbers and numerical results

If we believe that finite size effects are responsible for the relatively poor fit between numerics and the $\mathrm{SO}(n)_3$ CFT in Fig. 3.8, the obvious way to improve is to increase the system size. Instead of doing this (which requires more computer memory), we take another approach.

We conjecture that the Majorana surface fluid of a class DIII TSC with bulk winding number $\nu \in 2\mathbb{Z}+1$ (odd) can be captured by the generalized 2×2 surface model

$$\left[\hat{h}_{\mathsf{S}}^{(\nu)}\right]_{\mathbf{k},\mathbf{k}'} = \begin{bmatrix} 0 & i\bar{\mathsf{k}}^{\nu} \\ -i\mathsf{k}^{\nu} & 0 \end{bmatrix} \delta_{\mathbf{k},\mathbf{k}'} + (k_x + k_x')\,\sigma_1\,P_x(\mathbf{k}-\mathbf{k}') + (k_y + k_y')\,\sigma_2\,P_y(\mathbf{k}-\mathbf{k}'). \tag{3.76}$$

For $\nu = 1$ we get the spin-1/2 surface states of ^{3}He-B, while $\nu = 3$ corresponds to the hole-doped LSM [Eq. (3.70)]. Again taking $P_{x,y}$ to be random phase, white noise variables as in Eq. (3.71), the disorder strength λ is relevant for any $\nu \geq 3$, while it is irrelevant for ^{3}He-B.

How do we know that the surface Hamiltonian in Eq. (3.76) can be taken to represent a TSC, without connecting it to a bulk model for general ν? Certainly the clean limit of this model is artificial and extremely unstable (to both disorder and interactions) for large ν. Both attributes follow from the strongly diverging clean

DoS,

$$\varrho(\varepsilon) \sim |\varepsilon|^{-(\nu-2)/\nu}. \tag{3.77}$$

However, if the "topological tuning" scenario articulated in Fig. 3.6 is correct, then *any* clean starting point should lead to the same disordered fixed point, the $\mathrm{SO}(n)_\nu$ CFT [11].

We can infer the bulk winding number ν by computing the *surface winding number* W_{S}. This obtains by adding the homogeneous time-reversal symmetry-breaking mass term $m\,\sigma_3$ to the clean band structure in Eq. (3.76), and computing [8]

$$W_{\mathsf{S}}(m) = \frac{\epsilon_{\alpha\beta\gamma}}{3!(2\pi)^2} \int_{-\infty}^{\infty} d\omega \int d^2\mathbf{k}\, \mathrm{Tr}\, \Big[\Big(\hat{G}^{-1}\partial_\alpha \hat{G}\Big) \times \Big(\hat{G}^{-1}\partial_\beta \hat{G}\Big) \Big(\hat{G}^{-1}\partial_\gamma \hat{G}\Big) \Big], \tag{3.78}$$

where Tr denotes the trace over the two spinor components, and $\alpha, \beta, \gamma \in \{\omega, k_x, k_y\}$ (repeated indices are summed). The surface state Green function's $\hat{G}(\omega, \mathbf{k}, m)$ is given by

$$\hat{G}(\omega, \mathbf{k}, m) \equiv \Big[-i\,\omega\,\hat{1} + \hat{h}_m(\mathbf{k})\Big]^{-1}, \tag{3.79}$$

where $\hat{h}_m = \hat{h}^{(\nu)}_{\mathsf{S}}|_{P_\alpha=0} + m\,\sigma_3$ is the clean, gapped surface Hamiltonian. The surface winding number determines the thermal Hall conductivity [18, 19, 20, 21, 22, 23]

$$\kappa_{xy} = W_{\mathsf{S}}\,\kappa_\circ, \tag{3.80}$$

$$\kappa_\circ = \pi^2 k_B^2 T/6h. \tag{3.81}$$

Here h is Planck's constant.

It is easy to check that

$$W_{\mathsf{S}}(m) = (\nu/2)\ \mathrm{sgn}(m). \tag{3.82}$$

For $\nu = 1$ this is the standard "half-integer" (shifted) surface quantum Hall effect familiar from ^{3}He-B and topological insulators [8, 9]. For a relativistic Majorana surface fluid, it can be shown that the maximum possible value of W_{S} is the bulk winding number divided by two [11]. We conclude that the surface Hamiltonian in Eq. (3.76) is a representative surface band structure for a class DIII TSC with winding number ν.

Following the same logic of the previous section, we compare the numerical diagonalization of Eq. (3.76) in momentum space to the predictions of the $\mathrm{SO}(n)_\nu$ CFT. Results for $\nu = 5$ and $\nu = 7$ are shown in Figs. 3.9 and 3.10, respectively. In these cases, the multifractal spectrum $\tau(q)$ and the IDoS $N(\varepsilon)$ match very well the corresponding CFT predictions in Eqs. (3.73)-(3.75) and (3.72), respectively. The reason for the better matching is the weaker multifractality of the critical wave functions with increasing ν, as predicted by the CFT.

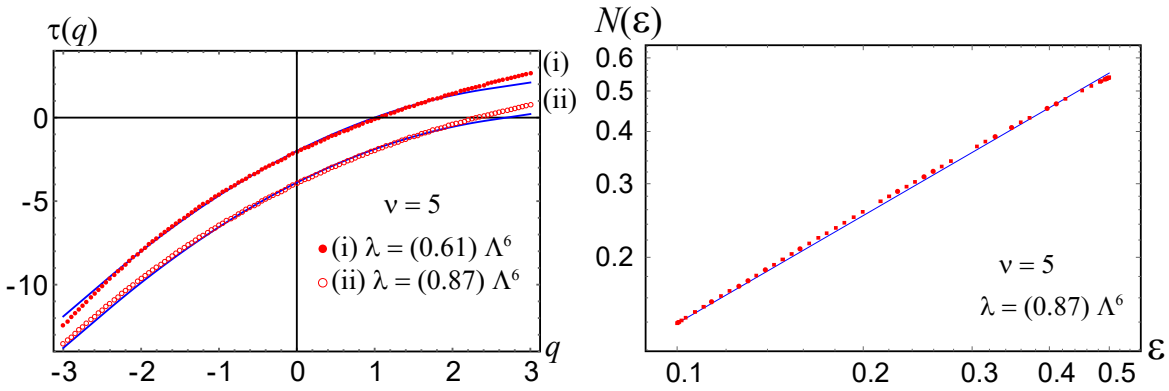

Figure 3.9: Same as Fig. 3.8, but for the generalized surface model in Eq. (3.76) with $\nu = 5$. Numerical results are shown as red dotted curves, while analytical predictions (blue solid curves) for $\tau(q)$ and $N(\varepsilon)$ obtain from the SO$(n)_5$ CFT. Box sizes b=3 and b=6 are used to extract $\tau(q)$. The disorder strength λ formally has units of 1/(length)^6, hence proportional to the sixth power of the momentum cutoff Λ. The absolute disorder strength is of the same order as in Fig. 3.8, with the same system size. The termination threshold $q_c = \sqrt{6} \simeq 2.45$ [see Eq. (3.74)].

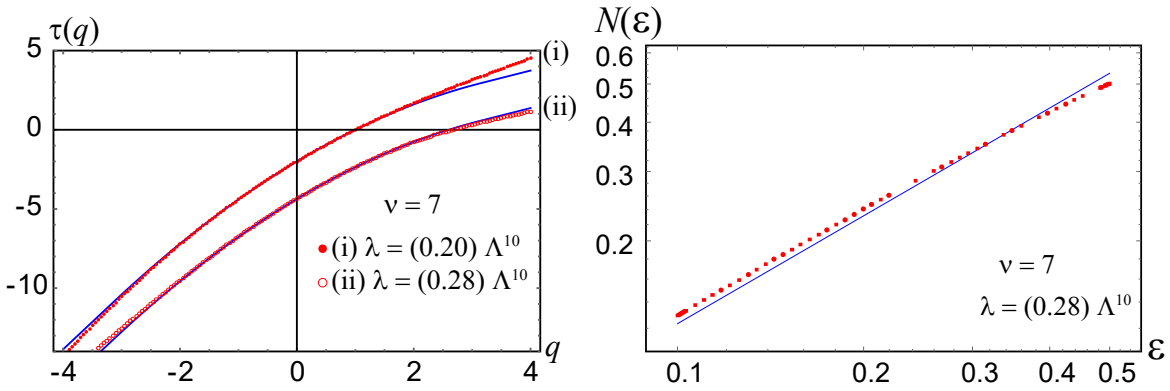

Figure 3.10: Same as Fig. 3.8, but for the generalized surface model in Eq. (3.76) with $\nu = 7$. Numerical results are shown as red dotted curves, while analytical predictions (blue solid curves) for $\tau(q)$ and $N(\varepsilon)$ obtain from the $\mathrm{SO}(n)_7$ CFT. Box sizes b=3 and b=6 are used to extract $\tau(q)$. The disorder strength λ formally has units of $1/(\text{length})^{10}$, hence proportional to the tenth power of the momentum cutoff Λ. The absolute disorder strength is of the same order as in Fig. 3.8, with the same system size. The termination threshold $q_c = \sqrt{10} \simeq 3.16$ [see Eq. (3.74)].

The $\mathrm{SO}(n)_\nu$ fixed point is stable against residual quasiparticle-quasiparticle interactions [11]. In addition to universal energy scaling of the DoS and wave function multifractality (both which could be detected via STM), the ratio of the thermal conductivity to temperature T is predicted to be quantized in the $T \to 0$ limit: [9, 13]

$$\lim_{T\to 0} \frac{\kappa_{xx}}{T} = \frac{|\nu|}{\pi} \frac{\kappa_\circ}{T}, \tag{3.83}$$

where $\kappa_\circ$ was defined by Eq. (3.81).

3.6 Summary

In summary, we have studied the topological superconductivity in Luttinger model for two different orientations of bands.

For the case where both bands bend in same direction we have derived surface states and surface effective Hamiltonian for a spin-3/2 time-reversal invariant topological superconductor that hosts a cubic dispersion coexisting with the conventional linear Majorana cone. We have shown that in the clean limit, unlike the spin-1/2 case [33], interactions are marginally relevant and lead to a BCS-type instability that gaps out the surface and induces a thermal quantum Hall effect (TQHE) plateau. By contrast, quenched disorder gives the $\mathrm{SO}(n)_4$ theory previously predicted for a spin-1/2 TSC with winding number 4; this theory is stable to interaction effects. We conclude that disorder enhances topological protection. In the low-temperature limit, the ratio of the longitudinal thermal conductivity to temperature is predicted to be quantized and proportional to the bulk winding number, as shown in Eq. (3.83).

On the other hand, when bands bend oppositely, we have investigated the effects of disorder on the cubically dispersing surface states that arise from odd-parity, fully gapped p-wave pairing (as in ^{3}He-B). Using a generalized surface model with ν-fold dispersion for winding number $\nu \geq 3$, we demonstrated excellent agreement between numerical results and the conformal field theory (CFT) $\mathrm{SO}(n)_\nu$ for higher ν. The CFT characterizes the critical delocalization of the surface in the presence of disorder, whilst the naively expected thermal metal phase is absent in our numerics. This suggests a deep connection between the bulk topology on one hand, and the *disordered* surface physics on the other, reminiscent of key aspects of the integer quantum

Hall effect. A key open question is whether there exists a *topological generalization* of the conformal embedding rule $[\mathrm{SO}(n\nu)_1 \supset \mathrm{SO}(n)_\nu \oplus \mathrm{SO}(\nu)_n]$, employed to explain the robustness of CFT results in the case of spin-1/2 topological superconductors [11].

Chapter 4

Percolation all the way down on the surface of topological supercondutors

This chapter is mainly adapted from the following published paper: S.A.A. Ghorashi, Y. Liao, M.S. Foster, arXiv:1711.03972.

4.1 Introduction

When fluid floods a landscape, the percolation threshold is the stage at which travel by land or by sea becomes equally difficult. Percolation ideas can be applied to the quantum Hall effect, wherein the sea level corresponds to the Fermi energy and

the landscape is the electrostatic impurity potential [47]. The critical wave function that sits exactly at the plateau transition corresponds to the percolation threshold, while closed contours that encircle isolated lakes or islands correspond to Anderson localized states within a plateau. Although the critical statistics of the usual plateau transition differ [48, 28], the plateau transition in the *spin quantum Hall effect* (SQHE) [49, 50, 51, 52, 53, 54, 55, 56] can be mapped exactly to classical percolation [50]. The SQHE was introduced in the context of spin singlet, two-dimensional (2D) superconductivity. The idea is that unpaired gapless quasiparticles can conduct a spin current, and under the right conditions (broken time-reversal symmetry but negligible Zeeman coupling, as in a $d+id$ superconductor [51]), the spin Hall conductance within the spin Hall plateau is precisely quantized. The SQHE belongs to the Altland-Zirnbauer class C [28].

For both classical percolation and the plateau transition in the SQHE, the "sea level" has to be fine-tuned to the percolation threshold; in the SQHE, this means that almost all states are Anderson localized, except those at the transition. In this chapter, we uncover a new realization of 2D critical percolation that requires no fine-tuning. In particular, we provide numerical evidence for an *energy band* of states, where each state exhibits statistics consistent with critical percolation. We show that this band of percolative states appears at the surface of a three-dimensional (3D) topological superconductor in class CI, subject to quenched surface disorder that preserves spin SU(2) symmetry and time-reversal invariance.

Our results are important because they suggest an unexpected, direct link between 3D time-reversal invariant topological superconductors (TSCs) and 2D quantum Hall effects. We employ a generalized class CI surface model that works for any bulk winding number, but we find the same "percolative" states at finite energy in all cases. Together with previous results for a particular winding number in class AIII [57, 58, 12], it is natural to conjecture that the three classes of 3D TSCs (CI, AIII, DIII [9, 59]) possess surface states that at finite energy and (almost) *any winding number* are equivalent to the corresponding plateau transitions of the SQHE (class C), integer quantum Hall effect (class A), and thermal quantum Hall effect (class D). The band of plateau transition states found here will dominate finite-temperature surface state response (a "multifractal spin metal").

Surface states of bulk TSCs are known to exhibit unusual properties in the presence of quenched disorder [9, 10, 11, 38, 26]. Effective field theories for TSC surface states were studied two decades ago [57, 60, 61, 62, 63] as examples of exactly solvable, critical delocalization in 2D. Only recently was it understood that these must be attached to a higher-dimensional bulk, owing to certain anomalies [9, 22, 23]. TSC surface states can appear as multiple species of 2D Dirac or Majorana fermions [9]. In class CI these are Dirac, not Majorana, owing to the conservation of spin SU(2), the z-component of which plays the role of a U(1) "electric" charge. Nonmagnetic intervalley impurity scattering takes the form of an SU(2) vector potential, due to the anomalous version of time-reversal symmetry [10, 11]. The exact solvability (and proof of critical delocalization) holds at only one single-particle energy in these theories [60, 61, 62, 63].

The conventional notion of topological protection is that at least one surface or edge state in the bulk gap of a topological insulator or superconductor must evade Anderson localization in the presence of (non-magnetic) quenched disorder [9]; this was made precise in [64], building off of [8, 65]. For a class CI TSC surface, the zero-energy wave function is critically delocalized, with statistics that are exactly solved by a certain conformal field theory (CFT) [66, 10]. The standard symmetry-based argument [28, 64] would imply that all finite-energy states of a class CI Hamiltonian should reside in the "orthogonal" metal class (AI), which is known to possess only Anderson-localized states in 2D [28]. Let us examine the grounds for this belief.

A superficial argument can be given for why any nonstandard class (such as CI) with a special chiral or particle-hole symmetry becomes a standard Wigner-Dyson class (here AI) at finite energy: Adding the energy perturbation to the Hamiltonian matrix $\hat{h} \to \hat{h} - \varepsilon\,\hat{1}$ breaks the special symmetry for any $\varepsilon \neq 0$. This logic is flawed, however, because ε couples to the identity operator $\hat{1}$, which *commutes* with $\hat{h}$. The argument works for a random symmetry-breaking perturbation $\varepsilon \to \varepsilon(\mathbf{r})$ ($\mathbf{r}$ is the position vector), but that is a different problem.

A physical argument for the reduction to Wigner-Dyson is the following. Non-standard class models can be realized as Bogoliubov-de Gennes Hamiltonians for quasiparticles in superconductors [9, 28]. For single-particle energies much larger than the BCS gap, it is clear that the wave functions should resemble those of the parent normal metal, while $\varepsilon = 0$ is the only symmetry-distinguished energy. However, TSC surface states can evade this argument as well, since the bulk gap is the *maximum* allowed surface state energy; above this, 2D surface states can hybridize

with the 3D bulk. All TSC surface states are (Andreev) bound states.

We find energy stacks of delocalized class C, SQHE plateau transition states for any bulk TSC winding number. The SQHE states are identified by their multifractal spectrum [54, 55, 28]. The absence of Anderson localization throughout the *surface* energy spectrum is qualitatively similar to 1D edge states of quantum Hall, as well as edge and surface states of 2D and 3D topological insulators. Our work suggests that this may be a general principle of fermionic topological matter.

Our results generalize a previous observation for a simpler model in class AIII. This model consists of a single 2D Dirac fermion coupled to abelian vector potential disorder; it is critically delocalized and exactly solvable at zero energy [57]. It can also be interpreted as the surface state of TSC with winding number $\nu = 1$ [9, 11]. It was later claimed [58] that all finite-energy states of this model should reside at the plateau transition of the (class A) integer quantum Hall effect, and this was verified numerically [12]. The same logic employed by Haldane [67] and Pruisken [68] implies that there should be an "even-odd" effect whereby AIII surface states for a TSC with even winding number are localized at finite energy, while those with odd form stacks of critical plateau-transition states [58]. Here we find critical delocalization for all class CI winding numbers, with no "even-odd" effect.

4.2 Model and numerical approach

We employ a *k-generalized* two-species Dirac model to capture the surface states of a class CI TSC with even winding number $\nu = 2k$,

$$\hat{h}_{\mathsf{s}} = \begin{bmatrix} 0 & (-i\partial)^k + \mathsf{A}^a\,\hat{\tau}^a + \mathsf{A}^0 \\ (-i\bar{\partial})^k + \bar{\mathsf{A}}^a\,\hat{\tau}^a + \bar{\mathsf{A}}^0 & 0 \end{bmatrix}, \tag{4.1}$$

where $\partial \equiv \partial_x - i\partial_y$ and $\mathsf{A} \equiv A_x - iA_y$, with $\bar{\partial}$ and $\bar{\mathsf{A}}$ respective complex conjugates of these.

For $k = 1$, this is the surface theory for the lattice model in [66]. Quenched disorder enters via the abelian vector potential $\mathsf{A}^0(\mathbf{r})$ or the nonabelian SU(2) vector potential $\mathsf{A}^a(\mathbf{r})\,\hat{\tau}^a$, where $\mathbf{r} = \{x, y\}$ is the position vector, and $\hat{\tau}^{1,2,3}$ denotes Pauli matrices acting on the space of the two species. The case with $k > 1$ was inspired by higher-dispersion surface bands obtained in spin-3/2 class DIII TSC models [15, 14, 38, 26]. The bulk winding number can be inferred by turning on the time-reversal symmetry-breaking mass term and calculating the surface Chern number [8, 38]. For $k > 1$, Eq. (4.1) is not gauge invariant, but this is of no consequence because the vector potentials merely represent the most relevant type of quenched disorder allowed by symmetry. Class CI has $P^2 = -1$ particle-hole symmetry [9]. In order to realize P, we take $\mathsf{A}^0 = 0$ for odd k, while we take $\mathsf{A}^3 = 0$ for even k 4.4. Time-reversal invariance is equivalent to the block off-diagonal form of $\hat{h}_{\mathsf{s}}$ [10, 11].

We analyze $\hat{h}_{\mathsf{s}}$ in Eq. (4.1) numerically via exact diagonalization. Calculations are performed in momentum space $\mathbf{q} = \{q_x, q_y\}$ to avoid fermion doubling of the continuum surface theory [12, 38, 26]. The Fourier components of any nonzero vector

potential $A^{0,1,2,3}_{x,y}(\mathbf{q})$ are parameterized via (same method of disorder as chapter 3)

$$A(\mathbf{q}) = \left(\sqrt{\lambda}/L\right) \exp\left[i\theta(\mathbf{q}) - q^2\xi^2/4\right], \tag{4.2}$$

where $\theta(\mathbf{q}) = -\theta(-\mathbf{q})$, but these are otherwise independent, uniformly distributed random phases. Here L, ξ and λ denote the system length, correlation length, and disorder strength respectively; the latter is dimensionless for $k = 1$. We choose periodic boundary conditions so that $q_i = (2\pi/L)n_i$, with $-N \leq n_i \leq N$, for $i \in \{x, y\}$. Here N determines the size of the vector space, which is $4(2N + 1)^2$. The inverse correlation length ξ^{-1} is measured in units of the ultraviolet momentum cutoff $\Lambda = 2\pi N/L$. This approach is equivalent to the disorder-averaging, up to finite-size corrections [12]. The drawback is that our matrices are dense, which limits our system sizes.

We reconstruct each real space eigenstate $\psi(\mathbf{r})$ and examine $|\psi|^2(\mathbf{r})$ to look for Anderson localization. Except for the states in the high-energy "Lifshitz tails" (see the numerical density of states plots in Fig. 4.2), we find no evidence of localization, although we cannot rule it out for much larger system sizes. Localization at high energies is not unexpected, because the model is not terminated in a physical way (which would instead involve hybridizing the 2D surface with the 3D bulk).

All of the states that we find in the bulk of the surface energy spectrum look "critically delocalized," i.e., $|\psi|^2(\mathbf{r})$ is small over most of the surface, but is sporadically punctuated by probability peaks of variable height. The main quantative tool we use to characterize these states is multifractal analysis [48, 54, 55, 28, 57, 61, 62, 10, 11, 12, 38, 26]. One breaks the system up into boxes of size b, and defines the

box probability μ_n and inverse participation ratio (IPR) $\mathcal{P}_q$ via $\mu_n = \int_{\mathcal{A}_n} d^2\mathbf{r}\,|\psi(\mathbf{r})|^2$, $\mathcal{P}_q \equiv \sum_n \mu_n^q$, where $\mathcal{A}_n$ denotes the nth box. The multifractal spectrum $\tau(q)$ governs the scaling of the IPR, $\mathcal{P}_q \sim (b/L)^{\tau(q)}$.

For critically delocalized states, the form of $\tau(q)$ is expected to be self-averaging in the infinite system size limit [29]. For class CI surface states at zero energy (class C SQHE plateau transition states), the spectrum is exactly (to a good approximation) parabolic, and is given by

$$\tau(q) = \begin{cases} (q-1)(2-\theta\, q), & q < |q_c|, \\ \left(\sqrt{2} - \mathrm{sgn}(q)\sqrt{\theta}\right)^2 q, & |q| > q_c, \end{cases} \tag{4.3}$$

where $q_c \equiv \sqrt{2/\theta}$. The parameter θ determines the degree of critical rarification: $\theta = 0$ ($\theta > 0$) for a plane wave (multifractal) state. In the above, q_c denotes the *termination threshold* [29, 30]; the spectrum is linear for $|q| > q_c$, and the slopes govern the scaling of the peaks and valleys of $|\psi|^2(\mathbf{r})$ for $q > q_c$ and $q < -q_c$, respectively. Note that an accurate calculation of $\tau(q)$ for negative q requires significant coarse-graining, since it entails taking negative powers of a function that is small almost everywhere. For this reason negative-q results are always worse than positive q (and are often not reported).

For class CI, the $\mathrm{Sp}(2n)_k$ CFT predicts that $\theta_k = 1/2(k+1)$ [10]. Analytical and numerical results on the SQH plateau transition instead give $\theta \simeq 1/8$ [54, 55].

4.3 Numerical Results

In Fig. 4.1, we plot the anomalous (non-plane-wave) part of the multifractal spectrum $\Delta(q) \equiv \tau(q) - 2(q-1)$ for $k = 1$ (a,b), $k = 7$ (c,d), and $k = 8$ (e,f). The class CI and class C (percolation) analytical predictions are respectively depicted as blue dot-dashed and green dashed lines.

In Fig. 4.1(a,c,e), we plot the numerical result for the low-energy states of the spectrum, which show good agreement with the k-dependent class CI prediction. Calculations are performed for a typical realization of the random phase disorder, without disorder-averaging, over an 81×81 grid of momenta ($N = 40$). The solid red line in each panel is obtained by averaging over a narrow energy bin of 36 consecutive low-energy states. For $k = 7, 8$ these correspond to the lowest positive energies in the spectrum, while for $k = 1$ we neglect states very close to zero energy, keeping those in the energy bin (0.01-0.0141) (see Fig. 4.2 for the numerical density of states versus energy). The average plus or minus the standard deviation is indicated by the light red shaded region in each panel. We plot the deviation only for $|q| < q_c$, where q_c is the termination threshold for the low-energy class CI prediction (a,c,e) or finite-energy SQHE class C prediction (b,d,f,g). Since the spectrum becomes linear outside of this range, the error in a given $\Delta(q)$ for a particular wave function also grows linearly for $|q| > q_c$, but only the slope discrepancy near $q = \pm q_c$ is meaningful.

Figs. 4.1(b,d,f) show the corresponding results for finite-energy states. Again the solid red curve in each panel corresponds to an average over a narrow energy bin of 36 states, with good agreement for $k = 1$ (b) $k = 7$ (d) and $k = 8$ (f) with the

k-independent, class C prediction (dashed green curve). The finite-energy bin for each k is selected as the one with the highest percentage of states matching the spin quantum Hall prediction, as indicated by a certain fitness criterion described below.

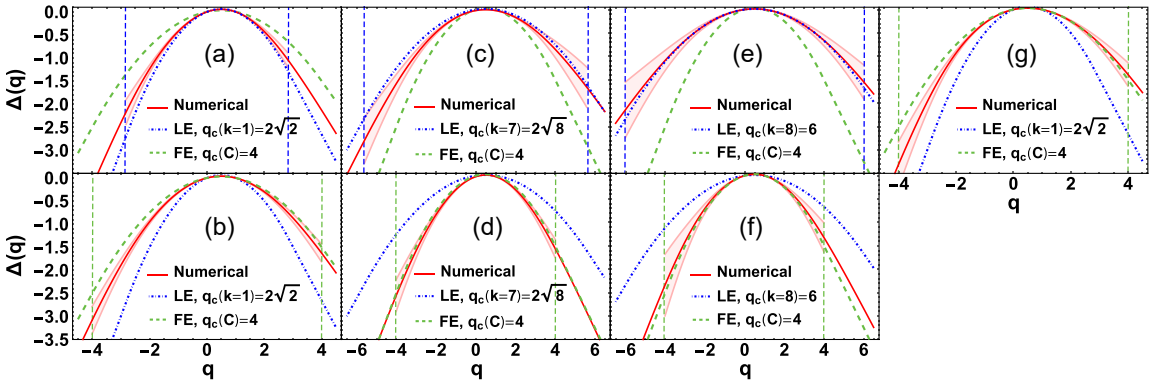

Figure 4.1: Anomalous part of the multifractal spectrum $\Delta(q) \equiv \tau(q) - 2(q-1)$ for low-energy (a,c,e) and finite-energy (b,d,f) states, for the class CI TSC surface state model in Eq. (4.1) with $k = 1$ (a,b), $k = 7$ (c,d), and $k = 8$ (e,f). The solid red curves obtain from momentum-space exact diagonalization [12]. The blue dot-dashed curve (green dashed curve) is the k-dependent (independent) class CI (class C SQH plateau transition) prediction. The solid red curve in each panel is obtained by averaging over states within a narrow energy bin (see text); the shaded red region shows the standard deviation amongst the states within the bin. Finally, (g) shows the same for low-energy states when time-reversal symmetry is broken explicitly, while spin SU(2) (particle-hole) symmetry is preserved. The system is a $(2N+1) \times (2N+1)$ grid of momenta; here $N = 40$. The disorder strength $\lambda = 1.6\pi$ (16π) for $k = 1$ $(7, 8)$. Parameters for (g) and box sizes are specified in 4.6.

Finally, Fig. 4.1(g) shows the low-energy spectrum of the $k = 1$ model, but

now with time-reversal symmetry broken explicitly. This is obtained by turning on random mass and nonabelian potential terms with vanishing average value, but nonzero variance [49] and 4.5. These perturbations preserve spin SU(2) symmetry. A nonzero average mass corresponds to a "spin Hall Chern insulator"; tuning this to zero while retaining a nonzero variance was expected to give the SQHE plateau transition [66, 22]. Indeed Fig. 4.1(g) matches the states in Figs. 4.1(b,d,f).

In Fig. 4.2, we compare the computed $\tau(q)$ spectrum for every state in regularly spaced energy bins to the class CI and C predictions, for $k = \{1, 7, 8\}$. We introduce a "fitness" criteria, defined as follows. For each eigenstate $\psi(\mathbf{r})$, we compute the error between the numerical spectrum $[\equiv \tau_N(q)]$ and the appropriate analytical prediction $[\equiv \tau_A(q)]$, $\text{error}(q) \equiv |\tau_N(q) - \tau_A(q)|/\tau_A(q)$. If the error is less than or equal to 6% for 75% of the evaluated q-points in the interval $0 \leq q \leq q_c$, we keep the state. We consider bins of 36 states each; the states within each bin have consecutive eigenenergies. The height of each bar marked "$\mathsf{E}_{\mathsf{WZNW}}$" ("$\mathsf{E}_{\mathsf{P}}$") denotes the percentage of eigenstates in the bin starting with energy E that match the class CI (class C) prediction. The energies in each left panel of Fig. 4.2 should be compared to the numerical density of states shown in the corresponding right panel.

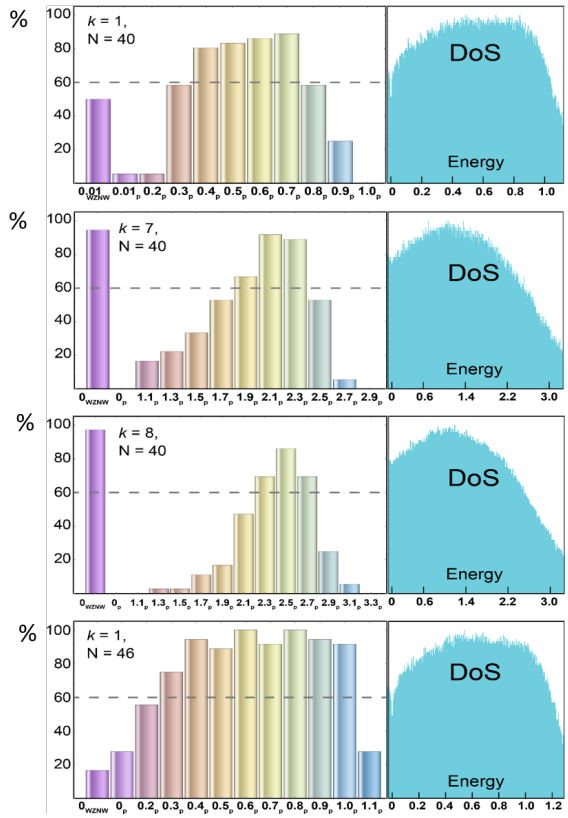

Figure 4.2: Population statistics for critically delocalized eigenstates. The bars in each graph give the percentage of states with consecutive energy eigenvalues lying within a narrow energy bin that match a certain fitness criterion. The bar labeled "$\mathsf{E}_{\mathsf{WZNW}}$" ("$\mathsf{E}_{\mathsf{P}}$") denotes the percentage of eigenstates in the bin beginning with energy E that match the class CI (class C) prediction for the multifractal spectum (see text for details). The bar energy labels should be compared to the corresponding density of states (DoS). All plots are for $N = 40$ except the bottom, which has $N = 46$. In the latter case even the lowest energy bin has more class C than class CI states.

Fig. 4.2 indicates that most of the lowest energy states match the predictions of class CI (bin $\mathsf{E}_{\mathsf{WZNW}}$), except for $k = 1$. In this case, the lower percentage is due to the strong disorder strength that we chose, $\lambda = 1.6\pi$ [c.f. Ref. [12]]. By contrast, for $k = 1$ the finite energy states match well the class C SQH prediction (bins E_{P} with $\mathsf{E} \in \{0.4, \ldots, 0.7\}$ for $N = 40$). With stronger disorder, we convert more of the spectrum to class C for a fixed system size N. The plots for $k = 7$ and 8 also show bands of finite energy states that match class C, but possessing narrower bandwidths. Here we choose $\lambda = 16\pi$, but we stress that the effective dimensionless disorder strength grows *weaker* for larger k [26].

The energy-averaged finite-energy results for $\tau(q)$ shown in Fig. 4.1(b,d,f) were obtained from the bin with the highest percentage of states matching the class C SQH prediction for each value of k. I.e., for $k = 7$, the red solid curve in Fig. 4.1(d) was obtained by averaging over states in the bin starting with energy $\mathsf{E} = 2.1$. We emphasize that while the fitness criterion introduced above is arbitrary, the trends are not 4.8.

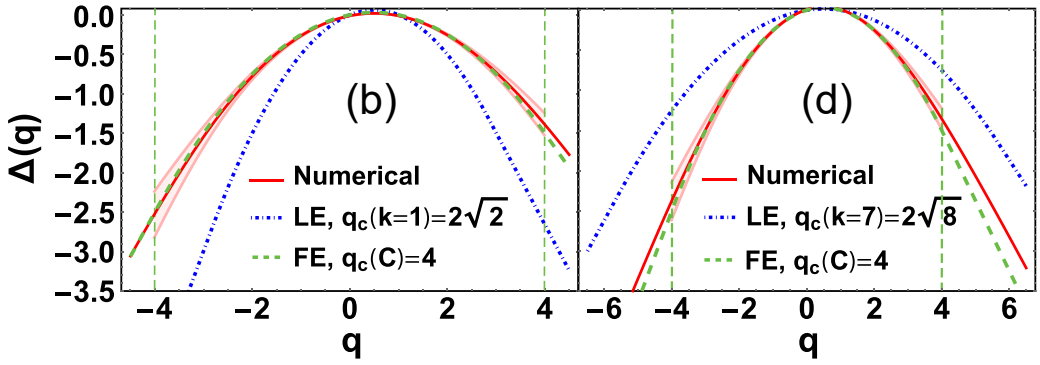

Figure 4.3: Same as Figs. 1(b) and 1(d), but for $N = 46$.

Results for a larger system ($N = 46$) appear at the bottom of Fig. 4.2 and in Fig. 4.3. We show finite-size trends in Fig. 4.4. Here we plot $\Delta(q)$ for $q = 2, 3$, which are well-distinguished for the class CI (low-energy) and class C (finite-energy) analytical predictions [10, 55]. Although we are limited to relatively small sizes due to dense matrices and full diagonalization, the trends for increasing N suggest convergence towards the analytical results 4.8.

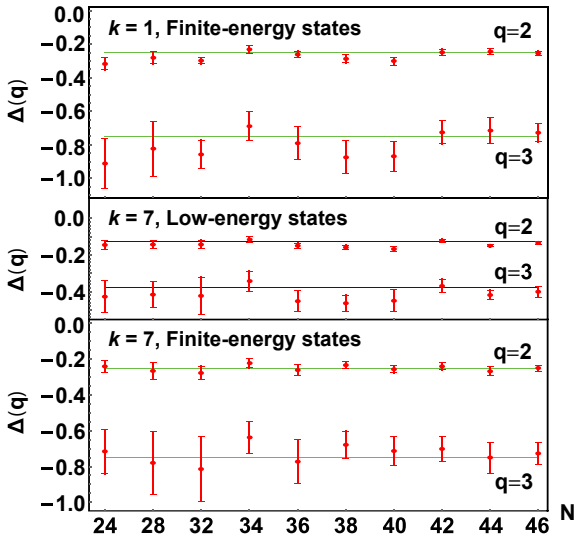

Figure 4.4: Finite-energy and low-energy $\Delta(q)$ as in Figs. 4.1 and 4.3, but for fixed $q = 2, 3$ and for varying system sizes N. The intrinsic disorder correlation length and strength are kept fixed 4.6. The blue and green lines are the exact analytical predictions for $\Delta(2, 3)$ [10, 55]. The solid points show the average, while error bars indicate the standard deviation within the energy bin. The main effect of increasing N is to reduce the fluctuations, although the reduction is slower for q closer to the termination threshold q_c (= 4 for class C). Full $\Delta(q)$ and population statistics (as in Fig. 4.2) are presented in 4.8.

4.4 Particle-hole symmetry for odd and even k

The Hamiltonian $\hat{h}_{\mathsf{s}}$ can be succinctly encoded by introducing an additional species of Pauli matrices $\hat{\sigma}^{1,2,3}$ as a basis for the decomposition in Eq. (4.1). Then

$$\hat{h}_{\mathsf{s}} = \frac{1}{2}\left[\hat{\sigma}^{+}\left(-i\partial\right)^{k} + \hat{\sigma}^{-}\left(-i\bar{\partial}\right)^{k}\right] + \hat{\boldsymbol{\sigma}}\cdot\mathbf{A}^{a}(\mathbf{r})\,\hat{\tau}^{a} + \hat{\boldsymbol{\sigma}}\cdot\mathbf{A}^{0}(\mathbf{r}), \tag{4.4}$$

where $\hat{\sigma}^{\pm} \equiv \hat{\sigma}^{1} \pm i\hat{\sigma}^{2}$ and $\hat{\boldsymbol{\sigma}}\cdot\mathbf{A} = \hat{\sigma}^{1}A_{x} + \hat{\sigma}^{2}A_{y}$. Physical time-reversal invariance is encoded in the chiral condition [9, 10, 11]

$$-\hat{M}_{\mathsf{S}}\,\hat{h}_{\mathsf{s}}\,\hat{M}_{\mathsf{S}} = \hat{h}_{\mathsf{s}}, \qquad \hat{M}_{\mathsf{S}} = \hat{\sigma}^{3}. \tag{4.5}$$

For class CI, particle-hole symmetry P must involve an antisymmetric matrix $\hat{M}_{\mathsf{P}} = -\hat{M}_{\mathsf{P}}^{\mathsf{T}}$ ("$P^{2} = -1$") [9]. The particle-hole condition is

$$-\hat{M}_{\mathsf{P}}\,\hat{h}_{\mathsf{s}}^{\mathsf{T}}\,\hat{M}_{\mathsf{P}} = \hat{h}_{\mathsf{s}}, \tag{4.6}$$

where T denotes the transpose operation and it is understood that derivative operators are odd under transposition: $(\partial_{x,y})^{\mathsf{T}} = -\partial_{x,y}$.

For $k \in \{1, 3, 5, \dots\}$ (odd), we take [10, 11]

$$\hat{M}_{\mathsf{P}}^{(\mathsf{odd})} = \hat{\sigma}^{1}\hat{\tau}^{2}. \tag{4.7}$$

Eq. (4.4) is invariant under Eq. (4.6) with this choice provided we set the abelian vector potential equal to zero, $\mathbf{A}^{0} = 0$. For $k \in \{2, 4, 6, \dots\}$ (even), we take

$$\hat{M}_{\mathsf{P}}^{(\mathsf{even})} = \hat{\sigma}^{2}\hat{\tau}^{1}. \tag{4.8}$$

Eq. (4.4) is invariant under Eq. (4.6) with this choice provided we set the third component of the SU(2) vector potential equal to zero, $\mathbf{A}^{3} = 0$.

4.5 Class C model with broken TRI

In Fig. 4.1(g), we exhibit the low-energy anomalous multifractal spectrum $\Delta(q) = \tau(q) - 2(q-1)$ for the $k = 1$ class CI model in Eq. (4.4), except that we have now explicitly broken time-reversal symmetry (in every fixed realization of disorder, but not on average). The Hamiltonian in this case resides in class C [49],

$$\hat{h}_{\rm C} \equiv \hat{h}_{\rm s} + m(\mathbf{r})\,\hat{\sigma}^3 + v^a(\mathbf{r})\,\hat{\tau}^a, \tag{4.9}$$

where $a \in \{1,2,3\}$. The mass $m(\mathbf{r})$ and nonabelian valley potentials $v^{1,2,3}(\mathbf{r})$ break physical time-reversal symmetry [Eq. (4.5)], but preserve $P^2 = -1$ particle-hole [Eqs. (4.6) and (4.7) for $k = 1$]. The latter is tantamount to spin SU(2) invariance.

4.6 Parameter specification for the numerics

The numerical results presented in Figs. 4.1-4.4 were obtained via the exact diagonalization of $\hat{h}_{\rm s}$ in Eq. (4.1). Calculations are performed in momentum space. All disorder potentials are parameterized as described in the text, i.e.

$$A_i^\mu(\mathbf{q}) = \frac{\sqrt{\lambda}}{L} \exp\left[i\,\theta_i^\mu(\mathbf{q}) - \frac{q^2\xi^2}{4}\right], \tag{4.10}$$

where $i \in \{x,y\}$ and $\mu \in \{0,1,2,3\}$. The phases $\theta_i^\mu(\mathbf{q}) = -\theta_i^\mu(-\mathbf{q})$, but are otherwise identical, independent random variables uniformly distributed over $[0, 2\pi)$. We assign the same disorder strength λ to all nonzero components of the abelian A^0 and nonabelian $\mathsf{A}^{1,2,3}$ vector potentials. We choose $\lambda = 1.6\pi$ (16π) for the $k = 1$ $(k = 7, 8)$ calculations with $N = 40$ [except Fig. 4.1(g), described below].

The arbitrary dimensionful system length L determines the ultraviolet cutoff $\Lambda = 2\pi N/L$. The correlation length of the impurity potentials is chosen to be $\xi = 0.25(L/N)$ [12]. For $N \neq 40 \equiv N_0$ (Figs. 4.2-4.4), we rescale the disorder parameter $\lambda \to (N/N_0)^{2(k-1)}\lambda$, which corresponds to fixing the intrinsic disorder strength relative to the appropriate power of the momentum cutoff.

The multifractal spectra exhibited in Fig. 4.1(a,b,g), (c,d), and (e,f) are extracted using box sizes $b = 2$ and $b = 8$ ($k = 1$), $b = 3$ and $b = 10$ ($k = 7$), and $b = 5$ and $b = 10$ ($k = 8$), respectively. Box sizes for Fig. 4.3(b,d) are $b = 2$ and $b = 13$ ($k = 1$) and $b = 2$ and $b = 31$ ($k = 7$).

For the low-energy states in class C with $k = 1$ [Fig. 4.1(g)], in addition to the nonabelian vector potentials $A^{1,2,3}_{x,y}$, we include random mass $m(\mathbf{r})$ and (valley-graded) scalar potential $v^3(\mathbf{r})$ disorders, see Eq. (4.9). The disorder strengths are $\lambda_A = \lambda_{v^3} = 0.8\pi$, while the mass variance is $\lambda_m = 16\pi$. We neglect the off-diagonal potentials $v^{1,2}(\mathbf{r}) = 0$ [Eq. (4.9)].

4.7 Sigma models for class CI TSC surface states and the class C SQHE

The nonlinear sigma model representations for (a) the class CI conformal field theory describing zero-energy TSC surface state wave functions and (b) the class C spin

quantum Hall effect are captured by the following actions [69, 11, 70],

$$S_{\rm CI} = \frac{k}{8\pi}\int d^2\mathbf{r}\,\mathrm{Tr}\left[\boldsymbol{\nabla}\hat{q}^\dagger\cdot\boldsymbol{\nabla}\hat{q}\right] + i\,\frac{\omega}{2}\int d^2\mathbf{r}\,\mathrm{Tr}\left[\hat{\Lambda}\left(\hat{q}+\hat{q}^\dagger\right)\right] - i\frac{k}{12\pi}\int d^2\mathbf{r}\,dR\,\epsilon^{abc}\,\mathrm{Tr}\left[\left(\hat{q}^\dagger\partial_a\hat{q}\right)\left(\hat{q}^\dagger\partial_b\hat{q}\right)\left(\hat{q}^\dagger\partial_c\hat{q}\right)\right], \tag{4.11a}$$

$$S_{\rm C} = \frac{\sigma_{11}}{8}\int d^2\mathbf{r}\,\mathrm{Tr}\left[\boldsymbol{\nabla}\hat{q}\cdot\boldsymbol{\nabla}\hat{q}\right] + i\,\omega\int d^2\mathbf{r}\,\mathrm{Tr}\left[\hat{\Lambda}\,\hat{q}\right] - \frac{\sigma_{12}}{8}\int d^2\mathbf{r}\,\epsilon^{ij}\,\mathrm{Tr}\left[\hat{q}\,\partial_i\,\hat{q}\,\partial_j\,\hat{q}\right]. \tag{4.11b}$$

In Eq. (4.11a), $\hat{q}(\mathbf{r})$ is a $4n\times 4n$ unitary matrix field that is also a Sp($4n$) group element; $\mathbf{r}=\{x,y\}$ is the position vector that spans over the 2D TSC surface. We assume that disorder-averaging has been accomplished with the replica trick; $n\to 0$ counts the number of replicas [35]. Here and in Eq. (4.11b), ω is a real parameter that denotes the ac frequency of the spin conductivity that the sigma model is designed to compute [70, 35]. The matrix $\hat{\Lambda}$ is diagonal and equal to $\hat{\Lambda}=\mathrm{diag}(1,1,\ldots,1,-1,-1,\ldots,-1)$ [$2n$ (+1)s and $2n$ (-1)s]. The last term in Eq. (4.11a) is the Wess-Zumino-Novikov-Witten (WZNW) term. This term is defined over a three-dimensional ball (coordinates $\{\mathbf{r},R\}$, $0\le R\le 1$), such that $\hat{q}(\mathbf{r},R=1)=\hat{q}(\mathbf{r})$ is the field on the 2D surface, while $\hat{q}(\mathbf{r},R)$ for $R<1$ is a smooth deformation of this into the ball interior. The WZNW term ensures that the action in Eq. (4.11a) is conformally invariant for $\omega=0$ [11, 71]. In the context of a 3D topological superconductor, the ball can be identified with the bulk if the surface has genus zero [72].

The structure of the first two terms of the class C sigma model can be obtained from the corresponding ones in class CI by imposing the additional constraint on

$\hat{q}(\mathbf{r})$ by hand,

$$\hat{q}^\dagger(\mathbf{r}) = \hat{q}(\mathbf{r}). \tag{4.12}$$

The matrix $\hat{q}(\mathbf{r})$ now belongs to the space $\mathrm{Sp}(4n)/\mathrm{U}(2n)$ [69, 28]. The last term in Eq. (4.11b) is the Pruisken or theta term, which assigns winding numbers to different topological sectors of the $\hat{q}$-field and evaluates to a pure imaginary phase [35]. The coefficients of the first and third terms in Eq. (4.11b) are respectively proportional to the longitudinal conductivity σ_{11} and Hall conductivity σ_{12}; the class CI WZNW model has $\sigma_{11} = k/\pi$ and $\sigma_{12} = 0$ (in units of the spin conductance quantum) [9, 11].

When the constraint in Eq. (4.12) is imposed on $\hat{q}(\mathbf{r})$ in Eq. (4.11a), we can show that the WZNW term in the latter becomes the theta term in Eq. (4.11b), with

$$\sigma_{12} = k/2. \tag{4.13}$$

However, we stress that in the context of the finite-energy TSC surface states discussed in this paper, there is no reason to trust this assignment of σ_{12}, because it does not follow from a physical RG flow. As emphasized at the end of the main text, the only statement we can make is that the energy perturbation (the operator coupling to $\omega \neq 0$) is relevant, and breaks the symmetry of the class CI model from $G \times G$ down to G, where $G = \mathrm{Sp}(4n)$ [73].

If $\omega \neq 0$ induces a flow to the class C SQHE plateau transition, it is must be due to the effect of the WZNW term on the RG. Without the WZNW term, the class CI model describes (gapless) quasiparticles in an ordinary (non-topological) spin-singlet superconductor, and the single-particle wave functions must become those of the

orthogonal metal class AI at large energies. Moreover, in this case all states (at zero and finite energy) are localized in 2D for arbitrarily weak disorder [69, 28].

4.7.1 From WZNW to theta

The derivation of Eq. (4.13) requires a little care, since the restriction in Eq. (4.12) induces topologically distinct sectors of the $\hat{q}$-matrix; this is why the theta term in Eq. (4.11b) can produce an effect. It means that the field $\hat{q}(\mathbf{r}, R)$ appearing in the WZNW term of Eq. (4.11a) cannot be strictly restricted in this way, because otherwise it is not possible to deform generic $\hat{q}(\mathbf{r}, R < 1)$ in the interior to some particular $\hat{q}(\mathbf{r}, R = 1)$ at the surface. Here we show how the WZNW term in Eq. (4.11a) becomes the theta term in Eq. (4.11b), employing the method used in Ref. [74].

We extend $\hat{q}(\mathbf{r})$ on the 2D surface to $\hat{q}(\mathbf{r}, R)$ on the three-dimensional ball through the following equation:

$$\hat{q}(\mathbf{r}, R) = \quad -i \cos\left(\tfrac{\pi R}{2}\right) \hat{1} + \sin\left(\tfrac{\pi R}{2}\right) \hat{q}(\mathbf{r}), \qquad 0 \leq R \leq 1. \tag{4.14}$$

In this extension scheme, we have $\hat{q}(\mathbf{r}, R = 0) = -i\hat{1}$ (where $\hat{1}$ is the identity) and $\hat{q}(\mathbf{r}, R = 1) = \hat{q}(\mathbf{r})$. Note that, unlike $\hat{q}(\mathbf{r})$ on the surface, $\hat{q}(\mathbf{r}, R)$ does not obey the restriction in Eq. (4.12).

Inserting Eq. (4.14) into the WZNW term of Eq. (4.11a), the latter reduces to

$$\begin{aligned} & -\tfrac{k}{8} \int d^2\mathbf{r}\, dR\, \epsilon^{abc} \operatorname{Tr}\left[\hat{q}(\mathbf{r}) \partial_b \hat{q}(\mathbf{r}) \partial_c \hat{q}(\mathbf{r})\right] \sin^2\left(\tfrac{\pi R}{2}\right) \partial_a R \\ = \quad & -\tfrac{k}{8} \int d^2\mathbf{r}\, dR\, \epsilon^{abc} \operatorname{Tr}\left\{\partial_a \left[\hat{q}(\mathbf{r}) \partial_b \hat{q}(\mathbf{r}) \partial_c \hat{q}(\mathbf{r}) \left(\tfrac{R}{2} - \tfrac{1}{2\pi} \sin(\pi R)\right)\right]\right\} \\ = \quad & -\tfrac{k}{16} \int d^2\mathbf{r}\, \epsilon^{ij} \operatorname{Tr}\left[\hat{q}(\mathbf{r}) \partial_i \hat{q}(\mathbf{r}) \partial_j \hat{q}(\mathbf{r})\right], \end{aligned} \tag{4.15}$$

where in the second equality we have used the divergence theorem and the fact that $R = 1$ on the 2D surface. Comparing this expression with the theta term in Eq. (4.11b), one obtains Eq. (4.13).

4.8 Additional numerical results

4.8.1 Density of states

The numerical density of states (DoS) is depicted via the histograms in the right panels of Fig. 4.2 for $k \in \{1, 7, 8\}$. The DoS shows a "dip" upon approaching zero energy $\mathsf{E} = 0$. This is expected for the critically delocalized class CI surface states, where the $\mathrm{Sp}(2n)_k$ conformal field theory predicts universal scaling for the DoS $\nu(\mathsf{E})$ [42, 10]

$$\nu(\mathsf{E}) \sim |\mathsf{E}|^{1/(4k+3)}, \tag{4.16}$$

a result that is independent of the multifractal spectrum [10, 11]. In Fig. 4.5, we compare the numerical integrated density of states $\mathcal{N}(\mathsf{E}) \equiv \int^{\mathsf{E}} \nu(\mathsf{E}')\, d\mathsf{E}'$ to the class CI prediction, and observe good agreement for $k = \{1, 7, 8\}$ ($N = 40$).

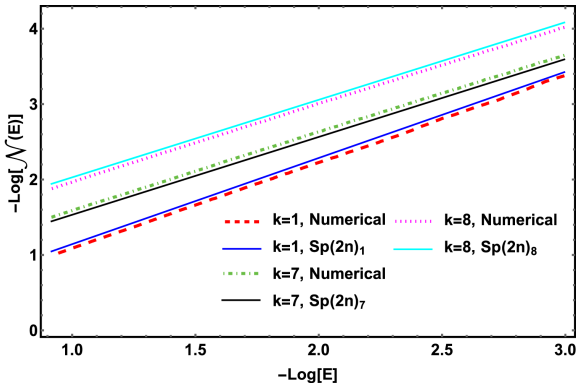

Figure 4.5: Log-log plot of the integrated density of states $\mathcal{N}(\mathsf{E})$ obtained via exact diagonalization of $\hat{h}_{\mathrm{s}}$ in Eq. (4.1), versus the exact analytical prediction of the class CI conformal field theory [42, 10]. Results are shown for $k = \{1, 7, 8\}$, with parameters chosen the same as in Figs. 1 and 2 ($N = 40$).

4.8.2 Alternative fitness threshold

To obtain the population statistics exhibited in Fig. 4.2, we employ an arbitrary "fitness" criteria, described in the main text. While the exact percentages of states above the fitness threshold (encoded in the bar heights in Fig. 2) depend somewhat sensitively on these criteria, the overall trends as a function of energy E do not. In Fig. 4.2, we replot the same data as in $k = 7$ panel of Fig. 4.2, but for the criterion that a state is kept if it matches the appropriate analytical prediction for $\tau(q)$ with no more than 7% error, over 75% or more of the q-values in the range $0 \leq q \leq q_c$.

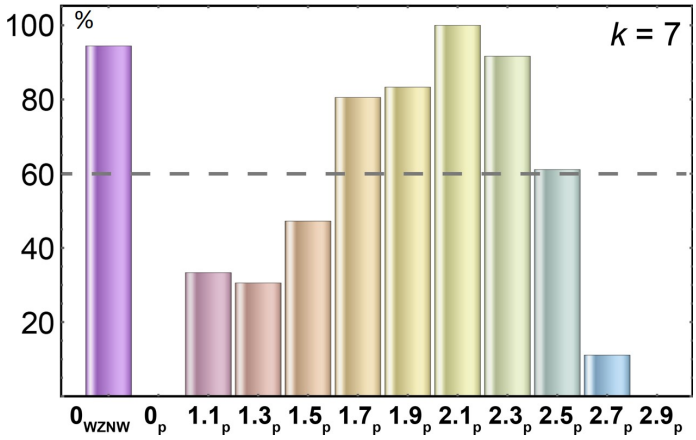

Figure 4.6: The same as the second left-hand panel of Fig. 4.2 ($k = 7$), but with a 7% error threshold for states matching the class CI ("WZNW") or C ("P") prediction for the multifractal spectrum $\tau(q)$, over the range $0 \leq q \leq q_c$.

4.8.3 Finite-size trends for $k = 1$ and $k = 7$

Here we plot the anomalous spectrum $\Delta(q) = \tau(q) - 2(q-1)$ for low- and finite-energy states as in Figs. 4.1 and 4.3, as well as the population statistics and numerical density of states as in Fig. 4.2, for the full range of N used to obtain the results shown in Fig. 4.4. Box sizes for multifractal analysis are chosen to be almost commensurate with the linear system size $2N + 1$.

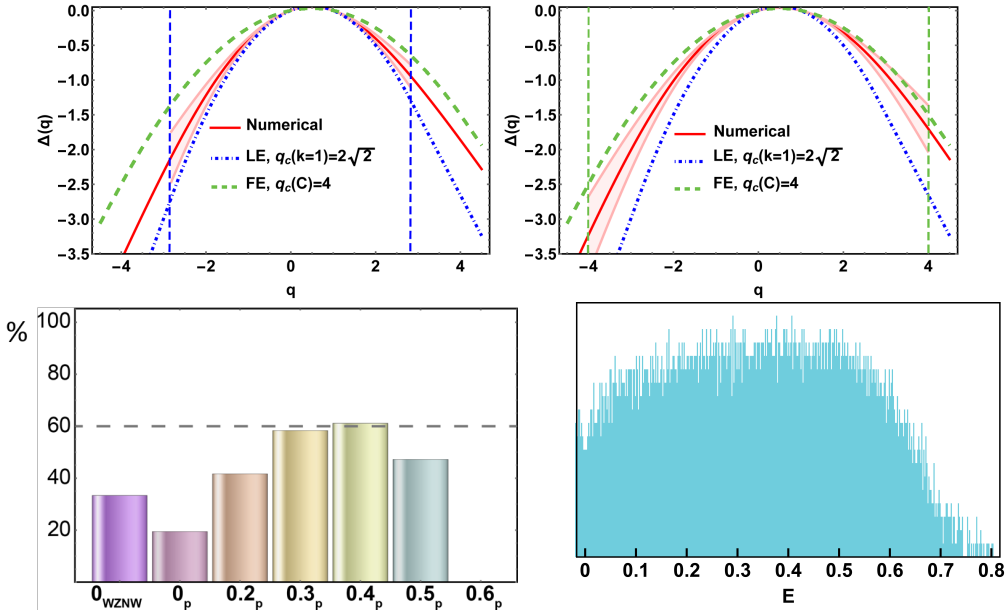

Figure 4.7: $k = 1$, $N = 24$. Box sizes $b = 2, 6$.

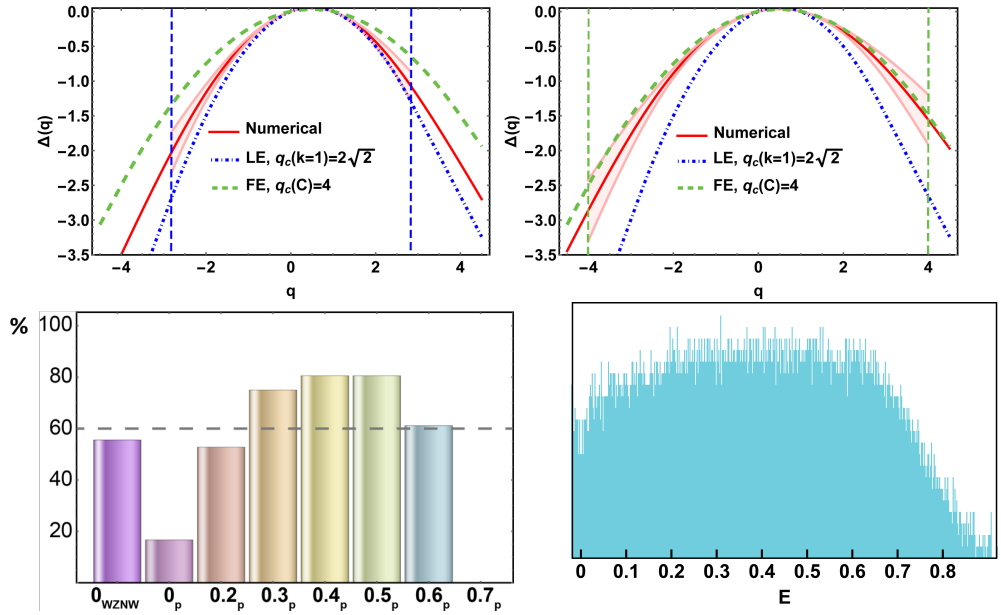

Figure 4.8: $k = 1$, $N = 28$. Box sizes $b = 2, 8$.

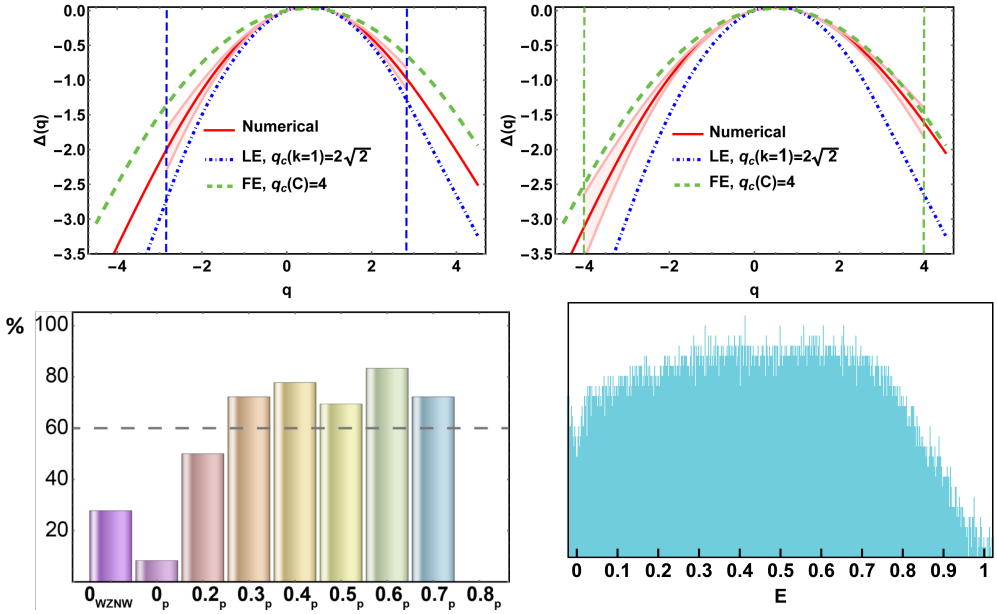

Figure 4.9: $k = 1$, $N = 32$. Box sizes $b = 2, 8$.

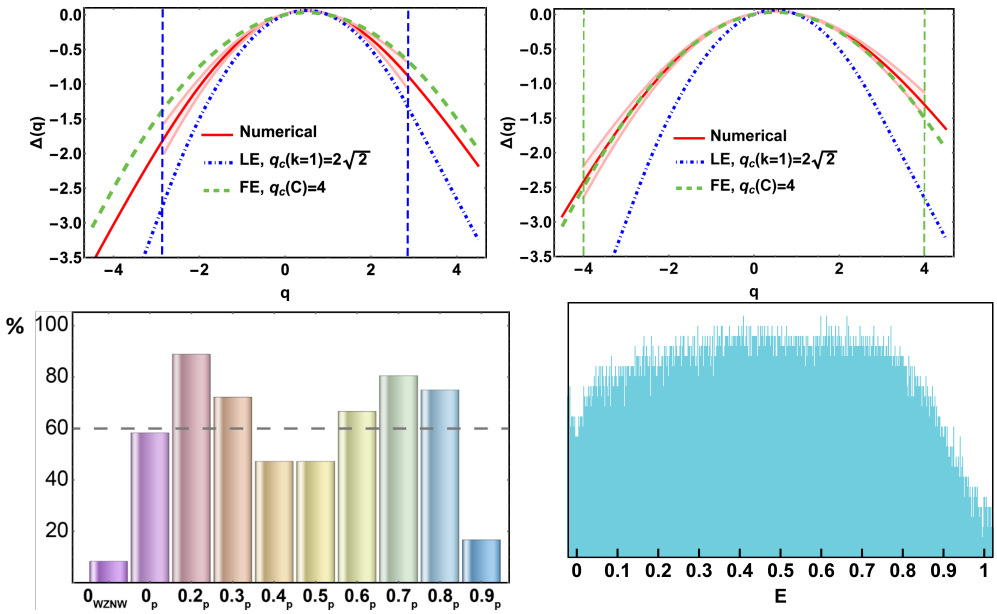

Figure 4.10: $k = 1$, $N = 34$. Box sizes $b = 2, 23$.

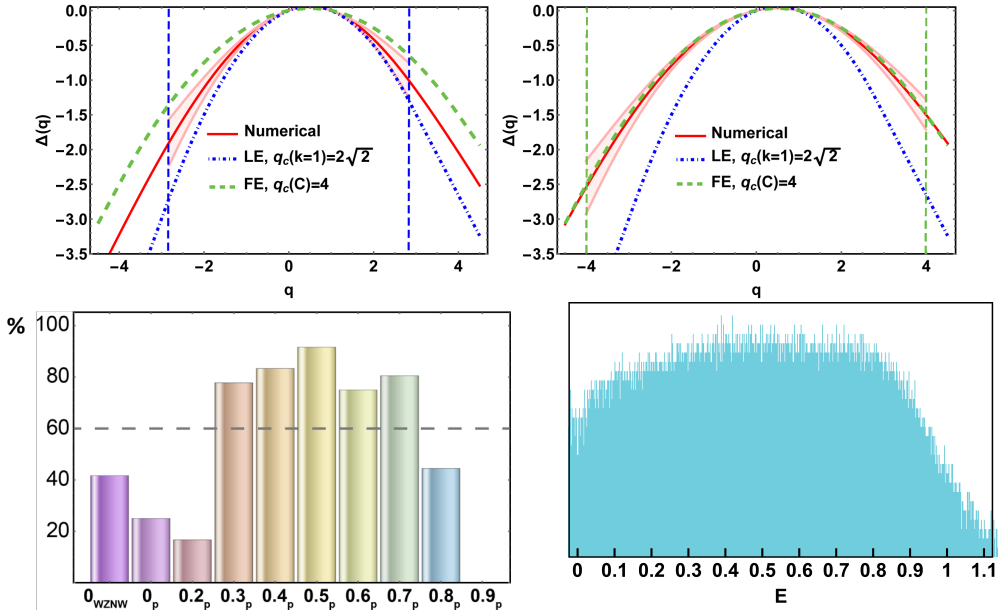

Figure 4.11: $k = 1$, $N = 36$. Box sizes $b = 3, 6$.

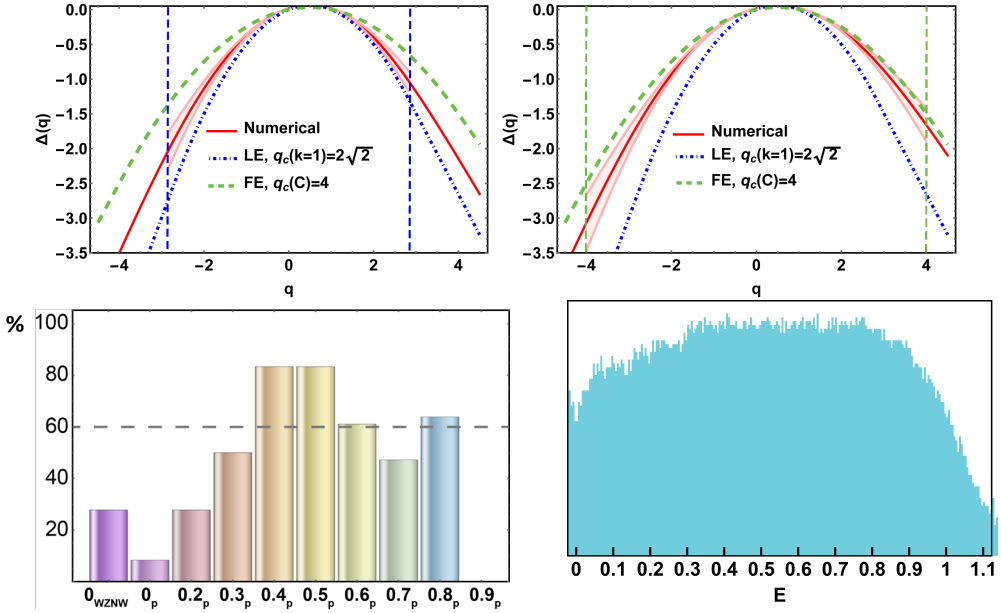

Figure 4.12: $k = 1$, $N = 38$. Box sizes $b = 2, 7$.

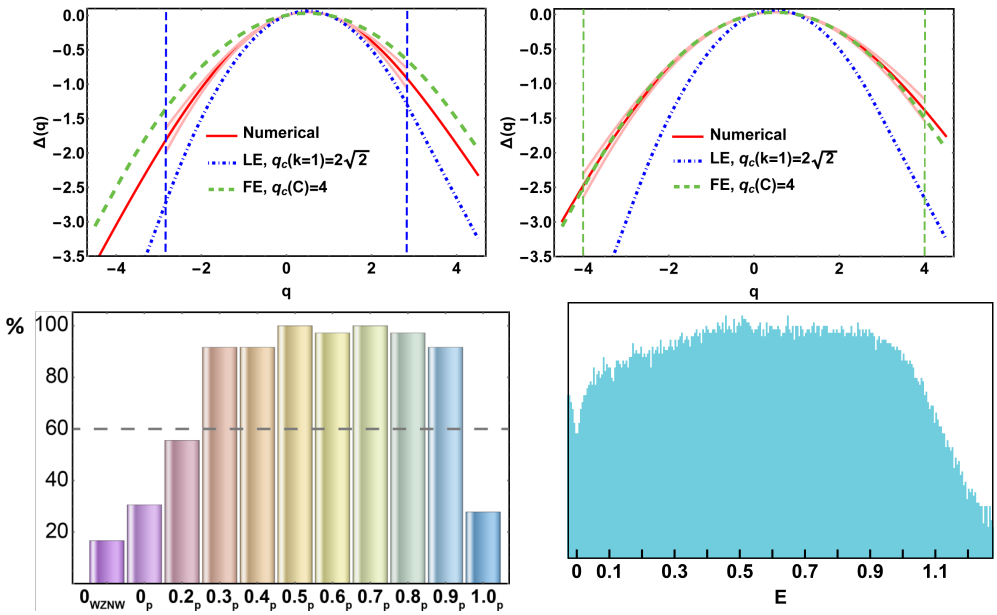

Figure 4.13: $k = 1$, $N = 42$. Box sizes $b = 2, 14$.

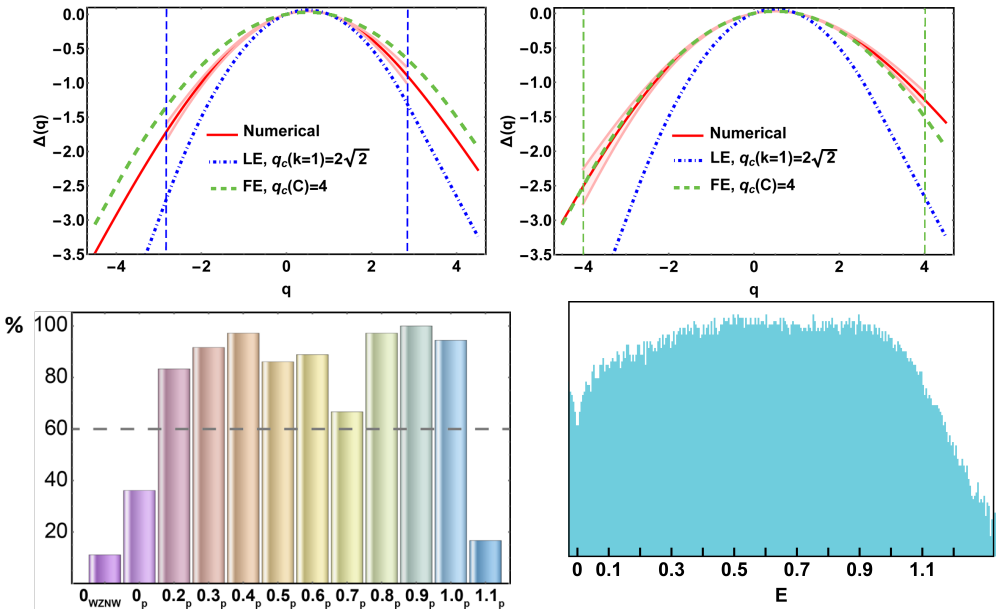

Figure 4.14: $k = 1$, $N = 44$. Box sizes $b = 2, 22$.

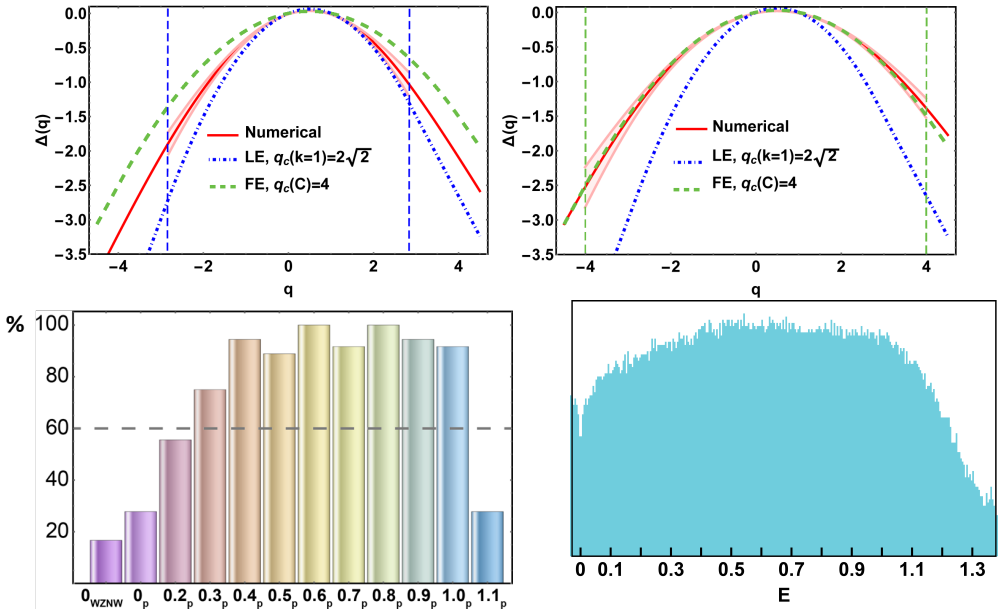

Figure 4.15: $k = 1$, $N = 46$. Box sizes $b = 2, 13$.

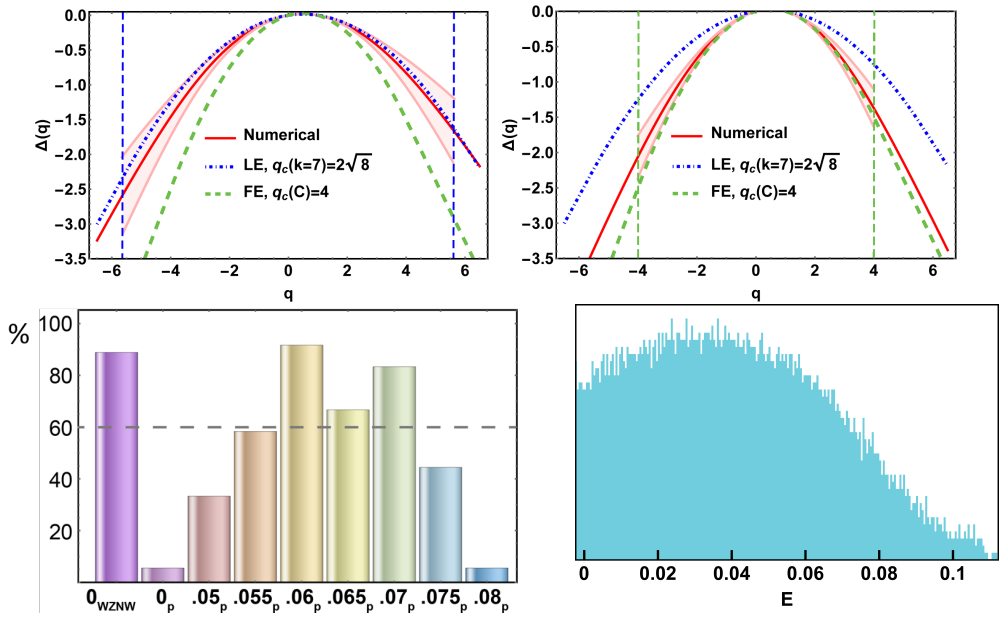

Figure 4.16: $k = 7$, $N = 24$. Box sizes $b = 3, 12$.

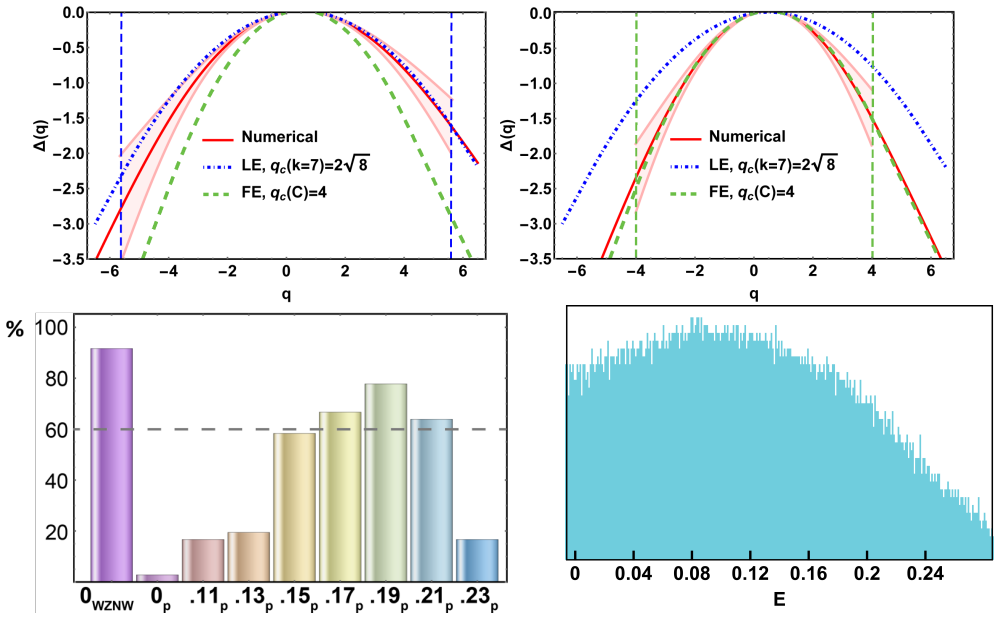

Figure 4.17: $k = 7$, $N = 28$. Box sizes $b = 4, 8$.

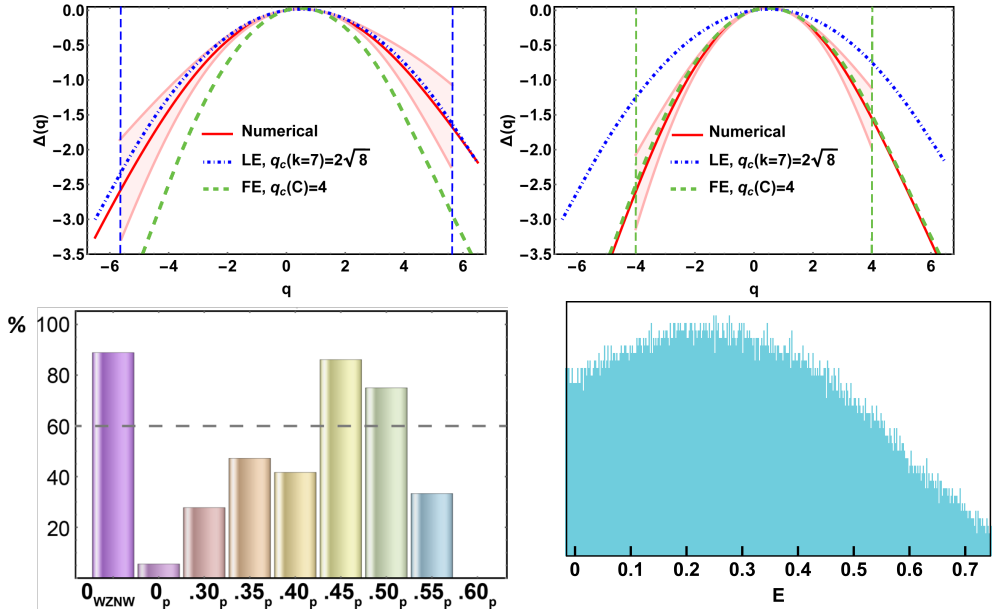

Figure 4.18: $k = 7$, $N = 32$. Box sizes $b = 4, 8$.

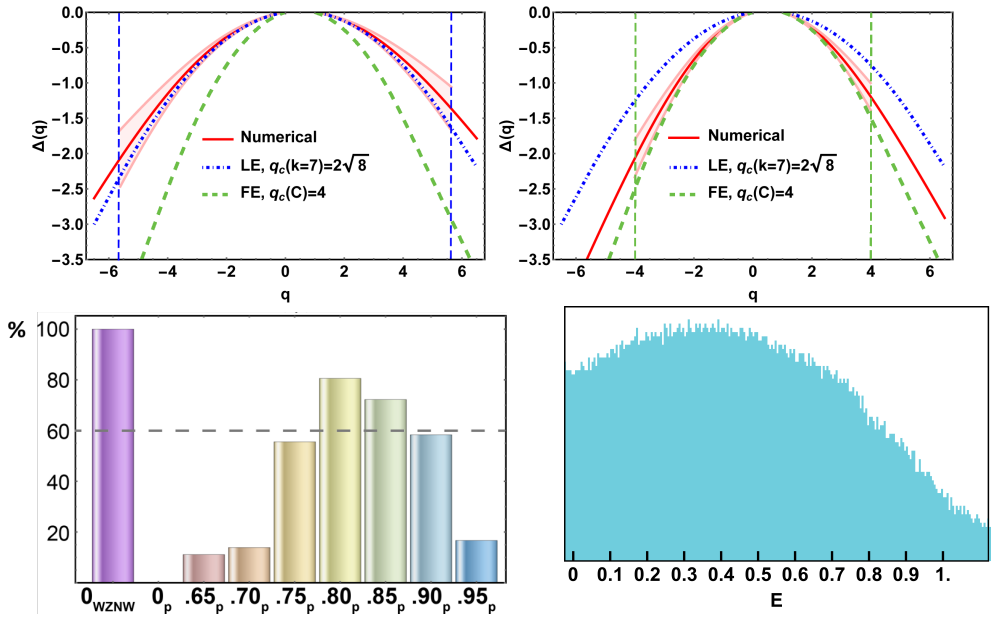

Figure 4.19: $k = 7$, $N = 34$. Box sizes $b = 4, 17$.

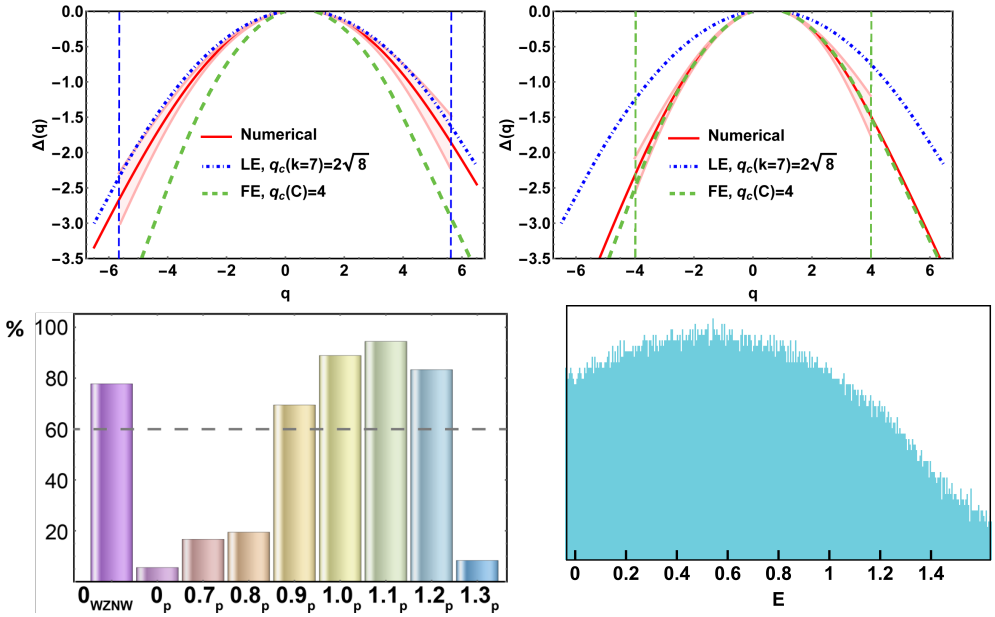

Figure 4.20: $k = 7$, $N = 36$. Box sizes $b = 3, 12$.

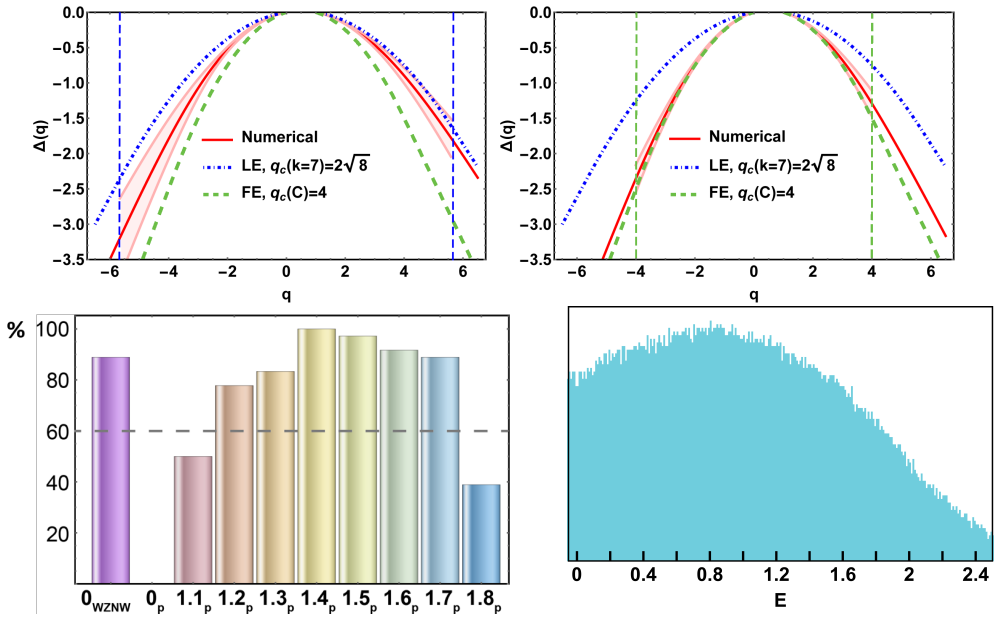

Figure 4.21: $k = 7$, $N = 38$. Box sizes $b = 2, 19$.

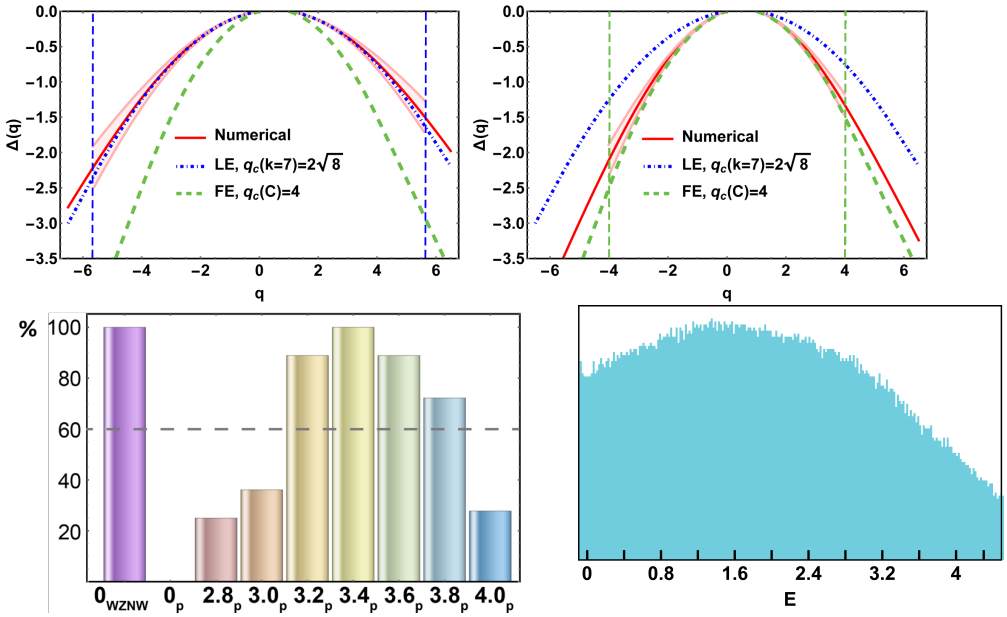

Figure 4.22: $k = 7$, $N = 42$. Box sizes $b = 3, 21$.

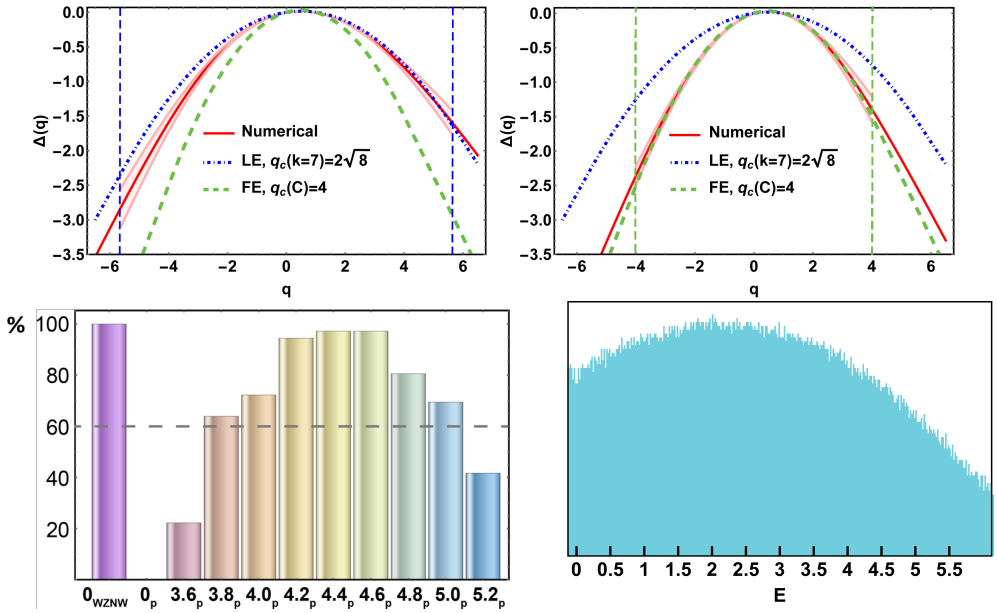

Figure 4.23: $k = 7$, $N = 44$. Box sizes $b = 2, 29$.

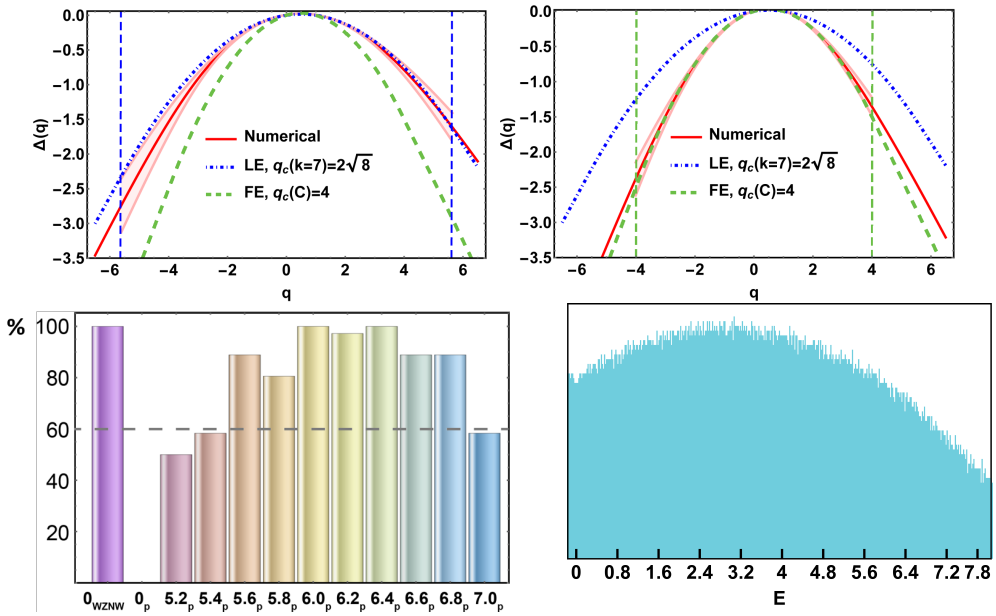

Figure 4.24: $k = 7$, $N = 46$. Box sizes $b = 2, 31$.

4.9 Conclusion and open questions

The class CI CFT governing the zero energy state can be formulated as a nonlinear sigma model with a Wess-Zumino-Novikov-Witten (WZNW) term [10, 11]. The energy perturbation breaks the symmetry from $G \times G$ down to G, where $G = \mathrm{Sp}(4n)$ (using replicas, with $n \to 0$). This perturbation is relevant, and presumably induces a renormalization group (RG) flow to another sigma model with lower symmetry. This argument is insufficient to choose between the orthogonal metal class AI [manifold $\mathrm{Sp}(4n)/\mathrm{Sp}(2n) \times \mathrm{Sp}(2n)$] and class C [manifold $\mathrm{Sp}(4n)/\mathrm{U}(2n)$] [28]. If the class CI model is deformed to class C "by hand," the WZNW term becomes a theta term (with theta proportional to k). Because this deformation does not necessarily correspond to a physical RG flow, it does not pin the physical value of theta.

The most important open question is how much of the physics linking TSCs to quantum Hall plateau transitions can be directly understood in terms of topology?

Chapter 5

Irradiated Luttinger semimetal: A factory for engineering Weyl semimetal

This chapter is mainly adapted from "S.A.A. Ghorashi, P. Hosur, C.S. Ting, arXiv:1801.04287"

5.1 Introduction

Topological phases of matter have attracted tremendous interest since the discovery of topological insulators. Topological protection of their edge and surface states is the hallmark of these systems, and leads to applications ranging from quantum computation to robust transport and exotic superconductivity [4, 6]. In contrast to topological insulators, which are gapped phases of matter like most topological

phases, it has been shown recently that gapless phases of matter can be topological as well [8, 75, 76, 77, 78, 79, 80]. Among them, Weyl semimetals (WSMs) have been particularly attractive due to their unconventional properties such as the chiral anomaly [82, 83], negative magnetoresistance [81, 82] and anomalous Hall effect [76, 79]. Experimental observation of these phases in TaAs [82, 84, 85] and photonic crystals [86] has ignited further interest in exploring these systems.

Very recently, new types of WSMs, namely, type-II and multi-WSMs were also discovered [87, 89, 90, 91]. The defining feature of type-II Weyl points is that the dispersion around them is strongly anisotropic, such that the slope changes sign along some directions. As a result, the Weyl nodes become the touching points between electron and hole Fermi surfaces, and result in properties different from those of type–I WSMs. For example, there are indications that the chiral anomaly depends on the relative direction of the magnetic field and the tilt of the cone, but the issue is still under debate [87, 88]. Moreover, unlike in type-I WSMs, the anomalous Hall effect can survive in type-II WSMs under certain conditions even when the nodes are degenerate [92]. On the other hand, multi-WSMs occur when the monopole charges of Weyl points are higher than 1, and can be either type-I or type-II [89, 90, 91]. In general, the search for Weyl semimetallic phases has been a vigorous field of research lately, and proposals have been put forth to engineer these phases in a tunable way by shining light on Dirac semimetals [99, 100], band insulators [101], stacked Graphene [102], line-nodal semimetals [100, 103] and crossing-line semimetals [96, 97]. Finally, proposals have been made to create tunable WSMs in pyrochlore iridates with Zeeman fields. [109, 115].

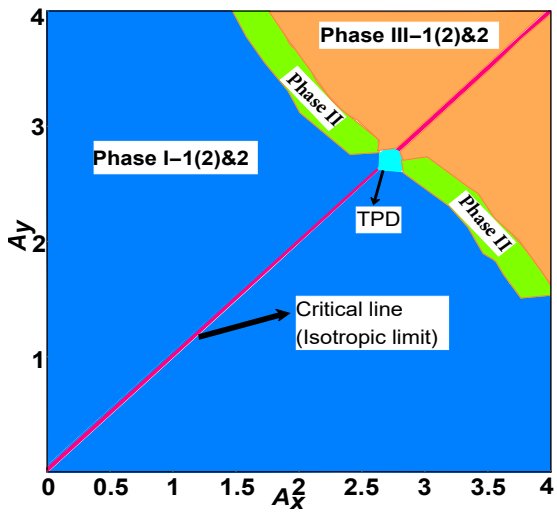

Figure 5.1: Phase diagram for 3D Floquet Luttinger semimetal (with respect to field strength with dimension of momentum see text (no unit)). Critical line (Isotropic limit): diagonal red line with two lower (w_l) and two higher (w_h) Weyl points on the k_z axis; phase I: $4w_l + 2w_h$, blue, where for bands bending oppositely (similarly), the $4w_l$ are type-I (type-II) denoted by $phaseI - 1(2)\&2$. The notation 1(2) denotes type-I (type-II) Weyl nodes in the respective phase. The first number is the type of lower and the second number after & indicates the type of the higher nodes. Phase III: $4w_h + 2w_l$, orange, where for bands bending oppositely (similarly), the $2w_l$ are type-I (type-II) and denoted by $phaseIII - 1(2)\&2$. Phase II, green, shows the transient phases between phase I and III where the flat bands in the k_z-direction ($k_x - k_y$ plane) for bands bending in opposite (same) directions, as well as merging and splitting of lower and upper nodes in $k_y - k_z$ and $k_x - k_z$ planes, respectively, occur. "TPD" denotes the triply degenerate point, which exists only for circular light.

In this chapter, we expand the horizons for creating tunable WSMs, by computing the band structure of a three-dimensional Luttinger semimetal with quadratic band touching irradiated by elliptically polarized light using Floquet theory. We find Weyl nodes of different charges (± 1 and ± 2), Weyl nodes of different types (type-I and type-II), and several phases which contain more than one class of Weyl nodes. We also stumble upon a situation where a pair of Weyl nodes form at infinity, and rapidly come in and merge with other nodes at finite $\mathbf{k}$. In a regularized lattice model, this pair would form at the edge of the Brillouin zone. Crucially, given the bare band structure, all these phases can be accessed by simply changing the properties of the light, making this system highly tunable. Fig. 5.1 summarizes the results of this paper. We expect these results to hold for real systems described by the Luttinger Hamiltonian [36], such as the zinc-blend semiconductors GaAs, HgTe, α-Sn etc. and a class of pyrochlore iridates [37, 104, 105, 25] studied recently.

5.2 Model and formalism

We begin with an isotropic version of the Luttinger Hamiltonian [36],

$$H = \frac{1}{2}\int_{\mathbf{k}} c^{\dagger}(\mathbf{k}) \left((\lambda_1 + \frac{5}{2}\lambda_2)k^2 - 2\lambda_2(\mathbf{J}.\mathbf{k})^2 - \mu \right) c(\mathbf{k}), \tag{5.1}$$

where $\lambda_{1,2}$ are positive constants, $\mathbf{k} = \{k_x, k_y, k_z\}$, $c(\mathbf{k}) = (c_{3/2\mathbf{k}}, c_{1/2\mathbf{k}}, c_{-1/2\mathbf{k}}, c_{-3/2\mathbf{k}})^T$, $\mathbf{J} = \{J^x, J^y, J^z\}$ are effective spin-3/2 operators, and $c_{m\mathbf{k}}$ denotes a fermion annihilation operator with momentum $\mathbf{k}$ and J_z quantum number m. The energy dispersions are $E(k) = (\lambda_1 \mp 2\lambda_2)k^2 - \mu$ for the $j = 3/2$ and the $j = 1/2$ bands, respectively. Time-reversal and inversion symmetries ensure that the four bands come in doubly

degenerate pairs due to Kramer's theorem. The degenerate pairs of bands curve the same (opposite) way for $\lambda_2 < 2\lambda_1$ ($\lambda_2 > 2\lambda_1$), as depicted in Fig. 5.2. When both bands bend the same way, Eq. (5.1) is widely used to model heavy- and light-hole bands in zinc-blende semiconductors [25]. Many properties of such a dispersion have been studied in the literature, including a recent study on the realization of fully gapped topological superconductivity with p-wave pairing which has states with exotic cubic and linear dispersions coexisting on the surface [14, 38]. On the other hand when bands bend oppositely, the above model is relevant for certain pyrochlore iridates as well as for some doped half-Heusler alloys such as LaPtBi [106, 107, 108]. Various aspects of this scenario have been explored as well, such as the phase diagram in the presence of electronic interactions [109], the effect of anisotropy [110] and superconductivity [111, 26]. Systems with higher effective spins and winding numbers have also attracted interest in the context of multi-Weyl phases [112] and the investigation of the spin quantum Hall plateau transition on the surface of topological superconductors with general winding numbers [113].

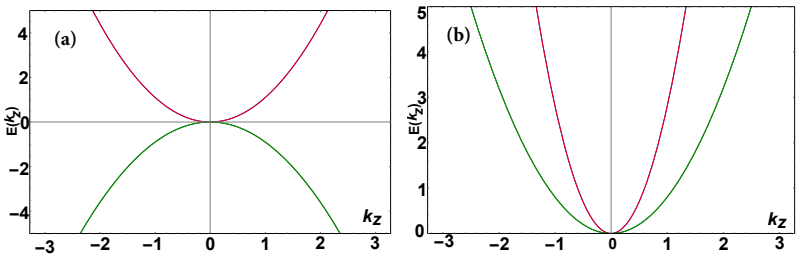

Figure 5.2: Energy dispersion of Eq. (5.1) for (a) $\lambda_1 = 0.1$ and $\lambda_2 = 0.5$ with $J = 3/2$ (red) bending down $J = 1/2$ (blue) bending up, and (b) $\lambda_1 = 1.8$ and $\lambda_2 = 0.5$ where both bands bend up. Note that the bands are doubly degenerate.

Here, we study another aspect of this model. By employing machinery from Floquet theory, we investigate light-matter interactions in this model in both band-bending scenarios. We consider periodic driving induced by laser light with a general vector potential $\boldsymbol{\mathcal{A}}(t) = (A_x \cos(\omega t), A_y \eta \sin(\omega t), 0)$, where $\eta = \pm 1$ corresponds to right-handed and left-handed polarizations of the light, respectively, and $A_i \propto E_i/\omega$, where E_i is its electric field. The time-dependent Hamiltonian can be written as $H(\mathbf{k}, t) = \sum_n H_n(\mathbf{k}) e^{in\omega t}$, where $H_{\pm n}(\mathbf{k}) = \frac{1}{T}\int_0^T H(\mathbf{k}, t) e^{\pm in\omega t}$.

The effective time-independent Hamiltonian in the high frequency limit, as dictated by Floquet theory, is [95, 98],

$$H_{eff}(\mathbf{k}) = H_0 + \sum_{n\geq 1} \frac{[H_{+n}, H_{-n}]}{n\omega} + O\left(\frac{1}{\omega^2}\right). \tag{5.2}$$

where,

$$H_1 = (\lambda_1 + \frac{5}{2}\lambda_2)\mathbf{k}.\mathbf{A} - 2\lambda_2\{\mathbf{J}.\mathbf{k}, \mathbf{J}.\mathbf{A}\} \tag{5.3}$$

$$H_2 = \frac{1}{4}((\lambda_1 + \frac{5}{2}\lambda_2)\mathbf{A}^2 - 2\lambda_2(\mathbf{J}.\mathbf{A})^2) \tag{5.4}$$

$$H_{-n} = H_n^\dagger, \tag{5.5}$$

and $\mathbf{A} = (A_x, i\eta A_y, 0)$. The Floquet perturbation series is controlled by parameter $\gamma = \lambda e^2 E^2/\hbar\omega^3$, where λ is either λ_1 or λ_2 which are of the same order of magnitude and have units of inverse mass, E is the magnitude of the electric field of the incident light and c is the speed of light in the medium. Clearly, $\gamma \ll 1$ at high enough frequencies, thus controlling the Floquet expansion. We discuss the estimation of this parameter in the real experiments in the concluding section. In the meantime, we work in the units $e = \hbar = 1$. We first analyze the limit of circular polarization, which is the only case can be fully studied analytically. Then, we analyze the general

case of elliptical polarization.

5.3 Circularly polarized light

.

Because H is quadratic in $\mathbf{k}$, $H_n = 0$ for $n > 2$ in Eq. (5.2). The terms coming from $n = \pm 2$ are momentum-independent, and it is their competition with the $\mathbf{k}$-dependent terms arising from $n = \pm 1$ that proves to be essential in realizing the various WSMs. In other words, the leading order correction in $\mathbf{A}$ is insufficient, and it is necessary to go to a higher order. For circularly polarized light, rotational symmetry ensures that Weyl points appear only on the k_z axis, which makes extracting the salient features of the model analytically possible. For $k_x = k_y = 0$, the effective Hamiltonian reads

$$H_{eff}(k_z) = H_0(k_z) + \frac{2i\eta A^2\lambda_2^2}{\omega}\Bigg(- k_z^2[\{J_x, J_z\}, \{J_y, J_z\}] \tag{5.6}$$

$$+ \frac{A^2}{8}[\ J_y^2 - J_x^2, \{J_x, J_y\}]\Bigg), \tag{5.7}$$

with dispersions of $E_{1,\pm} = (\lambda_1 + 2\lambda_2)k_z^2 \pm (3A^2\lambda_2^2\eta(A^2 - 8k_z^2))/2\omega - \mu$ and $E_{2,\pm} = (\lambda_1 - 2\lambda_2)k_z^2 \pm (3A^2\lambda_2^2\eta(A^2 + 8k_z^2))/2\omega - \mu$. Note that introduction of circularly polarized light has broken time-reversal symmetry and lifted the double degeneracy of the bands. Inversion symmetry survives, though, because only even powers of the light amplitude enter H_{eff}. The four non-degenerate bands intersect in various pairs, giving rise to Weyl nodes at $\mathbf{K}_1 = (0, 0, \pm A/2\sqrt{2})$ and $\mathbf{K}_2 = (0, 0, \mp A^2\sqrt{3\lambda_2/\omega}/2)$.

We can compute the monopole charge of each node by writing an effective low energy Hamiltonian around in the form $H_k \propto \mathbf{n}(\mathbf{k}) \cdot \boldsymbol{\sigma}$ and using,

$$W_n = \frac{1}{8\pi} \int_S d^2\mathbf{k} \epsilon^{ijk} \mathbf{n}.(\partial_j \mathbf{n} \times \partial_k \mathbf{n}) \tag{5.8}$$

where $\mathbf{n}$ is a unit vector and the integration is over a surface S surrounding the node. We obtain $W_n = \pm 1$ and $W_n = \pm 2$ for K_1 and K_2 respectively. This is a remarkable result, that single and double-Weyl nodes coexist at different energies, thus allowing us to access both dynamically by tuning the chemical potential. As is clear, the positions of single Weyl points are only a function of the light parameters while the locations of the double-Weyl points also depend on the band structure parameter, λ_2. Moreover, for circularly polarized light, there is a special point in parameter space, namely, $A_m = \pm\sqrt{\omega/6\lambda_2}$ where the two types of nodes merge and form a triply degenerate point (TDP).

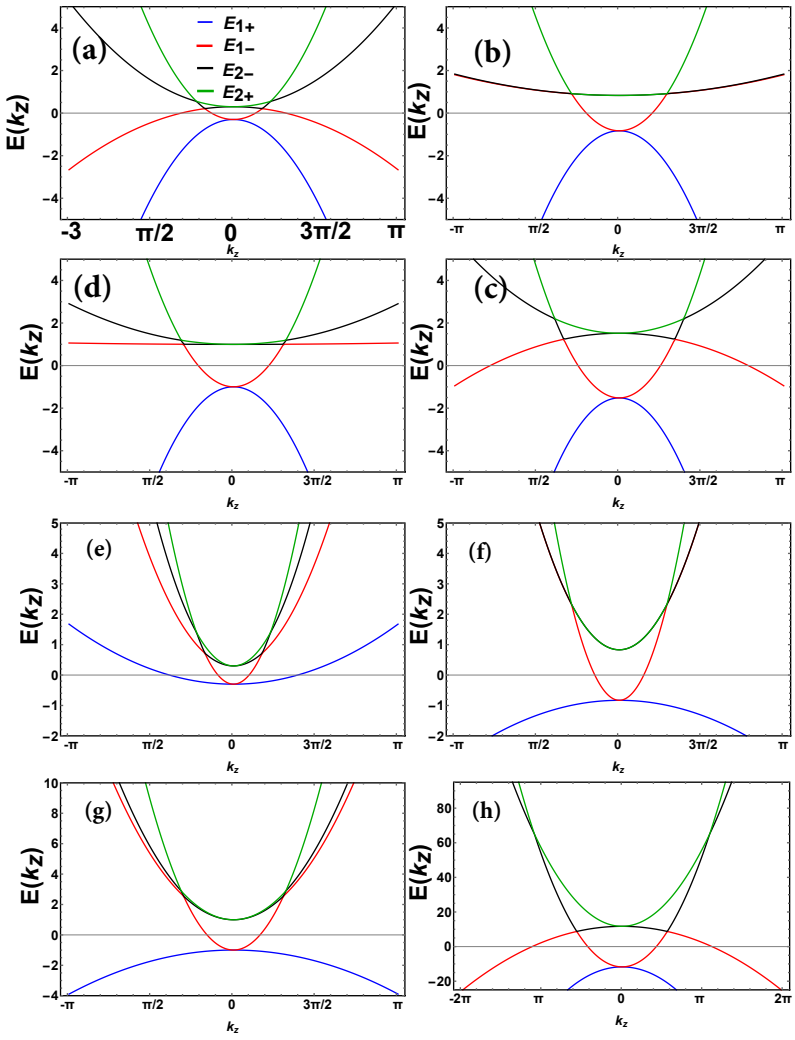

Figure 5.3: Evolution of the Weyl nodes with light amplitude A. (a)-(d) show $A = 2, 2.58, 2.7$ and 3, respectively for bands bending oppositely. For (e)-(h), we used $A = 2, 2.58, 2.7$ and 5, respectively, to show the type-II to type-I phase transition for high enough intensity with both bands bending in same direction. $\lambda_1 = 0.1, \lambda_2 = 0.5$ ($\lambda_1 = 1.8, \lambda_2 = 0.5$) are used for bands bending oppositely (similarly). $\omega = 20$, $\mu = 0$ and $\eta = 1$ is used for all of the plots.

Fig. 5.3(a-d) shows the evolution of the band structure with the light intensity, for a representative set of parameters with $\eta\lambda_2 > 0$ in a scenario with bands bending oppositely. This corresponds to evolution along the $A_x = A_y$ line in Fig. 5.1. Two pairs of nodes appear (Fig. 5.3a) as soon as light is turned on. The nodes higher (lower) in energy are type-II (type-I), have monopole charge ± 1 (± 2) and occur at K_1 (K_2). On increasing A, the lower nodes flatten along k_z (not shown) and transition into type-II nodes, before merging with the upper nodes at the TDP at $A = A_m$ (Fig. 5.3b). On further increasing A, the bands cross, and the charge ± 2 nodes end up being higher in energy than the charge ± 1 nodes (Fig. 5.3c). The latter then transitions back from type-II to type-I (Fig. 5.3d). In summary, the upper nodes are always type-II, while the lower nodes evolve from type-I to type-II and back to type-I. Naturally, the bands hosting the lower Weyl nodes flatten twice during this evolution, once at each transition between type-I and type-II characters. The charges are ± 1 (± 2) for the upper (lower) nodes for low intensity, and the correspondence gets reversed as A is tuned across the TDP.

Fig. 5.3(e-h) show the evolution when the bare bands bend the same way. It shows the same trend as the case where the bare bands bend oppositely, except that all the nodes are type-II. Moreover, there is a type-II to type-I transition at high intensity, as shown in Figs. 5.3(g) and 5.3(h).

5.4 Elliptically polarized light

Now, we turn to the more general case of elliptically polarized light, i.e, $A_x \neq A_y$. The phase diagram is much richer when the incident light is anisotropic in the field's amplitudes. In the following, we analyze various driven phases in the two band-bending possibilities shown in Fig. 5.2.

Let us first study Eq. (5.4) when the bands are bent oppositely. The phase evolution for this case is depicted in Fig. 5.4. In describing the evolution, we keep A_y fixed at a high or a low value, and tune A_x from 0 to A_y.

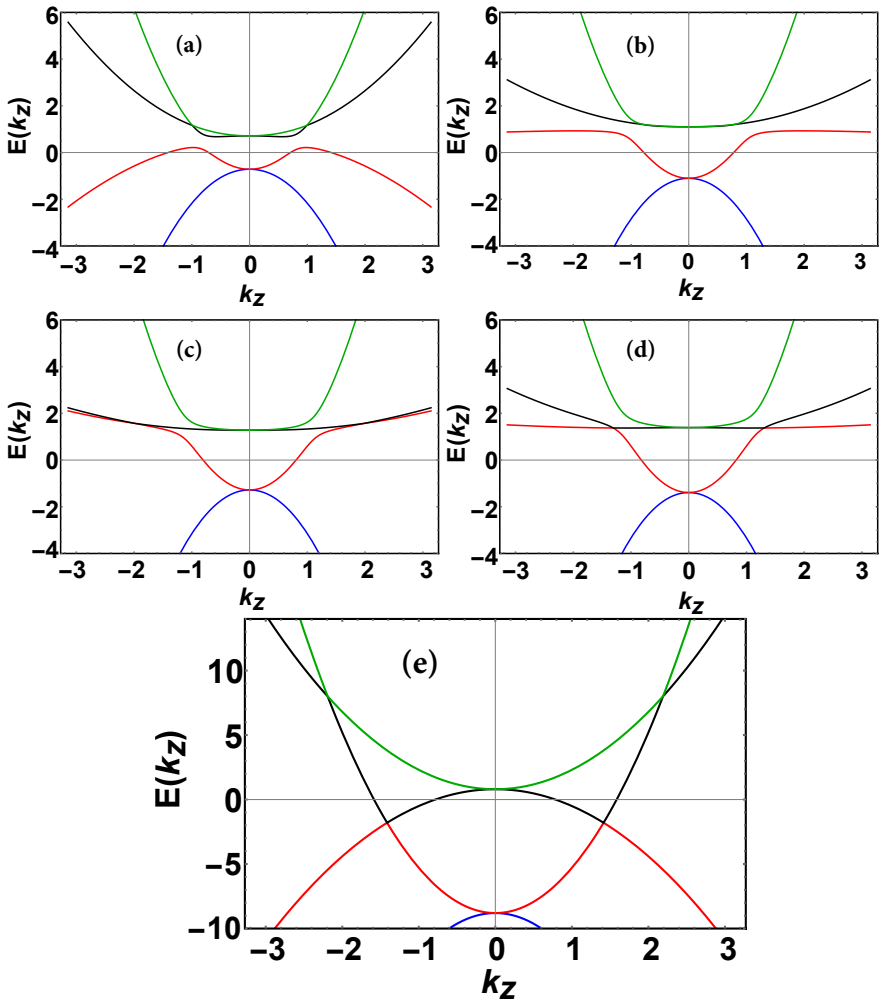

Figure 5.4: (a)-(e) show the $k_x = k_y = 0$ cut for $A_y = 4$ and $A_x = 1, 1.48, 1.68, 1.8, 4$ respectively. $\lambda_1 = 0.1, \lambda_2 = 0.5$, $\omega = 20$, $\eta = 1$ and $\mu = 0$ ($\mu = 4$) for (a)-(d)((e))

Let us first look at high A_y. For large anisotropy with $A_y \gg A_x$, there are 4 type-I nodes of unit monopole charge in the $k_y - k_z$ plane and 2 type-II nodes of charge ± 2 at higher energies on the k_z-axis (Fig. 5.4a and 5.6a). On increasing A_x, the two higher nodes split into four type-II nodes of unit charge in the $k_x - k_z$

plane (Fig. 5.4b and 5.6b). On further increasing A_x a pair of type-II nodes of unit charge come in on the k_z axis from $k_z = \pm\infty$ while there are still 4 nodes in $k_y - k_z$ plane (Fig. 5.4c and 5.5a). The new node at $k_z > 0$ presumably has a monopole charge opposite to that of the two nodes in the $k_y - k_z$ plane at $k_z > 0$; an analogous condition holds for $k_z < 0$ with all monopole charges reversed. Finally, the nodes in each triplet merge to yield two type-II nodes of charge ± 1 (Fig. 5.5) on the k_z axis. These nodes change character from type-II to type-I, accompanied by the flattening of one of the bands participating in the nodes (Fig. 5.4d), and survive in this form up to the circularly-polarized limit (Fig. 5.4e). In the meantime, the four higher nodes remain type-II with unit charge, but merge into two type-II, charge ± 2 nodes in the limit of $A_x = A_y$. Therefore we end up of 2 higher (type-II, ± 2) and lower (type-I, ± 1) nodes as explained in the previous section (Fig. 5.4e). It should be noted that the TDPs are absent for elliptical polarization.

However, for lower A_y, situation is different. In this case the situations of Fig. 5.4(b-d) do not happen. In another words, for lower A_y, the upper nodes do not split, while the merging of lower four points happens near the isotropic limit. Moreover, no flat-line occurs, and the upper nodes (type-II) have charge ± 1 and lowers (type-I) have ± 2 charges.

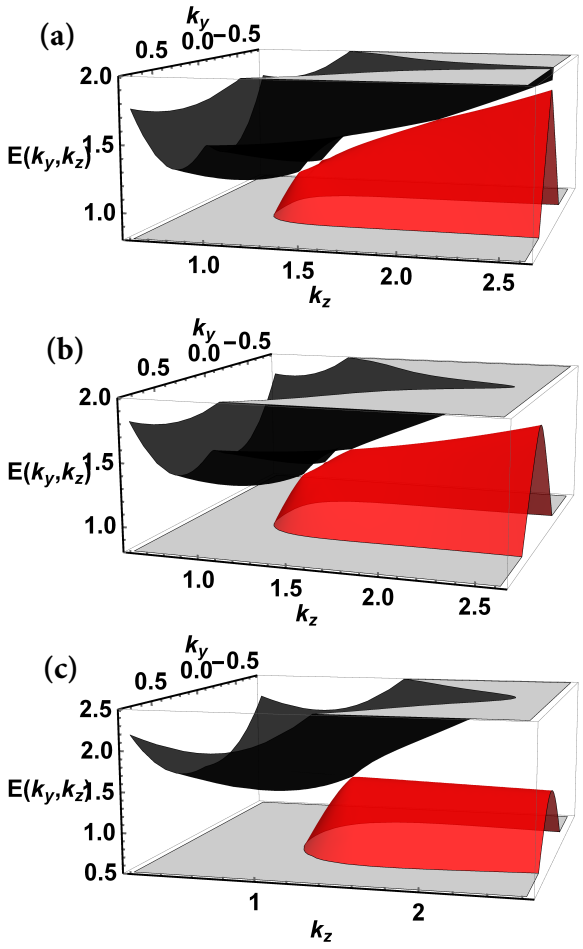

Figure 5.5: Appearance of type-II node from infinity (a) while there are two nodes on the $k_y - k_z$ plane. The node from infinity moves towards origin (b) and merges with two other nodes on the k_z axis (c). (a)-(c) we used fixed $A_y = 4$ and $A_x = 1.68, 1.72, 1.85$, respectively. To increase the resolution only evolution of the nodes between two relevant bands is depicted. Also, only one side of plot is shown.

When both bare bands bend in same direction, the phase diagram undergoes almost the same evolution as the case with bands bent oppositely. In particular, it

starts with four lower and two higher nodes, which, after a series of merging and splitting, yields a phase with two lower and four higher nodes. Finally, in the circular polarization limit, the higher nodes merge, leaving only two lower and two higher nodes. However, there are couple of differences. Firstly, as we mentioned in the previous section, nodes are type-II for most amplitude ranges. The second, instead of a flat line along k_z, there is a "flat-band" in the $k_x - k_y$ plane for the lower nodes (Fig. 5.6c). The flat-line along k_z does happen, but only for very large A_y. This is consistent with the type-II to type-I transition that was found to occur at high intensities in the isotropic limit for bare bands bending in the same direction.

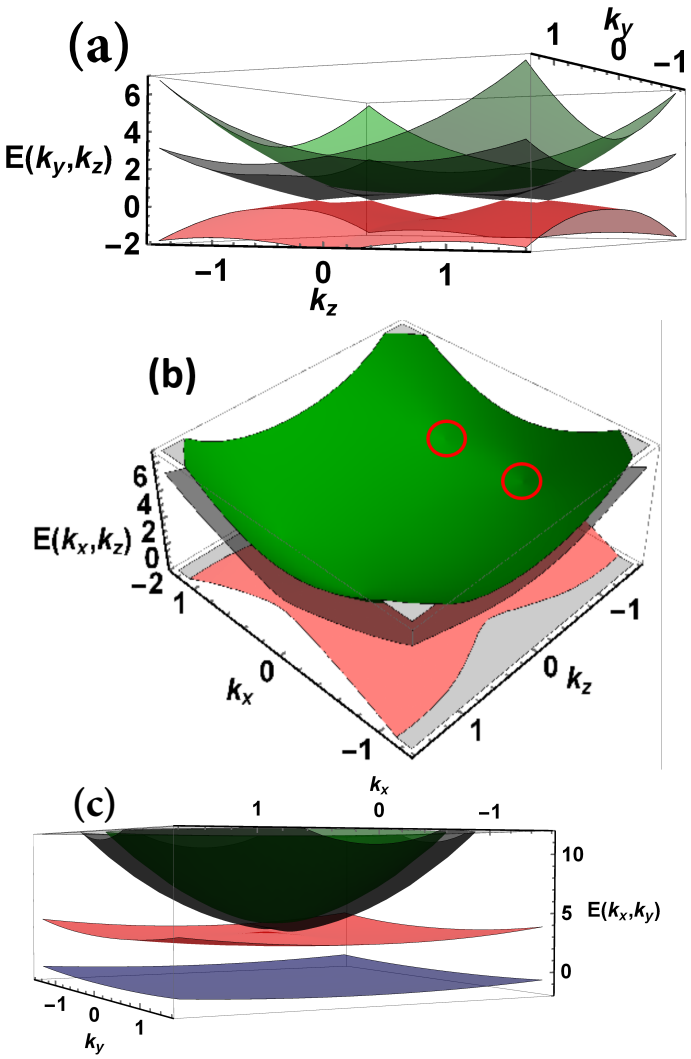

Figure 5.6: Representative 3D plots: (a) shows a representative plot in phase (I) illustrating four nodes in the $k_y - k_z$ plane with $A_y = 4$ and $A_x = 1$, (b) shows a representative plot in phase (III) illustrating four nodes in $k_x - k_z$ plane with $A_y = 4$ and $A_x = 2$. Red rings denote nodes in the upper bands. (c) shows a representative plot of the flat-bands in $k_x - k_y$ in the scenario with both bands bending in same direction (Fig. 2.2b) with $A_y = 4$ and $A_x = 1.6$. We used $\omega = 20$, $\eta = 1$ and $\mu = 0$ for (a)-(c).

5.5 Discussion, experimental considerations and concluding remarks

In this chapter we have studied the Floquet theory of the three-dimensional Luttinger semimetal with quadratic band touching points. We have found that depending on the orientation of bands and light parameters, both type I and II Weyl nodes with single and double monopole charges at different energies can be generated. In particular we arrive at the following main results:

- When the incident light is circularly polarized, we have solved the problem analytically and have obtained two nodes with charge ± 1 and two other nodes with ± 2 at different energies. For both band bending scenarios, the higher nodes are always type-II while the lower ones can be type-I or II depending on light parameters. We found that at a certain light intensity, both pairs of nodes merge to form two TDPs. This is a special point which exists only for circularly polarized light and is a function of both light and band structure parameters.

- For the elliptically polarized light, we have only solved system numerically. For both bands bending scenarios, for large anisotropy, $A_x \ll A_y$, there are two higher nodes on the k_z axis and four lower nodes in $k_y - k_z$ plane. Then, when the A_y is held fixed at a small value and A_x is increased, the four lower nodes merge around $A_x \sim A_y$. However, for high enough A_y, on increasing A_x, the lower Weyl nodes merge and then tilt back and turn into a flat-line (flat-band)

for bare bands bending oppositely (similarly) and make two nodes. On the other hand the higher nodes deform to nearly flat lines and then split to four nodes in $k_x - k_z$ plane which finally merge at isotropic limit.

Therefore, we conclude that the Luttinger semimetal with parabolic dispersion provides a master platform for realizing various types of WSMs from type I to type II with four nodes or two nodes, as well as single and double monopoles. Remarkably, we found that single and double-Weyl can coexist at different energies, so either ones can be accessed through controlled doping of the system and tuning of laser light. To the best of our knowledge this is the only system that reported so far with this level of tunability for broad range of possible Weyl phases. In addition, irradiated Luttinger semimetals is the only example so far discovered with Weyl node with different monopole charges coexist, making it feasible for the possible applications of both single and double WSMs. To the best of our knowledge our work is the only example that can generate such a broad range of WSMs from a system with no Weyl nodes. There have been some recent studies [96, 97], where photo-induced multi-Weyl phases were generated from crossing-line systems.

The Luttinger Hamiltonian describes a wide range of materials from semiconductors to pyrochlore iridates and half-Heuslers which are accessible experimentally, unlike the other semimetals such as Dirac, loop-node, or linked semimetals, where experimental examples are rare or non-existent. Therefore, this work might facilitate the experimental realizations of photoinduced WSMs. Using $\lambda_2 = 4.2/m_0$ for HgTe, where m_0 is the bare electron mass, $\hbar\omega = 120meV$ and an electric field of $E_0 = 2.5 \times 10^7 V/m$ – typical values for pump-probe experiments [114] – we estimate

the perturbation parameter $\gamma = \lambda e^2 E^2/\hbar\omega^3 \sim 10^{-10}$, so the Floquet expansion is certainly well-controlled. The only word of caution is that, as with all three-dimensional Floquet systems, our proposal only works for films thin enough for the electric field to penetrate the system substantially.

Chapter 6

Conclusion

In dissertation we studied the several phases and critical phenomena in topological superconductors and semimetals. In particular, we investigated various aspects of a class of materials with effective spin of 3/2, so-called Luttinger semimetal.

In chapter 3, we showed that p-wave topological superconductivity of $J = 3/2$ (spin-3/2 generalization of 3He-B) lead to a surface states which a linear and cubic dispersions coexisting with bulk winding number 4. We showed that in the clean limit that, unlike the spin-1/2 case, the only short-range interaction is marginally relevant, so it spontaneously breaks time-reversal symmetry and opens a gap on the surface leading to the thermal quantum Hall effect. In the dirty limit, however, we have proven that surface flows to a critical phase governed by CFT $SO(n \to 0)_4$ where longitudinal thermal conductivity is quantized universally, the same CFT class that describes the dirty surface of spin-1/2 systems. Therefore, we concluded that disorder stabilizes the surface.

Next, motivated by recent studies suggesting non-s-wave pairing superconductivity in hole-doped half Heusler systems, we turned on the spin-orbit coupling leading to Luttinger Hamiltonian with quadratic band touching where bands bend oppositely. In this case, depending on doping on the valence or conduction bands, we get two different surface states, with same bulk winding number $\nu = 3$ though. In this dissertation, we focused on the hole-doped scenario where surface possess cubic dispersion. In this case interaction is irrelevant in clean limit, and we performed the same disorder analysis of previous case without spin-orbit coupling. We again showed that same CFT theory is resulted by adding non-magnetic disorder. As a follow-up to this project, one could study the electron-doped case where surface show a linear dispersion at Γ point and a zero-energy ring states at finite-momentum.

In chapter 4, we studied surface states of three-dimensional superconductors in class "CI" with the goal to investigate the idea of topological protection for the case of finite-energy states. In this case we showed that, surprisingly, the finite-energy states show critical delocalization with a different multifractal spectrum, corresponding to spin quantum plateau transition of "class C", which is known to be mapped to classical percolation in 2D. Moreover, we showed that unlike the common believe that the percolation transition happens at fine-tuned values of the energy, on the surface state of topological superconductors almost all the states with finite-energy sit at the plateau transition without fine-tuning. We expect that finite-temperature physics of these surface states be governed by percolation. As the continuation of this work one could study the other symmetry classes. In particular class DIII which is experimentally more relevant. However, less is known about the thermal Hall plateau

transition of class "D".

Finally, in chapter 5, we studied the interaction of light with Luttinger semimetal. Via Floquet theory formalism, we showed that irradiated three-dimensional Luttinger semimetal is a factory for engineering various Weyl semimetals. Both the limit of circular and elliptical polarized lights investigated. We showed that one can get both type-I and type-II as well as single and double Weyl semimetals. Moreover, we showed that irradiated Luttinger semimetal provides a highly tunable setup for tuning between various Weyl phases.

Bibliography

[1] A. Richardella, P. Roushan, S. Mack, B. Zhou, D. A. Huse, D. D. Awschalom, and A. Yazdani, *Visualizing Critical Correlations Near the Metal-Insulator Transition in Ga1-xMnxAs*, Science, **327**, (2010).

[2] Y. Morita and Y. Hatsugai, *Near critical states of random dirac fermions*, Phys. Rev. Lett. **79**, 3728 (1997).

[3] N. P. Armitage, E. J. Mele, A. Vishwanath, *Weyl and Dirac semimetals in three-dimensional solids*, Rev. Mod. Phys **90**, 015001 (2018).

[4] M. Z. Hasan and C. L. Kane, *Colloquium: Topological insulators*, Rev. Mod. Phys. **82**, 3045 (2010); X.-L. Qi and S.-C. Zhang, *opological insulators and superconductors*, *ibid.* **83**, 1057 (2011).

[5] B. A. Bernevig and T. L. Hughes, *Topological Insulators and Topological Superconductors* (Princeton University Press, Princeton, New Jersey, 2013).

[6] C.-K. Chiu, J. C. Y. Teo, A. P. Schnyder, and S. Ryu, *Classification of topological quantum matter with symmetries*, Rev. Mod. Phys. **88**, 035005 (2016).

[7] T. Mizushima, Y. Tsutsumi, T. Kawakami, M. Sato, M. Ichioka, and K. Machida, *Symmetry-Protected Topological Superfluids and Superconductors From the Basics to 3He*, J. Phys. Soc. Jpn. **85**, 022001 (2016).

[8] G. E. Volovik, *The Universe in a Helium Droplet* (Oxford University Press, Oxford, England, 2003).

[9] A. P. Schnyder, S. Ryu, A. Furusaki, and A. W. W. Ludwig, *Classification of topological insulators and superconductors in three spatial dimensions*, Phys. Rev. B 78, 195125 (2008).

[10] M. S. Foster and E. A. Yuzbashyan, *Interaction-Mediated Surface-State Instability in Disordered Three-Dimensional Topological Superconductors with Spin SU(2) Symmetry*, Phys. Rev. Lett. **109**, 246801 (2012).

[11] M. S. Foster, H.-Y. Xie, and Y.-Z. Chou, *Topological protection, disorder, and interactions: Survival at the surface of three-dimensional topological superconductors*, Phys. Rev. B **89**, 155140 (2014).

[12] Y.-Z. Chou and M. S. Foster, *Chalker scaling, level repulsion, and conformal invariance in critically delocalized quantum matter: Disordered topological superconductors and artificial graphene*, Phys. Rev. B **89**, 165136 (2014).

[13] H.-Y. Xie, Y.-Z. Chou, and M. S. Foster, *Surface transport coefficients for three-dimensional topological superconductors*, Phys. Rev. B **91**, 024203 (2015).

[14] W. Yang, Y. Li, and C. Wu, *Topological Septet Pairing with Spin-*3/2 *Fermions: High-Partial-Wave Channel Counterpart of the* ^{3}*He-B Phase*, Phys. Rev. Lett. **117**, 075301 (2016).

[15] C. Fang, B. A. Bernevig, and M. J. Gilbert, *Tri-Dirac surface modes in topological superconductors*, Phys. Rev. B **91**, 165421 (2015).

[16] H. Kim, K. Wang, Y. Nakajima, R. Hu, S. Ziemak, P. Syers, L. Wang, H. Hodovanets, J. D. Denlinger, P. M. R. Brydon, D. F. Agterberg, M. A. Tanatar, R. Prozorov, and J. Paglione, *Beyond Triplet: Unconventional Superconductivity in a Spin-3/2 Topological Semimetal*, arXiv:1603.03375.

[17] P. M. R. Brydon, L. Wang, M. Weinert, and D. F. Agterberg, *Pairing of* $j = 3/2$ *Fermions in Half-Heusler Superconductors*, Phys. Rev. Lett. **116**, 177001 (2016).

[18] C. L. Kane and M. P. A. Fisher, *Quantized thermal transport in the fractional quantum Hall effect*, Phys. Rev. B **55**, 15832 (1997).

[19] N. Read, and D. Green, *Paired states of fermions in two dimensions with breaking of parity and time-reversal symmetries and the fractional quantum Hall effect*, Phys. Rev. B **61**, 10267 (2000).

[20] A. Capelli, M. Huerta, and G. Zemba, *Thermal Transport in Chiral Conformal Theories and Hierarchical Quantum Hall States*, Nucl. Phys. B **636**, 568 (2002).

[21] Z. Wang, X.-L. Qi, and S.-C. Zhang, *Topological field theory and thermal responses of interacting topological superconductors*, Phys. Rev. B **84**, 014527 (2011).

[22] S. Ryu, J. E. Moore, and A. W. W. Ludwig, *Electromagnetic and gravitational responses and anomalies in topological insulators and superconductors*, Phys. Rev. B **85**, 045104 (2012).

[23] M. Stone, *Gravitational anomalies and thermal Hall effect in topological insulators*, Phys. Rev. **85**, 184503 (2012).

[24] T. Senthil and M. P. A. Fisher, *Quasiparticle localization in superconductors with spin-orbit scattering*, Phys. Rev. B **61**, 9690 (2000).

[25] P. Y. Yu and M. Cardona, *Fundamentals of Semiconductors* (Springer-Verlag, Berlin, 1996).

[26] B. Roy, S. A. A. Ghorashi, M. S. Foster, A. H. Nevidomskyy, *Topological superconductivity of spin-3/2 carriers in a three-dimensional doped Luttinger semimetal*, arXiv: 1708.07825.

[27] Y. Shimizu, A. Yamakage, and K. Nomura, *Quantum thermal Hall effect of Majorana fermions on the surface of superconducting topological insulators*, Phys. Rev. B **91**, 195139 (2015).

[28] F. Evers and A. D. Mirlin, *Anderson Transitions*, Rev. Mod. Phys. **80**, 1355 (2008).

[29] C. C. Chamon, C. Mudry, and X.-G. Wen, *Localization in Two Dimensions, Gaussian Field Theories, and Multifractality*, Phys. Rev. Lett. **77**, 4194 (1996).

[30] M. S. Foster, S. Ryu, and A. W. W. Ludwig, *Termination of typical wavefunction multifractal spectra at the Anderson metal-insulator transition: Field theory description using the functional renormalization group*, Phys. Rev. B **80**, 075101 (2009); T. Vojta, *Viewpoint: Atypical is normal at the metal-insulator transition*, Physics **2**, 66 (2009).

[31] T. I. Baturina *et al.*, *Quantum-critical region of the disorder-driven superconductorinsulator transition*, Physica C **468**, 316 (2008); M. V. Feigel'man, L. B. Ioffe, V. E. Kravtsov, and E. A. Yuzbashyan, *Eigenfunction Fractality and Pseudogap State near the Superconductor-Insulator Transition*, Phys. Rev. Lett. **98** 027001 (2007).

[32] M. V. Feigel'man, L. B. Ioffe, V. E. Kravtsov, and E. Cuevas, *Fractal superconductivity near localization threshold*, Ann. Phys. **325**, 1390 (2010).

[33] Y. J. Park, S. B. Chung, and J. Maciejko, *Surface Majorana fermions and bulk collective modes in superfluid 3He-B*, Phys. Rev. B **91**, 054507 (2015).

[34] J. J. Sakurai, *Modern Quantum Mechanics* (Addison-Wesley, Reading, Mass., 1994).

[35] A. Altland and B. Simons, *Condensed Matter Field Theory*, 2nd. Ed. (Cambridge University Press, Cambridge, England, 2010).

[36] J. M. Luttinger, *Quantum Theory of Cyclotron Reso- nance in Semiconductors: General Theory*, Phys. Rev. **102**, 1030 (1956).

[37] S. Murakami, S-C. Zhang, and N. Nagaosa, *SU(2) non- Abelian holonomy and dissipationless spin current in semiconductors*, Phys. Rev. B 69, 235206 (2004).

[38] S. A. A. Ghorashi, S. Davis, M. S. Foster, *Disorder-enhanced topological protection and universal quantum criticality in a spin-3/2 topological superconductor*, Phys. Rev. B **95**, 144503 (2017).

[39] P. Goswami and B. Roy, *Axionic superconductivity in three-dimensional doped narrow-gap semiconductors*, Phys. Rev. B 90, 041301(R), (2014).

[40] L. Savary, J. Ruhman, J. W. F. Venderbos, L. Fu, and P. A. Lee, *Superconductivity in three-dimensional spin-orbit coupled semimetals*, arXiv:1707.03831

[41] X.-L. Qi, T. L. Hughes, and S.-C. Zhang, *Topological invariants for the Fermi surface of a time-reversal-invariant superconductor*, Phys. Rev. B **81**, 134508 (2010).

[42] A. LeClair and D. J. Robinson, *Super spin-charge separation for class A, C and D disorder*, J. Phys. A **41**, 452002 (2008).

[43] S. Ryu and Y. Hatsugai, *Numerical replica limit for the density correlation of the random Dirac fermion*, Phys. Rev. B **63**, 233307 (2001).

[44] D. Carpentier and P. Le Doussal, *Glass transition of a particle in a random potential, front selection in nonlinear renormalization group, and entropic phenomena in Liouville and sinh-Gordon models*, Phys. Rev. E **63**, 026110 (2001).

[45] Y. V. Fyodorov, *Multifractality and freezing phenomena in random energy landscapes: An introduction*, Physica A **389**, 4229 (2010).

[46] A. Comtet and C. Texier, *One-dimensional disordered supersymmetric quantum mechanics: A brief survey*, in *Supersymmetry and Integrable Models*, edited by H. Aratyn, T. D. Imbo, W.-Y. Keung, and U. Sukhatme (Springer-Verlag, Berlin, 1998).

[47] S. A. Trugman, *Localization, percolation, and the quantum Hall effect*, Phys. Rev. B **27**, 7539 (1983).

[48] B. Huckestein, *Scaling theory of the integer quantum Hall effect*, Rev. Mod. Phys. **67**, 357 (1995);

[49] V. Kagalovsky, B. Horovitz, Y. Avishai, and J. T. Chalker, *Quantum Hall Plateau Transitions in Disordered Superconductors*, Phys. Rev. Lett. **82**, 3516 (1999).

[50] I. A. Gruzberg, A. W. W. Ludwig, and N. Read, *Exact Exponents for the Spin Quantum Hall Transition*, Phys. Rev. Lett. **82**, 4524 (1999).

[51] T. Senthil, J. B. Marston, and M. P. A. Fisher, *Spin quantum Hall effect in unconventional superconductors*, Phys. Rev. B **60**, 4245 (1999).

[52] J. Cardy, *Linking Numbers for Self-Avoiding Loops and Percolation: Application to the Spin Quantum Hall Transition*, Phys. Rev. Lett. **84**, 3507 (2000).

[53] E. J. Beamond, J. Cardy, and J. T. Chalker, *Quantum and classical localization, the spin quantum Hall effect, and generalizations*, Phys. Rev. B **65**, 214301 (2002).

[54] F. Evers, A. Mildenberger, and A. D. Mirlin, *Multifractality at the spin quantum Hall transition*, Phys. Rev. B **67**, 041303R (2003).

[55] A. D. Mirlin, F. Evers, and A. Mildenberger, *Wavefunction statistics and multifractality at the spin quantum Hall transition*, J. Phys. A **36**, 3255 (2003).

[56] For a review, see e.g. J. Cardy, *Quantum Network Models and Classical Localization Problems*, in *50 Years of Anderson Localization*, ed. E. Abrahams (World Scientific, Singapore, 2010).

[57] A. W. W. Ludwig, M. P. A. Fisher, R. Shankar, G. Grinstein, *Integer quantum Hall transition: An alternative approach and exact results*, Phys. Rev. B, **50**, 7526 (1994).

[58] P. M. Ostrovsky, I. V. Gornyi, and A. D. Mirlin, *Quantum Criticality and Minimal Conductivity in Graphene with Long-Range Disorder*, Phys. Rev. Lett. **98**, 256801 (2007).

[59] A. Kitaev, AIP Conf. Proc. No. 1134 (AIP, New York, 2009), p. 22.

[60] A. A. Nersesyan, A. M. Tsvelik, F. Wenger, *Disorder Effects in Two-Dimensional d-Wave Superconductors*, Phys. Rev. Lett. **72**, 2628, (1994).

[61] C. Mudry, C. Chamon, and X.-G. Wen, *Two-dimensional conformal field theory for disordered systems at criticality*, Nucl. Phys. B **466**, 383 (1996).

[62] J.-S. Caux, I. I. Kogan, and A. M. Tsvelik, *Logarithmic operators and hidden continuous symmetry in critical disordered models*, Nucl. Phys. B **466**, 444 (1996).

[63] M. J. Bhaseen, J.-S. Caux, I. I. Kogan, and A. M. Tsvelik, *Disordered Dirac fermions: the marriage of three different approaches*, Nucl. Phys. B **618**, 465 (2001).

[64] A. M. Essin and V. Gurarie, *Delocalization of boundary states in disordered topological insulators*, J. Phys. A: Math.Theor. **48** (2015).

[65] A. M. Essin and V. Gurarie, *Bulk-boundary correspondence of topological insulators from their respective Green's functions*, Phys. Rev. B **84**, 125132 (2011).

[66] A. P. Schnyder, S. Ryu, and A. W. W. Ludwig, *Lattice Model of a Three-Dimensional Topological Singlet Superconductor with Time-Reversal Symmetry*, Phys. Rev. Lett. **102**, 196804 (2009).

[67] F. D. M. Haldane, *Continuum dynamics of the 1-D Heisenberg antiferromagnet: Identification with the O(3) nonlinear sigma model*, Phys. Lett. A **93**, 464 (1983); *Nonlinear Field Theory of Large-Spin Heisenberg Antiferromagnets: Semiclassically Quantized Solitons of the One-Dimensional Easy-Axis Néel State*, Phys. Rev. Lett. **50**, 1153 (1983).

[68] A. M. M. Pruisken, "Field theory, scaling and the localization problem," in *The Quantum Hall Effect*, ed. R. E. Prange and S. M. Girvin (Springer-Verlag, 1987).

[69] T. Senthil, M. P. A. Fisher, L. Balents, and C. Nayak, *Quasiparticle Transport and Localization in High-T_c Superconductors*, Phys. Rev. Lett. **81**, 4704 (1998).

[70] Y. Liao, A. Levchenko, and M. S. Foster. *Response theory of the ergodic many-body delocalized phase: Keldysh Finkel'stein sigma models and the 10-fold way*, Ann. Phys. **386**, 97 (2017).

[71] P. Di Francesco, P. Mathieu, and D. Sénéchal, *Conformal Field Theory* (Springer-Verlag, New York, 1997).

[72] E. J. König, P. M. Ostrovsky, I. V. Protopopov, and A. D. Mirlin, *Metal-insulator transition in two-dimensional random fermion systems of chiral symmetry classes*, Phys. Rev. B **85**, 195130 (2012).

[73] Note that quasiparticles in the BdG description of a superconductor cannot be "doped" to a nonzero chemical potential, because the zero of energy is always determined by the correlation gap (which occurs at the Fermi energy in the BCS regime). This is true both for quasiparticles in a nontopological, gapless (e.g. *d*-wave) superconductor, and for surface state Dirac or Majorana fermions in a TSC. For the sigma model designed to calculate the physical spin conductivity, the nonzero energy wave functions formally enter the zero temperature response by retaining $\omega \neq 0$ in Eqs. (4.11a) and (4.11b). For class CI, this is not a "soft" insertion, since it is guaranteed that the finite-energy wave functions belong to a different class.

[74] M. Bocquet, D. Serban, and M. R. Zirnbauer, *Disordered 2d quasiparticles in class D: Dirac fermions with random mass, and dirty superconductors*, Nucl. Phys. B **578**, 628 (2000).

[75] X. Wan, A. M. Turner, A. Vishwanath, and S. Y. Savrasov, *Topological semimetal and Fermi-arc surface states in the electronic structure of pyrochlore iridates*, Phys. Rev. B 83, 205101 (2011).

[76] K. Y. Yang, Y. M. Lu, and Y. Ran, *Quantum Hall effects in a Weyl semimetal: Possible application in pyrochlore iridates*, Phys. Rev. B 84, 075129 (2011).

[77] A. A. Burkov and L. Balents, *Weyl Semimetal in a Topological Insulator Multilayer*, Phys. Rev. Lett. 107, 127205 (2011).

[78] A. A. Burkov, M. D. Hook, and L. Balents, *Topological nodal semimetals*, Phys. Rev. B 84, 235126 (2011).

[79] P. Hosur and X. Qi, *Recent developments in transport phenomena in Weyl semimetals*, C. R. Phys. 14, 857 (2013).

[80] T. Meng and L. Balents, *Weyl superconductors*, Phys. Rev. B 86, 054504 (2012).

[81] D. T. Son and B. Z. Spivak, *Chiral anomaly and classical negative magnetoresistance of Weyl metals*, Phys. Rev. B 88, 104412 (2013).

[82] X. Huang, L. Zhao, Y. Long, P. Wang, D. Chen, Z. Yang, H. Liang, M. Xue, H. Weng, Z. Fang, X. Dai, and G. Chen, *Observation of the Chiral-Anomaly-Induced Negative Magnetoresistance in 3D Weyl Semimetal TaAs*, Phys. Rev. X **5**, 031023 (2015).

[83] H. J. Kim, K. S. Kim, J. F. Wang, M. Sasaki, N. Satoh, A. Ohnishi, M. Kitaura, M. Yang, and L. Li, *Dirac versus Weyl Fermions in Topological Insulators: Adler-Bell-Jackiw Anomaly in Transport Phenomena*, Phys. Rev. Lett. **111**, 246603 (2013).

[84] S. Y. Xu, I. Belopolski, N. Alidoust, M. Neupane, C. Zhang, R. Sankar, S. M. Huang, C. C. Lee, G. Chang, B. Wang, G. Bian, H. Zheng, D. S. Sanchez, F. Chou, H. Lin, S. Jia, and M. Z. Hasan, *Discovery of a Weyl fermion semimetal and topological Fermi arcs*, Science **349**, 613 (2015).

[85] B. Q. Lv, N. Xu, H. M. Weng, J. Z. Ma, P. Richard, X. C. Huang, L. X. Zhao, G. F. Chen, C. Matt, F. Bisti, V. N. Strocov, J. Mesot, Z. Fang, X. Dai, T. Qian, M. Shi, and H. Ding, *Observation of Weyl nodes in TaAs*, Nat. Phys. **11**, 724 (2015).

[86] L. Lu, Z. Wang, D. Ye, L. Ran, L. Fu, J. D. Joannopoulos, and M. Soljacic, *Experimental observation of Weyl points*, Science **349**, 622 (2015).

[87] A. A. Soluyanov, D. Gresch, Z. Wang, Q. Wu, M. Troyer, X. Dai, and B. A. Bernevig, *Type-II Weyl semimetals*, Nature (London) **527**, 495 (2015).

[88] G. Sharma, P. Goswami, and Sumanta Tewari, *Chiral anomaly and longitudinal magnetotransport in type-II Weyl semimetals*, Phys. Rev. B **96**, 045112 (2017).

[89] G. Xu, H. Weng, Z. Wang,X. Dai and Z. Fang, *Chern Semimetal and the Quantized Anomalous Hall Effect in HgCr2Se4*, Phys. Rev. Lett. **107**, 186806 (2011).

[90] C. Fang, M. J. Gilbert, X. Dai, and B. A. Bernevig, *Multi-Weyl Topological Semimetals Stabilized by Point Group Symmetry*, Phys. Rev. Lett. **108**, 266802 (2012).

[91] S.-M. Huang, S.-Y. Xu, I. Belopolski, C.-C. Lee, G. Chang, T.-R. Chang, B. Wang, N. Alidoust, G. Bian, M. Neupane, D. Sanchez, H. Zheng, H.-T. Jeng, A. Bansil, T. Neupert, H. Lin, and M. Z. Hasan, *New type of Weyl semimetal with quadratic double Weyl fermions*, Proc. Natl. Acad. Sci. USA **113**, 1180 (2016).

[92] A. A. Zyuzin and R. P. Tiwari, *Intrinsic anomalous Hall effect in type-II Weyl semimetals*, JETP Lett. **103**, 717 (2016).

[93] T. Oka and H. Aoki, *Photovoltaic Hall effect in graphene*, Phys. Rev. B **79**, 081406 (2009).

[94] T. Kitagawa, E. Berg, M. Rudner, and E. Demler, *Topological characterization of periodically driven quantum systems*, Phys. Rev. B 82, 235114 (2010).

[95] T. Kitagawa, T. Oka, A. Brataas, L. Fu, and E. Demler, *Transport properties of nonequilibrium systems under the application of light: Photoinduced quantum Hall insulators without Landau levels*, Phys. Rev. B **84**, 235108 (2011).

[96] Z. Yan and Z. Wang, *Floquet multi-Weyl points in crossing-nodal-line semimetals*, Phys. Rev. B **96**, 041206(R) (2017).

[97] M. Ezawa, *Photoinduced topological phase transition from a crossing-line nodal semimetal to a multiple-Weyl semimetal*, Phys. Rev. B **96**, 041205(R) (2017).

[98] N. Goldman and J. Dalibard, *Periodically Driven Quantum Systems: Effective Hamiltonians and Engineered Gauge Fields*, Phys. Rev. X **4**, 031027 (2014).

[99] H. Hubener, M. A. Sentef, U. D. Giovannini, A. F. Kemper and A. Rubio, *Creating stable FloquetWeyl semimetals by laser-driving of 3D Dirac materials*, Nature Communications **8**, 13940 (2017).

[100] C. K. Chan, Y. T. Oh, J. H. Han, and P. A. Lee, *Type-II Weyl cone transitions in driven semimetals*, Phys. Rev. B 94, 121106(R) (2016).

[101] X. X. Zhang, T. T. Ong and N. Nagaosa, *Theory of photoinduced Floquet Weyl semimetal phases*, Phys. Rev. B **94**, 235137 (2016).

[102] J. Y. Zou and B. G. Liu, *Floquet Weyl fermions in three-dimensional stacked graphene systems irradiated by circularly polarized light*, Phys. Rev. B **93**, 205435 (2016).

[103] Z. Yan and Z. Wang, *Tunable Weyl Points in Periodically Driven Nodal Line Semimetals*, Phys. Rev. Lett. 117, 087402 (2016).

[104] E.-G. Moon, C. Xu, Y. B. Kim, and L. Balents, *Non-Fermi-Liquid and Topological States with Strong Spin-Orbit Coupling*, Phys. Rev. Lett. 111, 206401 (2013).

[105] W. Witczak-Krempa, G. Chen, Y. B. Kim, and L. Balents, *Correlated Quantum Phenomena in the Strong Spin-Orbit Regim*, Annu. Rev. Condens. Matter Phys. 5, 57 (2014).

[106] S. Chadov, X. Qi, J. Kubler, G. H. Fecher, C. Felser, and S. C. Zhang, *Tunable multifunctional topological insulators in ternary Heusler compounds*, Nat. Mat. **9**, 541 (2010).

[107] H. Lin, L. A. Wray, Y. Xia, S. Xu, S. Jia, R. J. Cava, A. Bansil, and M. Z. Hasan, *Half-Heusler ternary compounds as new multifunctional experimental platforms for topological quantum phenomena*, Nat. Mat. **9**, 546 (2010).

[108] D. Xiao, Y. Yao, W. Feng, J. Wen, W. Zhu, X.-Q. Chen, G. M. Stocks, and Z. Zhang, *Half-Heusler Compounds as a New Class of Three-Dimensional Topological Insulators*, Phys. Rev. Lett. **105**, 096404 (2010).

[109] P. Goswami, B. Roy, and S. Das Sarma, *Competing orders and topology in the global phase diagram of pyrochlore iridates*, Phys. Rev. B **95**, 085120 (2017).

[110] I. Boettcher and I. F. Herbut, *Anisotropy induces non-Fermi-liquid behavior and nematic magnetic order in three-dimensional Luttinger semimetals*, Phys. Rev. B **95**, 075149 (2017).

[111] I. Boettcher and I. F. Herbut, *Superconducting quantum criticality in three-dimensional Luttinger semimetals*, Phys. Rev. B **93**, 205138 (2016).

[112] J. Cano, B. Bradlyn, Z. Wang, M. Hirschberger, N. P. Ong, and B. A. Bernevig, *Chiral anomaly factory: Creating Weyl fermions with a magnetic field*, Phys. Rev. B **95**, 161306(R) (2017).

[113] S. A. A. Ghorashi, Y. Liao, M.S. Foster, *Critical percolation without fine tuning on the surface of a topological superconductor*, arXiv:1711.03972.

[114] Y. Wang, H. Steinberg, P. Jarillo-Herrero, and N. Gedik, *Observation of Floquet-Bloch states on the surface of a topological insulator*, Science **342**, 453 (2013).

[115] T. Oh and B-J Yang, *Topological semimetals induced by magnetic control of the Luttinger q-term in pyrochlore iridates*, arXiv:1709.06796v1.